Université Fédérale
Toulouse Midi-Pyrénées

# THÈSE

## En vue de l'obtention du
## DOCTORAT DE L'UNIVERSITÉ DE TOULOUSE

**Délivré par l'Université Toulouse 3 - Paul Sabatier**

---

**Présentée et soutenue par**

**Refik Baris YILMAZ**

Le 6 décembre 2023

## Développement d'actionneurs souples : Étude de l'actionnement et des propriétés mécaniques des hydrogels macroporeux sensibles à la chaleur et à la chimie

---

Ecole doctorale : **GEETS - Génie Electrique Electronique,Télécommunications et Santé : du système au nanosystème**

Spécialité : **MicroNano Systèmes**

Unité de recherche :
**LAAS - Laboratoire d'Analyse et d'Architecture des Systèmes**

Thèse dirigée par
**Vincent MANSARD**

Jury

**M. Hugues BODIGUEL,** Rapporteur
**M. Cedric PLESSE,** Rapporteur
**Mme Pauline ASSEMAT,** Examinatrice
**M. Nicolas MANO,** Examinateur
**M. Vincent MANSARD,** Directeur de thèse
**M. Christian BERGAUD,** Président

PhD Thesis

# Development of Hydrogel Based Soft Actuators: Investigation of Actuation Properties of Macroporous Thermal/Chemical Sensitive Hydrogels

Refik Barış YILMAZ

Supervised by: Vincent MANSARD

Thesis prepared at: LAAS-CNRS, MEMS team

7, avenue du Colonel Roche,

BP 54200, 31031 Toulouse

Cedex 4

**To my dear family**

**and**

**my wife İrem**

# Acknowledgements

This thesis work was achieved thanks to the support of various people whom I would like to gratefully acknowledge.

I would like to thank my supervisor Vincent Mansard for giving me the opportunity to work in such a scientifically rich environment of LAAS-CNRS. His fast and outside-the-box thinking inspired me to take a step back and see the bigger picture in troubling situations rather than being affixed to specific problems. Thanks for being available and understanding anytime I needed help. I believe I learned a lot about working on interdisciplinary projects thanks to his supervision.

Thanks a lot to Ali Maziz for all his help especially in chapter 4 in which I benefited a lot from his knowledge of electrochemistry. I appreciate his helpful, understanding, and empathetic approach whenever I needed. Also, the small talks whenever we came across helped me a lot to stay positive.

I am also grateful to Christian Bergaud for his supportive, understanding, and guiding presence. Having such a positive and polite director, I felt very safe and supported which is very inspiring on what type of influence I would like to also have on my colleagues in the future.

It is important to put forward how important the help from the I2C team was for me. I would like to thank Marie-Charline Blatche and Sandrine Assie-Souleille for all the formations on the equipment in C211 and helping me every time I needed it throughout my studies. Also thanks a lot to Lionel Séguier for all the formations and help with the melt extrusion 3D printing in FabLAAS.

I would like to thank Julie Foncy for her huge help in stereo-lithography. Her both helpful and joyful presence in the MultiFab lab was very nice for all the long hours I spent 3D printing various designs. Thanks to her and Laurent Malaquin, I also had the chance to gain experience in 3D printing with new materials.

I was able to analyze my samples using SEM and EDX thanks to the formation I received from Benjamin Reig. His knowledge, patience, and helpfulness were also very important for me to better analyze my samples. I would also like to thank the TEAM team for all the formations in the clean room.

I would like to thank the members of the MEMS team, Elise Pierre, Yosr Chaabane, Damien Ourmet, Clément Cointe, Aarushee Rangra, Asma Eddarir, Aleksandra Markovic, Onkar Kulkarni, Valentin Saunier, Venkata Suresh Vajrala as they were warm, welcoming and friendly which made being a part of the team easier. Thanks, Elise, Yosr, and Damien for being such lovely office mates and colleagues. Thanks to Constandina Arvanitis for her guidance. Although we met in the last year of my study at LAAS, the empathetic and inspiring chats helped a lot to clear my vision in the difficult times.

One of the best outcomes of this Ph.D. study was gaining a friend like Raul Sanchez Olvera. Thanks to him, I felt like there was always someone in the laboratory that I could count on and ask for help anytime. Thank you for all the time we spent chatting, grabbing lunch, drinking, and traveling. It was great to share all these moments. Thanks to my friends Ophélie Thomas-Chemin, Hugo Villanti, Nadiia Yakovenkova, Leonardo Cancellara, and Gozde Eke. Thanks to all of you, even myself who was never good at dealing with changes, did not have a problem in building a new life in Toulouse. It is great to know the presence of such nice people keeping the world spinning.

Of course, a special thanks to my wonderful, beloved wife. I believe my biggest chance in life was meeting such a person early in life. You are the driving force for every success in my life. I am grateful to have such a loving, caring, and fun partner in this journey called life. I hope I did not tire you out with my whinings throughout my Ph.D. (It will get worse with age they say). Without you, I would not even think of applying a Ph.D. position in France to begin with so thanks for the new title. Also thank you for extending my family with such great individuals. I can see all the reflections of these great people who raised you and I am happy to be a part of an even bigger family now.

Finally, a big thanks to my mother and father. It feels great to know that I followed your steps. Knowing all the difficulties and challenges you endured to achieve everything you wanted in this life, I cannot think of any better role models. As you always say, Mom, we will always work hard as it is the only way to gain real self-satisfaction in this life. Also thank you for my brother, I know it was a big request but he turned out to be a great guy. Thank you Mom and Dad for being who you are and giving me such a loving, caring family.

# Abstract

Today, the world of actuators is dominated by the more conventional, well established systems based on piezo-electric, pneumatic or electromagnetic principals. The main reason behind this is the high efficiency, adaptability and controllability of hard mechanical/electrical systems with great precision. Yet, as the complexity of the controlled motion increases which requires whole lot more actuators or the size of the overall system decreases, the limitations of down scalability becomes problematic. Thus, soft materials are crucial in filling the gap left by the conventional active materials as the technological progress favors smaller, softer and lighter systems. The key attribute of soft materials in such situation is the extreme adaptability due to the elastic nature overcoming the size and weight limitations.

In this study, we first investigate the volume phase change properties next to mechanical properties of microporous thermo-sensitive PNIPAM gel. As we aimed to utilize the gel as the smart soft actuator, we optimized shrinking/re-swelling kinetics by overcoming diffusion limitations with engineering the macroporosity. We developed a cost-efficient, simple single-dot Braille device with fast actuating PNIPAM gel alternative to conventional piezo-electric actuators with all the requirements for tactile display applications. We conducted the mechanical, morphological and thermal analysis on the resulting system.

Secondly, we developed a novel template by 3D printing to apply controlled level and geometry of macroporosity on the PNIPAM gels. By developing a setup in which fluid flow through the microporous hydrogel could be controlled precisely, we investigated the effect of porosity level, and temperature on water permeability of the gel. Moreover, we also observed and analyzed the poroelastic deformation of the gel upon compression by the fluid flow. We were also able to obtain the evolution of pressure gradient, decreasing flow rate and eventually the change in water permeability of the gel upon shrinking.

Finally, we developed a PAAc/PEDOT:PSS double network electro-active hydrogel actuator. We achieved electronic conductivity (~10 S/cm) in a 3D gel matrix by incorporating a second PEDOT:PSS network. We conducted electrochemical, rheological, mechanical, morphological characterizations on the obtained conductive gel. Lastly, we analysed the efficiency and reversibility of neat PAAc gel complexation with metallic ions.

# Résumé

Aujourd'hui, le monde des actionneurs est dominé par les systèmes plus conventionnels et bien établis basés sur des principes piézo-électriques, pneumatiques ou électromagnétiques. La raison principale en est la grande efficacité, l'adaptabilité et la contrôlabilité des systèmes mécaniques/électriques durs avec une grande précision. Cependant, lorsque la complexité du mouvement contrôlé augmente, ce qui nécessite beaucoup plus d'actionneurs, ou lorsque la taille du système global diminue, les limites de l'évolutivité vers le bas deviennent problématiques. Les matériaux souples sont donc essentiels pour combler le vide laissé par les matériaux actifs conventionnels, car les progrès technologiques favorisent les systèmes plus petits, plus souples et plus légers. L'attribut clé des matériaux souples dans une telle situation est l'extrême adaptabilité due à la nature élastique qui permet de surmonter les limitations de taille et de poids.

Dans cette étude, nous avons d'abord étudié les propriétés de changement de phase en volume ainsi que les propriétés mécaniques d'un gel microporeux thermosensible de PNIPAM. L'objectif étant d'utiliser le gel comme actionneur souple intelligent, nous avons optimisé la cinétique de rétrécissement et de gonflement en surmontant les limitations de diffusion grâce à l'ingénierie de la macroporosité. Nous avons mis au point un dispositif braille simple et rentable à point unique avec un gel PNIPAM à actionnement rapide qui remplace les actionneurs piézo-électriques conventionnels et répond à toutes les exigences des applications d'affichage tactile. Nous avons effectué des analyses mécaniques, morphologiques et thermiques sur le système obtenu.

Deuxièmement, nous avons développé un nouveau modèle par impression 3D pour appliquer un niveau et une géométrie contrôlés de macroporosité sur les gels de PNIPAM. En développant un dispositif dans lequel l'écoulement des fluides à travers l'hydrogel microporeux peut être contrôlé avec précision, nous avons étudié l'effet du niveau de porosité et de la température sur la perméabilité à l'eau du gel. En outre, nous avons également observé et analysé la déformation poroélastique du gel lors de la compression par le flux de fluide. Nous avons également pu obtenir l'évolution du gradient de pression, la diminution du débit et finalement le changement de la perméabilité à l'eau du gel lors du rétrécissement.

Enfin, nous avons développé un actionneur hydrogel électro-actif à double réseau PAAc/PEDOT:PSS. Nous avons obtenu une conductivité électronique (~10 S/cm) dans une matrice de gel 3D en incorporant un second réseau de PEDOT:PSS. Nous avons effectué des

caractérisations électrochimiques, rhéologiques, mécaniques et morphologiques sur le gel conducteur obtenu. Enfin, nous avons analysé l'efficacité et la réversibilité de la complexation du gel PAAc pur avec des ions métalliques.

# Publications

The following publication is based on the work presented in this thesis:

[1] R.B. Yilmaz, Y. Chaabane, V. Mansard, Development of a Soft Actuator from Fast Swelling Macroporous PNIPAM Gels for Smart Braille Device Applications in Haptic Technology, ACS Appl. Mater. Interfaces. (2023). https://doi.org/10.1021/acsami.2c17835.

# Abbreviations

## Materials

| | |
|---|---|
| **APS** | ammonium persulfate |
| **CNT** | carbon nanotube |
| **CP** | conductive polymer |
| **DDBAB** | dodecyl dimethyl benzyl ammonium bromide |
| **DDTC** | diethyldithiocarbamate |
| **DEA** | dielectric elastomer |
| **DEAEMA** | diethylaminoethyl methacrylate |
| **DMAEMA** | dimethylamineoethyl methacrylate |
| **EDTA** | ethylenediaminetetraacetic acid |
| **LC** | liquid crystal |
| **LCE** | liquid crystal elastomer |
| **MAAc** | methacrylic acid |
| **PAAc** | poly(acrylic acid) |
| **PANI** | polyaniline |
| **PEDOT** | poly(3,4-ethylenedioxythiophene) |
| **PEG** | polyethylene glycol |
| **PI** | polyimide |
| **PLA** | poly(lactic acid) |
| **PMMA** | poly(methyl methacrylate) |
| **PNaAC** | poly(sodium acrylate) |
| **PNIPAM** | poly(n-isopropylacrylamide) |
| **PPY** | polypyrrole |
| **PSS** | polystyrene sulfonate |
| **PTSA** | p-toluenesulfonic acid |
| **PU** | polyurethane |
| **PVDC** | polyvinylidene chloride |

**PVDF** polyvinylidene flouride

**RT** room temperature

**SDS** sodium dodecylsulfate

**SMA** shape memory alloy

**SME** shape memory elastomer

**SMP** shape memory polymer

**TiNS** titanium nanoscales

## Created abbreviations used for materials

**DN** double network

**HP** high porous

**LP** low porous

**MP** macroporous

**OR** organically reticulated

## Characterization techniques

**AFM** atomic force microscopy

**CV** cyclic voltammetry

**DIC** digital image correlation

**EDX** energy dispersive X-ray

**SEM** scanning electron microscopy

## Other

**DC** direct current

**IPN** interpenetrated network

**LCST** lower critical solution temperature

**MEMS** micro electro mechanical system

**NC** nano composite

**NEMS** nano electro mechanical system

**PCB** printed circuit board

**UCST** upper critical solution temperature

| | |
|---|---|
| **UV** | ultra violet |
| **VPTT** | volume phase transition temperature |

# Table of Contents

**General Introduction** ..... 1

References ..... 6

**1. Introduction** ..... 9

1.1. Actuation Technology in Micro-Millimeter Systems ..... 9

1.2. Need of Small Actuators in Haptic Technology ..... 12

1.2.1. Braille Alphabet and Current Electronic Braille Devices ..... 12

1.2.2. Key Actuation Technologies for Commercial Braille Devices ..... 15

1.3. Active (Smart) Materials ..... 21

1.3.1. Conductive Polymers ..... 22

1.3.2. Dielectric Elastomers (DEAs) ..... 25

1.3.3. Shape Memory Polymers (SMPs) ..... 27

1.3.4. Liquid Crystalline Elastomers ..... 29

1.3.5. Smart Hydrogels ..... 34

1.4. Compliance of Smart Hydrogels for Untethered Actuation ..... 38

1.4.1. Smart Gels Sensitive to Different Stimuli ..... 38

1.5. Response Dynamics of Hydrogels ..... 44

1.5.1. Poroelastic Swelling of Hydrogels ..... 44

1.5.2. Free Swelling of PNIPAM Gel ..... 46

1.5.3. Macroporous Gel ..... 48

1.6. Motivation and Problem Statement ..... 49

1.7. Thesis Structure ..... 50

Chapter 2 ..... 50

Chapter 3 ..... 50

Chapter 4 ..... 50

1.8. References ..... 51

**2. Development of a Braille Device Utilizing Thermo-Sensitive Macroporous PNIPAM Hydrogel as the Fast Actuator** ..... 61

2.1. Introduction ..... 62

2.2. Macroporous Gels ..... 63

2.3. Shrinking/Re-Swelling of PNIPAM Gels ..... 66

2.4. Mechanical Properties of Macroporous PNIPAM Gels ..... 73

2.4.1. Effect of Macroporosity on Mechanical Properties of PNIPAM Gels ..... 73
2.5. Single Pin Braille Device ..... 77
2.5.1. Fabrication of The Single Pin Braille Device ..... 77
2.5.2 Thermal Efficiency Analysis of the Single Pin Braille Device ..... 81
2.6. Conclusions ..... 83
2.7. References ..... 84
**3. Characterization of Poroelastic Properties of Macroporous PNIPAM Hydrogel** ..... 89
3.1. Introduction ..... 90
3.2. Development of 3D Printed Shellac Scaffolds ..... 92
3.3. Development of Porous PNIPAM Hydrogel ..... 97
3.4. Unconstrained Swelling of Porous PNIPAM Hydrogel ..... 98
3.5. Diffusion Coefficient of Water in the Porous Gel Matrix ..... 99
3.6. Analysis of Poroelastic Gel Properties via Controlled Flow Experiment ..... 103
3.6.1. Development of the Experimental Setup ..... 103
3.6.2. Characterization of Hydrogel Permeability ..... 106
3.6.3. Poroelasticity of the Gel ..... 108
3.6.4. Flow Dynamics Upon Temperature Change ..... 110
3.7. Conclusion ..... 112
3.8. References ..... 114
**4. Development of an Electroactive PAAc/PEDOT:PSS Hydrogel Actuator** ..... 115
4.1. Introduction ..... 116
4.2. Conductive Gel ..... 118
4.3. Development of Conductive Double Network Gels ..... 120
4.3.1. Strategy #1: Impregnation of EDOT Monomers into PAAc Gel ..... 120
4.2.1. Strategy #2: Single Step Polymerization of AAc with PEDOT:PSS Dispersion ..... 125
4.2.2. Strategy #3: Impregnation of Gellified PEDOT:PSS with AAc Monomer ..... 127
4.3. Electrochemical Characterization of Double Network Gels ..... 129
3.3.1. Electrochemical Performance of DN Gels in the Presence of Copper Ions ..... 132
4.4. Macroporous Conductive Double Network Gels ..... 137
4.5. Investigation of Swelling/Shrinking Behavior of PAA Gels in the Presence of $Cu^{2+}$ Ions ..... 140
4.6. Can we couple electrochemistry and actuation? ..... 142

4.7. Conclusion ..... 144
4.8. References ..... 146
**General Conclusions** ..... 148
**Appendix: Materials and Methods** ..... 151
A.2-Chapter 2: Development of a Braille Device Utilizing Thermo-Sensitive Macroporous PNIPAM Hydrogel as the Fast Actuator ..... 151
A.2.1 Preparation of NC Gel ..... 151
A.2.2 Preparation of OR Gel ..... 151
A.2.3 Preparation of High Porosity (HP) Gels ..... 151
A.2.4 Preparation of Low Porosity (LP) Gels ..... 152
A.2.5 Mechanical Testing ..... 153
A.4 Chapter 4: Development of an Electroactive PAAc/PEDOT:PSS Hydrogel Actuator ..... 154
A.4.1 Impregnation of PAAc Gel with EDOT Monomers ..... 154
A.4.2. Four Point Probe Conductivity Measurement ..... 155
A.4.3 Single Step Polymerization of AAc with PEDOT:PSS Dispersion ..... 155
A4.4 Production of Agarose/PEDOT:PSS Gels ..... 156
A.4.5 Impregnation of Gellified PEDOT:PSS with AAc Monomer ..... 156
A.4.6 Rheological Characterization on the Gellification Process of PEDOT:PSS Dispersion ..... 156
A.4.7. Electrochemical Characterization of DN Hydrogels ..... 158
A.4.8 Preparation of PEDOT:PSS Coated PVDF Membrane ..... 158
A.4.9 Preparation of Macroporous Conductive Double Network Gel ..... 159
A.4.10 Preparation of Buffer Solutions ..... 159
A.4.11 Determination of Copper Concentrations via Complexometric Spectrophotometry Method ..... 159

# Table of Figures

**Figure 1. 0:** Spectrum of materials according to their elastic moduli. ..... 2
**Figure 1.1:** Spectrum of materials according to their elastic moduli. ..... 10
**Figure 1.2:** a) Contraction and opening of the tendon shaped silicone actuator upon negative and positive pressure inside, relatively) The three-armed gripper grasping an aluminum cup [7]. ..... 11
**Figure 1.3:** a) The Braille alphabet in its current form [8]. Commercial Braille displays a) BrailleSense-6, b) Hyperbraille-F and c) ActiveBraille. ..... 13
**Figure 1.4:** Lateral view of a typical piezo bimorph Braille Cell [9]. ..... 16
**Figure 1.5:** (a) Braille display with a micro-pneumatic channel (manifold) system, (b) Braille setup with five connected tubes (one for pressure input, four for different output tubes) [10]. ..... 17
**Figure 1.6**: (a) Schematic of the single pin magnetic actuation components, (b) PCB containing 4x4 haptic display [13]..... 18
**Figure 1.7:** (a) All 18 layers of copper tracking for a single solenoid, (b) 6x6, 18-layer PCB solenoid [23]. ..... 19
**Figure 1.8:** (a) The characteristic phase diagram and (b) sketch of the SMA coil actuator. The stroke stands for the volume/length change of the SMA coil upon heating/cooling. When the SMA coil extends upon heating, it compresses the bias spring and upon cooling bias coil stretches. Reversible motion is attained by such double coil system [14]. ..... 20
**Figure 1.9**: Schematic of the tactile display utilizing magnetic latch mechanism and SMA coil actuators [14]. ..... 20
**Figure 1.10:** The ion actuation mechanism of p-doped polymer actuators: a) anion transport dominated when anions are small and mobile (e.g. PEDOT:PTSA), b) cation transport dominated when anion are large and immobile (e.g. PEDOT:PSS) [26]. ..... 24
**Figure 1.11:** a) Cross-sectional image of the trilayer PEDOT:PSS/PVDF/PEDOT:PSS structure. b) A dragon-fly shaped inkjet printed PEDOT:PSS actuator and the resulting movement of the wings upon actuation. ..... 25
**Figure 1.12:** Illustration of a DEA system. ..... 26
**Figure 1.13:** a) Images showing the contraction of the arm with the help of the DEA. b) Multiple stack of DEAs. The dark gray ones are active layers while light colors are the passive layers. Metallic supports are placed in between to support the system. c) Zoomed in image of

the DEA stacks. Each layers consists of 25 individual elastomers with approximately 30μm thicknesses [29]. 27
**Figure 1.14:** The stages of thermally induced shape memory effect. Ttrans is the thermal transition temperature of the switching (soft) phase. 28
**Figure 1.15:** a) Schematic of the parts of 3D printed swimming robot. b) The SMP muscle in its deployed (I), transitioning (II) and activated (III) phases. c) Images of the soft robot swimming with frontal strokes [30]. 29
**Figure 1.16:** Different alignment characteristics of mesogens in liquid crystalline phase of thermotropic LCEs with increasing temperature. 30
**Figure 1.17:** Different attachment of mesogens on the polymer backbone for the synthesis of LCEs. Side chain elastomer with a) end-on, b) side-on attached meseogens. Main chain elastomers with c) end-on and d) side-on attached mesogenic units [31]. 31
**Figure 1.18:** a) Schematic of the self-healing of the LCE matrix by bond exchange reactions between thiol groups. b) Sandwich structure of the LCE actuator contracting upon passage of hot water due to the nematic to isotropic phase change of the mesogens. c) 8 LCE actuators assembled to achieve ~2cm displacement under 2N (200g) force. d) Graph depicting the actuation strains and rates when water at different temperatures are passed through the channels for 10s followed by cooling with water at RT for 10s [32]. 33
**Figure 1.19:** Examples of different methods for providing anisotropic actuation motion to smart hydrogels. a) Sequential synthesis method. Bilayer PNIPAM/Clay nanocomposite (NC) gel The bending motion induced upon heating over volume phase transition temperature (VPTT) [37]. b) Field induced anisotropy method. Titanate nanoscale (TiNS) particles were aligned in the aqueous NIPAM monomer solution by strong magnetic fields before UV initiated polymerization. The thermally triggered volume change of PNIPAM was more prominent in the direction perpendicular to the TiNS layers converting isotropic swelling to bending motion [38]. c) Ionoprinitng on PNaAc gel inducing metal complexation in gel matrix. Ionoprinted gel actuating in coiling mode upon shrinking. Scale bar, 5 mm [39]. d) Schematic of the IPN PNIPAM/PAAc double layer structure. Green zones are PNIPAM gel whereas transparent zones represent PAAc gel and images of the resulting buckling when the pH is increased from 1 to 9. Scale bar is 1 cm [40]. e) Extrusion of the PNIPAM/clay solution containing cellulose nanofibrils through a nozzle with 200 μm internal diameter. The printed grid structure and resulting bending motion upon heating due to the anisotropy generated by the aligned nanofibrils [41]. 36

**Figure 1.20:** Temperature vs polymer volume fraction graphs as phase diagrams of polymer solution with a) LCST and b) UCST behavior [49]. ..... 39
**Figure 1.21:** Mechanism of the volume change of PAA hydrogel upon redox reaction of copper [69]. ..... 42
**Figure 1.22:** Schematic of the hypothetical gels swelling induced by elongation [83]. ..... 46
**Figure 1.23:** Comparison of the experimental results and theoretical predictions of both constrained and unconstrained swelling of PNIPAM gel. The diffusion coefficient data was obtained from the initial slope of the constrained swelling results then used with the equilibrium swelling ratios to plot the analytical solution [82]. ..... 47
**Figure 2.1:** (a, c) SEM images of the sacrificial template: (a) melt spun shellac fibers and (c) PMMA microspheres. (b, d) Images of the MP gel using DIC microscopy to observe the macroporosity: (b) LP-OR gel and (d) HP-NC gel. SEM images and DIC microscopy images are at the same scale to emphasize the similarity between the initial sacrificial scaffold and the final porosity. No SEM images of the porous gels are shown here, as drying the gel dramatically affects the gel structure. ..... 65
**Figure 2.2:** Long-term (a) shrinking and (b) re-swelling graphs of PNIPAM gels. Data is obtained by periodic weighing of gels. Color indicators show red as OR, black as NC, green as LP-NC, blue as LP-OR and purple as HP-OR gels. ..... 67
**Figure 2.3:** Schematic of the real-time imaging setup for the shrinking/re-swelling tests. .... 67
**Figure 2.4 :** Evolution of the volume ratio $V/V_0$ (where $V_0$ is the initial gel volume at room temperature before shrinking) as a function of time when the gel is successively dipped (b) in hot water and then (c) in cold water for (blue) LP-OR, (green) LP-NC, and (pink) HP-OR gel. The inset in (b) gives the dynamic of shrinking for bulk gel: (black) NC gel, (red) OR gel... 68
**Figure 2.5 :** SEM images of sintered PMMA scaffold cross-sections with average particle diameters of (a) 75 ± 30 µm and (b) 60 ± 20 µm. ..... 70
**Figure 2.6 :** Evolution of the volume ratios V/V0 (where V0 is the initial gel volume) as a function of temperature when we slowly raise the temperature of the surrounding water bath (at 1 °C/min) for (green) LP-NC, (blue) LP-OR, and (purple) HP-OR gel. ..... 71
**Figure 2.7 :** (a) True stress−strain curves of (red) bulk OR, (black) bulk NC, (green) LP-NC, (blue) LP-OR, and (pink) HP-OR gel. (b) Elastic modulus values of the gel samples (same color coding). ..... 73
**Figure 2.8 :** (a−c) True stress versus strain graphs of gel samples under cycling deformation : (black) 1st cycle and (red) 100th cycle. ..... 75
**Figure 2.9 :** a) Tensile test setup for the gel samples, b) tensile test data of the HP-OR gel.. 76

**Figure 2.10 :** (a) Elastic modulus data of HP-OR gels with different average pore diameters. (b) True stress/deformation curves of small pored (red) and big pored (black) HP-OR gel upon compression test. ..... 76
**Figure 2.11 :** (a, b) Image and 3D representation of the single-pin braille setup. ..... 77
**Figure 2.12 :** (a) Equilibrium temperature of the gel containment unit as a function of the heating powers. (b) Evolution of the pin tip position as a function of time during forced heating under (black) no force or constant and (blue) 2.5 g and (green) 5.0 g forces applied. The heating procedures is as described: (dark red) 100% power for 10 s and (light red) 12% power. (c) Evolution of the pin position under (black) natural cooling and (blue) forced cooling. (d) Pin tip position during forced heating− forced cooling cycle under (black) no force or constant and (blue) 2.5 g and (green) 5.0 g forces applied. The heating procedure is as described previously. The forced cooling phase happens after 70 s and is shown in blue. (e) Pin tip displacement versus applied force. (f) Minimum (red circle) and maximum (blue square) forces exerted by the braille tip over 10 heating−cooling cycles. ..... 78
**Figure 2.13 :** (a, b) 3D temperature distribution for the single-pin braille device obtained from a COMSOL simulation operated at 12% heating power. (b) Temperature in the gel center along the vertical axis center at various heating powers: (blue) 12%, (purple) 20%, and (red) 30% power. Only a fraction of the gel was above the transition temperature (34 °C) and shrank. . 81
**Figure 2.14 :** Variation of the tip displacement amplitude for different heating powers: (red triangles) experimental measurement and (black squares) theoretical prediction based on COMSOL simulations. ..... 82
**Figure 3.1:** Optical microscope images of lines printed at 92.5 °C with a) 20, b) 30 and c) 40 kPa extrusion pressure. Optical microscope images of lines printed at 92.5 °C using 30 kPa pressure with d) 1, e) 5 and f) 7 mm/s printer head travel speed. ..... 93
**Figure 3.2:** SEM images of adjacent lines in the grid structured first layer of design printed using a) bidirectional, b) unidirectional printing. ..... 94
**Figure 3.3:** Schematic representation of a) drooping and b) non-drooping phenomena at the overhanging shellac lines. SEM images of 2 layers printed with using c) 0.2 and d) 0.3 mm as layer height ..... 95
**Figure 3.4:** Images of the a) 3D printer BioX (Cellink), b) grid design of the scaffold on Heartware software, c) photograph of the printed shellack scaffold with 0.3 mm horizontal distance between adjacent lines, d, e) perspective and top SEM image of the same scaffold' respectively. ..... 96

**Figure 3.5:** ) Schematic of the sample holder, images of the b) shrunk, c) swollen porous PNIPAM gel (50% v/v porous). $x_i$ represents the initial thickness of the gel while $x_f$ represents the final gel thickness.....98
**Figure 3.6:** Graphs showing the change in gel thickness with time during a) swelling and b) shrinking of HP-OR (Red square) and 3D printed porous gel (blue circle). .....100
**Figure 3.7:** Swelling a) and shrinking b) curves of 60% porous HP-OR gel (red) and 50 vol% porous 3D printed gel (blue). The initial slope (transient region) gives information on the diffusion coefficient of water through the gel matrix during swelling. Black dotted and dashed lines represent linear fit to the transient stage of the curves of HP-OR and 3D printed porous gel, respectively. .....102
**Figure 3.8:** Schematic of the a) gel container and the disc shaped gel sample, b) cross-section of the assembled gel container system with sample inside. .....104
**Figure 3.9:** a) Experimental setup for controlled flow of water through porous gel sample. b) A zoom in top view of the gel sample container and sensors used.....105
**Figure 3.10:** Graph depicting the change of flow rate of water (Q) with respect to the increasing (blue) and decreasing (red) pressure difference (ΔP) between inlet and outlet of the gel at RT. The dotted lines correspond to the linear fit applied at the data low pressure difference (<2500 Pa) region. .....107
**Figure 3.11:** Schematic of the gel compression against the outlet gel container wall upon high applied pressure ($P_{A)}$ on the inlet. .....108
**Figure 3.12:** Graph showing the solid displacement along the gel when compression started to occur at 2500 Pa pressure difference. .....109
**Figure 3.13:** Graphs depicting evolution of a) inlet/outlet temperature, b) pressure difference and c) flow rate of water through the gel with time upon introducing hot water (80 °C) to the system. The blue dotted line represents the moment temperature reached 34 °C (LCST) whereas the red dotted line represents the instant effect of shrinking gel started to occur on pressure gradient and fluid flow rate through the gel. .....111
**Figure 4.1 :** Images of the 4-point probe setup. The gel is sandwiched between two glass slides with symmetrical copper tapes. The probes are attached to the sourcemeter with alligator clips. .....121
**Figure 4.2 :** a) Images of the EDOT/NaPSS dispersions with different concentrations and polymerization conditions. b) Conductivity values of neat PAAc gel (red) and PAAc/PEDOT:PSS gels with standard dispersion and direct APS addition (Sample 1, yellow), diluted dispersion and direct APS addition (Sample 2, green), standard dispersion and separate

APS solution (Sample 3, blue), dilute dispersion and separate dilute APS solution (Sample 4, purple). ..... 123
**Figure 4.3 :** a) Conductivity values of PAAc/PEDOT:PSS gels after initial and second cycle of EDOT impregnation/polymerization processes. b) Images of the resulting gel samples.. 125
**Figure 4.4:** Images of the a) UV polymerized PEDOT:PSS/PAAc gels b) neat agarose, 0.5wt. % PEDOT:PSS/Agarose gels c) conductivity values of the 0.1 wt. % (red), 0.25 wt. % (orange), 0.5 wt. % (yellow) PEDOT:PSS containing UV polymerized PAAc gels and neat (green), 0.5 wt. % PEDOT:PSS containing (blue) agarose gels. ..... 127
**Figure 4.5:** Preparation steps of the PEDOT:PSS/PAAc double network gel. Images of a) the gellified PEDOT:PSS dispersion injected in the PP tubing, b) PEDOT:PSS gel after heating at 75°C for 1 h, c) PEDOT:PSS gels soaked in the AAc monomer solution and d) PEDOT:PSS/PAAc DN gels with average swollen diameter of 1.6 mm after polymerization of the AAc monomers. ..... 128
**Figure 4.6 :** Electronic conductivity values of thin (1.6 mm in diameter) PEDOT:PSS/PAAc DN gel (purple), b) thick (3.5 mm in diameter) PEDOT:PSS/PAAc DN gel (blue) and PEDOT:PSS/PAAm DN gel (green). ..... 128
**Figure 4.7:** Cyclic voltammetry graphs in which 0.01 M KCl solution is utilized as the electrolyte, potential window of ±0.7 V applied on a), b) PEDOT:PSS/PAAc gel, c), d) PEDOT:PSS/PAAm gel, e), f) PEDOT/PVDF membrane with 10, 100 mV/s rates, respectively. ..... 131
**Figure 4.8:** Cyclic voltammetry graphs in which 0.01 M $CuCl_2$ solution is utilized as the electrolyte, potential window of ±0.7 V applied on a), b) PEDOT:PSS/PAAc gel, c), d) PEDOT:PSS/PAAm gel, e), f) PEDOT/PVDF membrane with 10, 100 mV/s rates, respectively. ..... 133
**Figure 4.9:** a) Images of the PEDOT:PSS/PAAc gel before/after subjected to CV tests with different voltage rates and potential windows. ..... 134
**Figure 4.10:** Cross-sectional SEM images and elemental EDX analysis results after soaking a) PAAc and b) PAAm DN gel into $CuCl_2$ solution. After conducting chronoamperometry with applied potential of 0.2V and 1.0V to the b,c) PEDOT:PSS/PAAc , e,f) PEDOT:PSS/PAAm gels. All gels are washed and dried before analysis..... 136
**Figure 4.11:** SEM images of the DN microporous gels..... 137
**Figure 4.12:** Bar graph with a log scale depicting the conductivity values of the acid treated PEDOT:PSS gel (18 M sulfuric acid treated) (red, sample 1), PEDOT:PSS/PAAc DN gel (light green, sample 2), PEDOT:PSS/PAAm DN gel (dark green, sample 3), macroporous

PEDOT:PSS gel (orange, sample 4), macroporous PEDOT:PSS/PAAc DN gel (light blue, sample 5) and macroporous PEDOT:PSS/PAAm DN gel (dark blue, sample 6). ..... 138
**Figure 4.13:** Bar graphs (log scale) depicting the specific capacitance values of DN PEDOT:PSS/PAAc, PEDOT:PSS/PAAm gel, PEDOT coated PVDF membrane, macroporous PEDOT:PSS and PEDOT:PSS/PAAc, PEDOT:PSS/PAAm DN gel samples measured from CV test results conducted in 0.01 M a) KCl and b) $CuCl_2$ solutions. ..... 139
**Figure 4.14:** Graphs showing the volume change of the 3M PAAc gel initially at a) pH 3, b) pH 6 and 0.7M gels initially at c) pH 3 and d) pH 6..... 141
**Figure A.1:** Schematic representation of macroporous HP-OR gel preparation based on PMMA spherical micro particles. ..... 152
**Figure A.2:** Schematic representation of macroporous HP-OR gel preparation based on PMMA spherical micro particles. ..... 153
**Figure A.3:** a) Mark-10 ESM301 mechanical testing machine. b) Compression stages of HP-OR gel. ..... 154
**Figure A.4:** Images of the AR-2000X rheometer and the schematic of the cone head used on the PEDOT:PSS dispersion..... 157
**Figure A.5:** Strain sweeping test results in the range 0-5 % strain at a) 1Hz, b) 10 Hz and c) 100 Hz oscillation frequency. Graphs depicting change of storage modulus (G') with respect to time with different applied d) temperatures, e) two-step heating from 55 to 75°C program sulfuric and f) acid concentrations. ..... 159
**Figure A.6:** a-c) UV-Vis spectrums of pristine, EDTA and DDTC/SDS containing copper solutions. d-f) Calibration curves obtained for different copper ion concentration regions with different chemical complexes ..... 163

# Table of Tables

**Table 1.1:** Features of some dynamic tactile devices.....15
**Table 2.1:** Shrinking/Re-swelling and modulus data of Porous PNIPAM gel samples.....70
**Table 4.1:** Samples for EDOT:PSS polymerization inside pre-polymerized PAAc matrix. 121
**Table 4.2:** The sulphur atom traces obtained by EDX analysis on the cross-section of gel samples.....124

# General Introduction

Actuators are the systems which convert any kind of input energy (electric, heat, light) into mechanical motion. Actuation technology has been developing greatly especially since the industrial revolution in the 18$^{th}$ century. Electrical motors and pneumatic/hydraulic systems have been the main actuation mechanism in such large mechanical systems. Electric motors utilize the electrically driven rotational motion to actuate either linear or rotary controlled actuation. On the other hand, pneumatic/hydraulic systems are based on the energy transfer between pressurized liquids or gases in closed chambers to produce motion. Either of these systems which require complex, bulky structuration perform precise and efficiently controlled actuation in large systems.

On the other hand, the developing technology requires miniaturizations of the overall systems as well as the actuators to micron (MEMS) or even nanometer (NEMS) scales. The complex and multi-component classical actuation systems are not suited for efficient downscaling. Currently, piezoelectric actuators are the key technology for miniaturized systems. Piezoelectric systems rely on materials that can convert applied electricity to mechanical stress or vice-versa. They are being used today in many applications such as aerospace [1], atomic force microscopy (AFM) [2,3], precision machining [4] and even micro electro-mechanical systems (MEMS) [5]. Piezo-electric actuators offer very precise control over the actuation and can be easily down-scaled. Nevertheless, piezoelectric materials produce low actuation amplitudes (working stroke) which limits its efficiency. Low actuation amplitudes limit the acquired range of motion to 10-100 μm for linear and several mm for bending motions from a single actuator. To overcome such limitations, cantilever or stepping systems are used which require complex and bulky structures. Additionally, the dynamic characteristic of the piezo-electric actuator is decreased as the size of the amplifying mechanism is increased. So, we need to use other active materials which produce sufficient physical responses to obtain simpler actuation mechanisms.

Active materials have the ability to modify their structure both at molecular and macroscopic scale to give physical responses to environmental stimuli such as light, pH, temperature, magnetic or electric field. Therefore, they are often called smart materials. Such active physical responses can be rephrased as conversion of different types of external energy into mechanical motion which is the base principal of actuation.

As the complexity of the controlled motion increases which requires whole lot more actuators or the size of the overall system decreases, the limitations of down scalability becomes problematic. Thus, soft materials are crucial in filling the gap left by the conventional active materials as the technological progress favors smaller, softer and lighter systems. The key attribute of soft materials in such situation is the extreme adaptability due to the elastic nature overcoming the size and weight limitations.

Today's technology prefers smaller, softer and more efficient systems. Such systems mimic the nature which operates with maximum efficiencies. The most important parameter affecting the actuation efficiency is the working stroke for such systems as the overall size is limited. On the other hand, actuators from soft polymeric materials are being developed that have higher actuation amplitude, and energy/work density than the commercial systems.

The term "soft" has been widely referred to the materials with elastic moduli in the range of soft tissues (<$10^9$ Pa) in our bodies such as skin, organs, muscles, etc. (Fig. 1.0). The polymeric actuators have elastic moduli very close to the biological tissues.

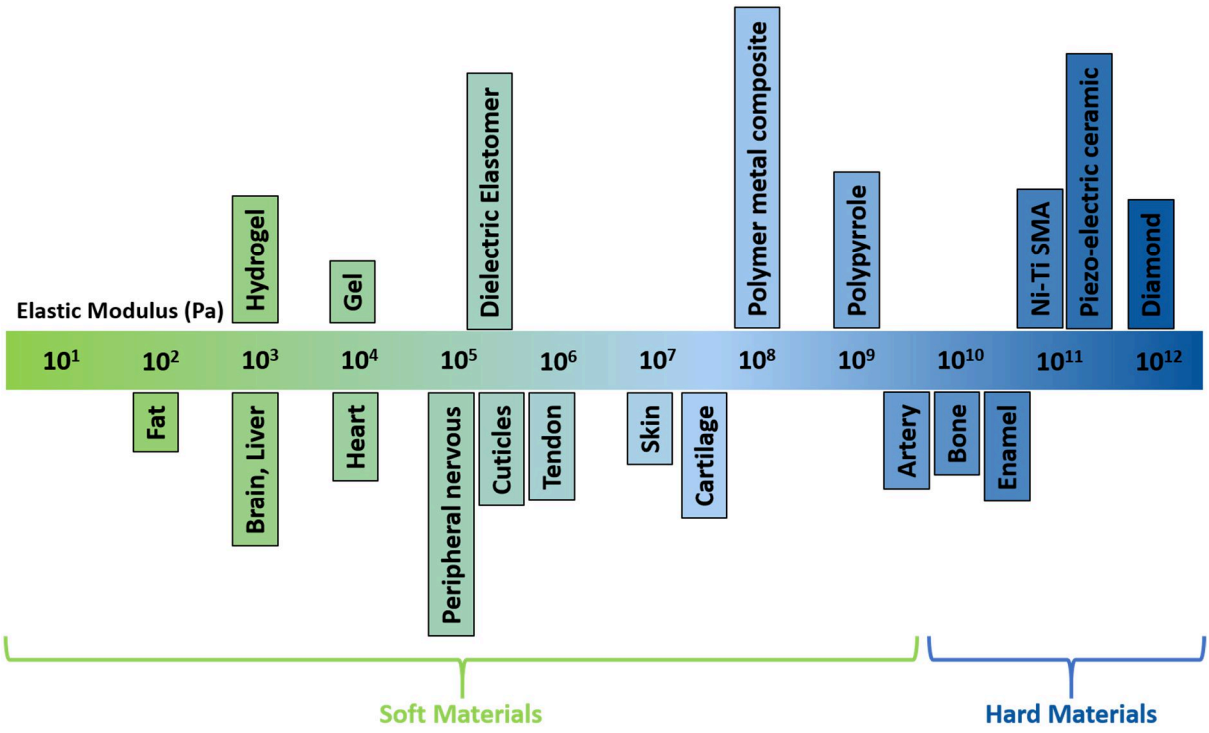



**Figure 1.0:** Spectrum of materials according to their elastic moduli.

In the first chapter, we introduce the current state of the soft and smart materials in the actuator technology. We point out some specific actuator applications which can benefit from the advantages of soft materials. Later, we focus on smart hydrogels which is the focal point of this

thesis. We also signify the unique poroelastic properties of hydrogels which gives more insight on its capabilities as actuators.

In the second chapter, we explore a new actuation strategy using mechanically active gels that are called smart gels [6–8]. We particularly focused on thermo-sensitive gels based on poly(N-isopropylacrylamide) (PNIPAM) [9,10]. The PNIPAM gel shows a volume phase transition with temperature. For temperatures above 34 °C, the PNIPAM gel shrinks reversibly with a very large swelling ratio (i.e., volume ratio between a swollen and shrunk gel sample), which can reach 1000%. PNIPAM gel shows several key characteristics suitable for development of a smart braille tablet. Thanks to the very large swelling ratio, only a small quantity of active material is required to produce a large enough displacement (actuation). Furthermore, controlling the actuation only requires local control of the temperature. It can also be implemented relatively easily with small heating resistances. Furthermore, the low-temperature transition (below 40 °C) is user-friendly and safe with no risk of burning the user's finger.

Hydrogels face two major limitations for actuation: the high fragility of the polymer matrix and very slow response to stimuli. In this study, we combine two recent developments to overcome these limitations. The first development is the synthesis of a hydrogel with improved mechanical robustness [11–15] often called a tough gel. The second development is the synthesis of a fast-reacting gel with a macroporous structure [16]. These two scientific leaps which make a smart gel adapted to soft actuation are applied and results are described below.

For introducing macroporosity to the gels, we used scaffolding method. In this method, a sacrificial scaffold is produced with the desired pore shape and density. As the gel is polymerized and cross-linked around the scaffold, after selectively dissolving the scaffold material, a porous gel is acquired.

Ultimately in this chapter, we developed a fast actuating PNIPAM gel with high cyclic performance and a single pin Braille device, enabling swift temperature control of the macroporous gel cylinder. We introduced a simple and cost-efficient alternative to existing actuators for Braille devices.

In the third chapter, we demonstrate our studies conducted to investigate the poroelastic properties of macroporous PNIPAM hydrogel. Attaining full control over the pore geometry and the level of gel porosity was crucial to thoroughly analyze the poroelastic properties of hydrogels. Thus, we first developed a novel sacrificial scaffold from shellac by melt extrusion 3D printing method. By using such method, we were able to achieve porosities in the range of

30-50 % (v/v) in the gel matrix. Moreover, we conducted the same imaging method mentioned in the previous chapter on 60% porous gels produced by PMMA templates and 50% porous gel produced with 3D printed scaffold. We calculated the diffusion constant of water through the gel during swelling with the help of the Biot's theory of poroelasticity. Lastly, we constructed an experimental setup and obtained a controlled (water pressure and temperature) flow through macroporous gel matrix. Since diffusion of water through the poroelastic matrix obeys the Darcy's law, flow rate of water is directly related to the pressure field gradient, viscosity of water and the permeability of the gel. Using such relation, we were able to acquire the permeability data of the macroporous gel. Moreover, we also observed and analyzed the poroelastic deformation of the gel upon compression by the fluid flow. By flowing hot water through the gel, we were able to obtain the evolution of pressure gradient, decreasing flow rate and eventually the change in water permeability of the gel upon shrinking.

In the last chapter, we demonstrate the studies conducted to develop a chemically active and electrically controllable hydrogel actuator. In order to achieve such purpose, there are several properties required from the hydrogel. These properties are chemical sensitivity, electronic conductivity and reversible actuation. Moreover, proper working conditions for the hydrogel should be investigated to achieve efficient and reversible actuation. PAAc is known to be chemically sensitive towards metallic ions such as $Cu^{2+}$ or $Ag^{+}$, The AAc molecules are known to form complexes with these metallic ions and shrink. Hence, we used PAAc as our chemically sensitive hydrogel throughout the study. Electronic conductivity was required from the hydrogel in order to be able to trigger actuation with electricity. Thus, our initial step towards developing such material was to introduce conductivity to the hydrogel matrix. We aimed to utilize an intrinsically conductive gel PEDOT:PSS and obtain a double network hydrogel system in which electricity could travel through the conductive secondary network. In the first section of this chapter we demonstrate three different strategies to acquire a double network hydrogel. These methods are polymerizing either EDOT/AAc monomers inside the chemically crosslinked counter gel or polymerizing AAc monomers inside physically crosslinked PEDOT:PSS gel matrix. After achieving electronic conductivity ($\geq 10^{-3}$ $S.cm^{-1}$) in the double network hydrogel, in the second part of this chapter we investigated its electrochemical properties such as capacitance to reveal the efficiency of ion transfer in/out upon electrical trigger. Finally, we investigated the complexation efficiency and reversibility upon introduction of $Cu^{2+}$ ions to PAAc hydrogel. The key aspect was to determine the amount of metallic ion required to acquire significant reversible actuation. Thus, we observed the shrinking/re-

swelling dynamics of PAAc gel upon introduction of different ion concentrations and the changes in solution pH/conductivity after complexation. Nevertheless, for more elaborative results such as the critical ion concentration required for full shrinking of the PAAc gel we used complexometric spectroscopy method.

To summarize, we developed fast actuating hydrogel actuators and investigated the applicability of such material in Braille device and artificial muscle applications. We revealed that there are several limitations on the controlling and production methods of such materials. Nevertheless, smart hydrogels pose great potential for future actuator technologies with its high actuation stroke to volume, elasticity and processability properties. Because actuation technology always pursues, smaller, more efficient and adaptive systems to develop a better world.

## REFERENCES


[1] H. Elahi, M. Eugeni, P. Gaudenzi, F. Qayyum, R.F. Swati, H.M. Khan, Response of piezoelectric materials on thermomechanical shocking and electrical shocking for aerospace applications, Microsyst. Technol. 24 (2018) 3791–3798. https://doi.org/10.1007/s00542-018-3856-8.

[2] H. Habibullah, 30 Years of atomic force microscopy: Creep, hysteresis, cross-coupling, and vibration problems of piezoelectric tube scanners, Meas. J. Int. Meas. Confed. 159 (2020) 107776. https://doi.org/10.1016/j.measurement.2020.107776.

[3] M.G. Ruppert, S.I. Moore, M. Zawierta, A.J. Fleming, G. Putrino, Y.K. Yong, Multimodal atomic force microscopy with optimized higher eigenmode sensitivity using on-chip piezoelectric actuation and sensing, Nanotechnology. 30 (2019). https://doi.org/10.1088/1361-6528/aae40b.

[4] Z. Zhu, X. Zhou, Z. Liu, R. Wang, L. Zhu, Development of a piezoelectrically actuated two-degree-of-freedom fast tool servo with decoupled motions for micro-/nanomachining, Precis. Eng. 38 (2014) 809–820. https://doi.org/10.1016/j.precisioneng.2014.04.009.

[5] J. Johari, J. Yunas, B.Y. Majlis, Piezoeletric micropump for drug delivery system fabricated using two optical masks, Adv. Mater. Res. 74 (2009) 279–282. https://doi.org/10.4028/www.scientific.net/AMR.74.279.

[6] E.S. Gil, S.M. Hudson, Stimuli-responsive polymers and their bioconjugates, Prog. Polym. Sci. 29 (2004) 1173–1222. https://doi.org/10.1016/j.progpolymsci.2004.08.003.

[7] S.-K. Ahn, R.M. Kasi, S.-C. Kim, N. Sharma, Y. Zhou, Stimuli-responsive polymer gels, Soft Matter. 4 (2008) 1151. https://doi.org/10.1039/b714376a.

[8] L. Ionov, Polymeric Actuators, Langmuir. 31 (2015) 5015–5024. https://doi.org/10.1021/la503407z.

[9] M.A. Haq, Y. Su, D. Wang, Mechanical properties of PNIPAM based hydrogels: A review, Mater. Sci. Eng. C. 70 (2017) 842–855. https://doi.org/10.1016/j.msec.2016.09.081.

[10] J. Liu, L. Jiang, S. He, J. Zhang, W. Shao, Recent progress in PNIPAM-based multi-responsive actuators: A mini-review, Chem. Eng. J. 433 (2022) 133496. https://doi.org/10.1016/j.cej.2021.133496.

[11] J.P. Gong, Y. Katsuyama, T. Kurokawa, Y. Osada, Double-network hydrogels with extremely high mechanical strength, Adv. Mater. 15 (2003) 1155–1158. https://doi.org/10.1002/adma.200304907.

[12] W.J. Zheng, N. An, J.H. Yang, J. Zhou, Y.M. Chen, Tough Al-alginate/Poly(N -isopropylacrylamide) hydrogel with tunable LCST for soft robotics, ACS Appl. Mater. Interfaces. 7 (2015) 1758–1764. https://doi.org/10.1021/am507339r.

[13] Q. Chen, H. Chen, L. Zhu, J. Zheng, Fundamentals of double network hydrogels, J. Mater. Chem. B. 3 (2015) 3645–3886. https://doi.org/10.1039/C5TB00123D.

[14] E.S. Gil, S.M. Hudson, Effect of silk fibroin interpenetrating networks on swelling/deswelling kinetics and rheological properties of poly(N-isopropylacrylamide) hydrogels, Biomacromolecules. 8 (2007) 258–264. https://doi.org/10.1021/bm060543m.

[15] J. Wang, L. Lin, Q. Cheng, L. Jiang, A strong bio-inspired layered PNIPAM-clay nanocomposite hydrogel, Angew. Chemie - Int. Ed. 51 (2012) 4676–4680. https://doi.org/10.1002/anie.201200267.

[16] H. Warren, D.J. Shepherd, M. in het Panhuis, D.L. Officer, G.M. Spinks, Porous PNIPAm hydrogels: Overcoming diffusion-governed hydrogel actuation, Sensors Actuators, A Phys. 301 (2020) 111784. https://doi.org/10.1016/j.sna.2019.111784.

# Introduction

## 1.1. Actuation Technology in Micro-Millimeter Systems

Actuators are the systems which convert any kind of input energy (electric, heat, light) into mechanical motion. Actuation technology has been developing greatly especially since the industrial revolution in the 18$^{th}$ century. Electrical motors and pneumatic/hydraulic systems have been the main actuation mechanism in such large mechanical systems. Electric motors utilize the electrically driven rotational motion to actuate either linear or rotary controlled actuation. On the other hand, pneumatic/hydraulic systems are based on the energy transfer between pressurized liquids or gases in closed chambers to produce motion. Either of these systems which require complex, bulky structuration perform precise and efficiently controlled actuation in large systems.

The developing technology requires miniaturizations of the overall systems as well as the actuators to micron (MEMS) or even nanometer (NEMS) scales. The complex and multi-component classical actuation systems are not suited for efficient downscaling. Currently, piezoelectric actuators are the key technology for miniaturized systems. Piezoelectric systems rely on materials that can convert applied electricity to mechanical stress or vice-versa. They are being used today in many applications such as aerospace [1], atomic force microscopy (AFM) [2,3], precision machining [4] and even micro electro-mechanical systems (MEMS) [5]. Piezo-electric actuators offer very precise control over the actuation and can be easily down-scaled.

Nevertheless, piezoelectric materials produce low actuation amplitudes (working stroke) which limits its efficiency. Low actuation amplitudes limit the acquired range of motion to 10-100 μm for linear and several mm for bending motions from a single actuator.

To overcome such limitation, several methods have been used. For example, compliant mechanical systems such as cantilevers are used to amplify the working stroke. As a result, very bulky systems much bigger than the size of the utilized piezo-electric material is required. Additionally, the dynamic characteristic of the piezo-electric actuator is decreased as the size of the amplifying mechanism is increased. Another way to achieve higher working stroke is stepping which is utilizing accumulation of small motions by rotors. Such method requires the

usage of servo-control systems and rotors additional to the piezo-electric material again increasing the overall complexity of the actuation system.

Today's technology prefers smaller, softer and more efficient systems. Such systems mimic the nature which operates with maximum efficiencies. The most important parameter affecting the actuation efficiency is the working stroke for such systems as the overall size is limited. On the other hand, actuators from soft polymeric materials are being developed that have higher actuation amplitude, and energy/work density than the commercial systems.

The term "soft" has been widely referred to the materials with elastic moduli in the range of soft tissues (<$10^9$ Pa) in our bodies such as skin, organs, muscles, etc. (Fig. 1.1). The polymeric actuators have elastic moduli very close to the biological tissues.

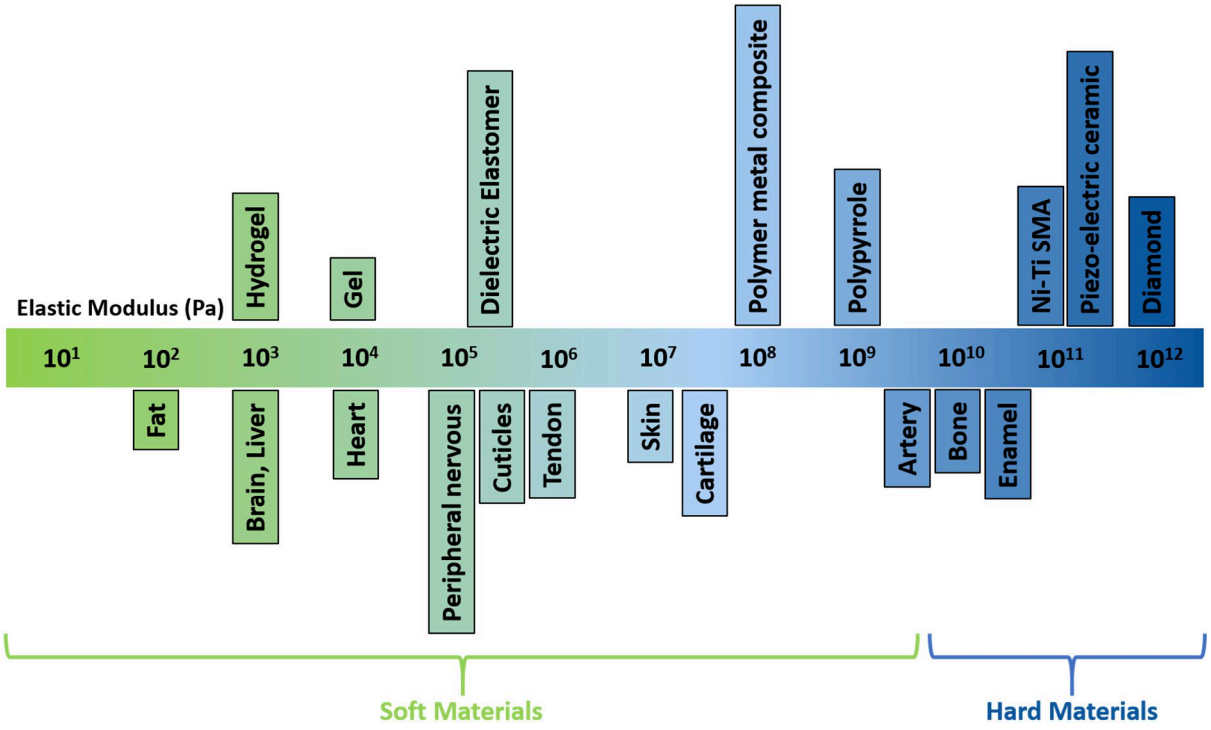



**Figure 1.1:** Spectrum of materials according to their elastic moduli.

The polymeric materials are being utilized in actuation systems as new smart materials or systems producing higher working stroke can be achieved. Such actuators can be classified into two as tethered and untethered in terms of the source of actuation.

In tethered actuators, polymeric soft materials which are not intrinsically active are only used due to their elastic properties [6]. Such systems generally rely on the conventional actuation mechanisms such as hydraulic or pneumatic. A perfect example for a tethered soft

actuator would be the pneumatic tendon-driven gripper utilizing silicone as the soft material. In this system, a special tendon shape was given to the silicone so any vacuum created inside would result in bending motion towards the tendons direction (Fig. 1.2). This can be realized as a perfect example for a tethered system since silicone does not possess any intrinsic active (smart) features but its elasticity permits such actuation through external forces [7].

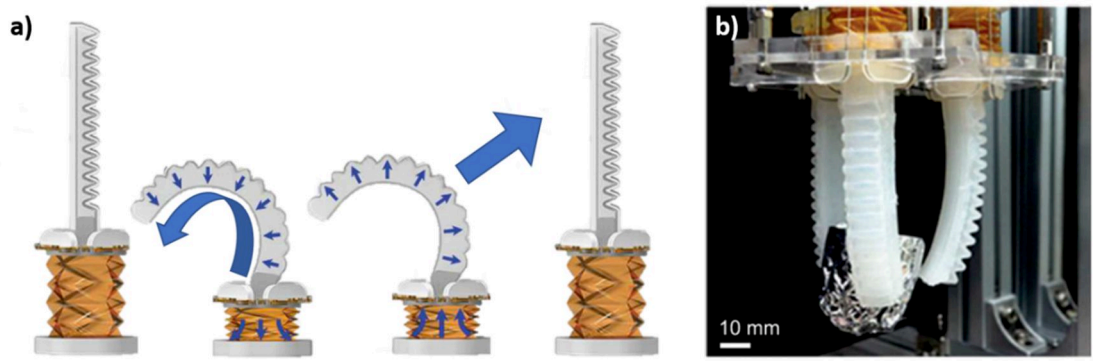



**Figure 1.2:** a) Contraction and opening of the tendon shaped silicone actuator upon negative and positive pressure inside, relatively) The three-armed gripper grasping an aluminum cup [7].

On the other hand, untethered actuators utilize solely the intrinsically active soft material for converting the energy into a mechanical motion. In other words, the mechanical response is not due to the any external force but the intrinsic properties of the active soft material. Dielectric elastomers (DEAs), shape memory polymers (SMPs), conductive polymers (CPs), liquid crystal elastomers (LCEs) and hydrogels are example to intrinsically active materials.

## 1.2. Need of Small Actuators in Haptic Technology

Haptic technology is based on transmission of information through touch perception which is one of the 5 main human senses. We perceive touch through our sensory organ skin which can detect stimuli such as applied pressure, motion and temperature. Thus, these stimuli are the primary channels to transfer information.

Studies in haptic technology has increased in the last decade due to the interest in virtual or augmented reality applications but the original challenge has been development of Braille devices. The very origin of haptic technology emerged from the need of conveying electronic information to the visually impaired individuals. Braille devices are made of retractable pins which can move up/down to convey Braille alphabet characters.

As simple as it sounds, today these devices cost thousands of euros and can only show several characters at once. The bottleneck of the technology is the actuation systems since a competent device which can not only convey a whole page full of sentences at once but also images requires thousands of pins to move independently. This means small actuators with large working strokes are required. Currently, commercial devices utilize piezo-electric actuators which results in bulky, complicated and thus, expensive systems.

Although there is no technology today answering this challenge, with the development of polymeric actuators there have been many studies in order to come with a simpler and cheaper alternative. In the following paragraphs we will explore possible solutions by emphasizing key problems.

### 1.2.1. Braille Alphabet and Current Electronic Braille Devices

Since the invention of writing in 3200 BCE by Sumerians in Mesopotamia, the primary access to knowledge has been through literacy. Unfortunately, visually impaired individuals have been precluded from not only visuality of the world but also knowledge through literature. This is because no universal alphabetical system was invented specifically adapted for visually impaired people until the invention of Braille alphabet in the 19$^{th}$ century.

Braille alphabet is a tactile writing system for visually impaired individuals. It was invented by a Frenchman named Louis Braille (1809-1852) at the age of fifteen. He was inspired by the alphabet found by Charles Barbier de la Serre (1767-1841) who created a tactile language system (night writing) for the secret military usage [8].

Braille characters (Fig. 1.3a) consists of six raised dots arranged in the form of 3x2 matrix which is called a braille cell. The original Braille alphabet consisted of 26 characters as in the French alphabet but today it is transcribed to over 133 languages and is considered the standard tactile alphabet.

There have been slight differences due to the adaptation of the Braille alphabet to different languages comprising of additional letters and signs to the French alphabet. Thus, there have been different standardizations for different countries. The same differentiation is also true for the size and spacing of the Braille. For example, according to the French standard, horizontal/vertical dot to dot distance should be 2.5-2.6 mm with dots having 1.2 mm of base diameter and 0.8-1.0 mm height. Distance between lines should be 10 mm.

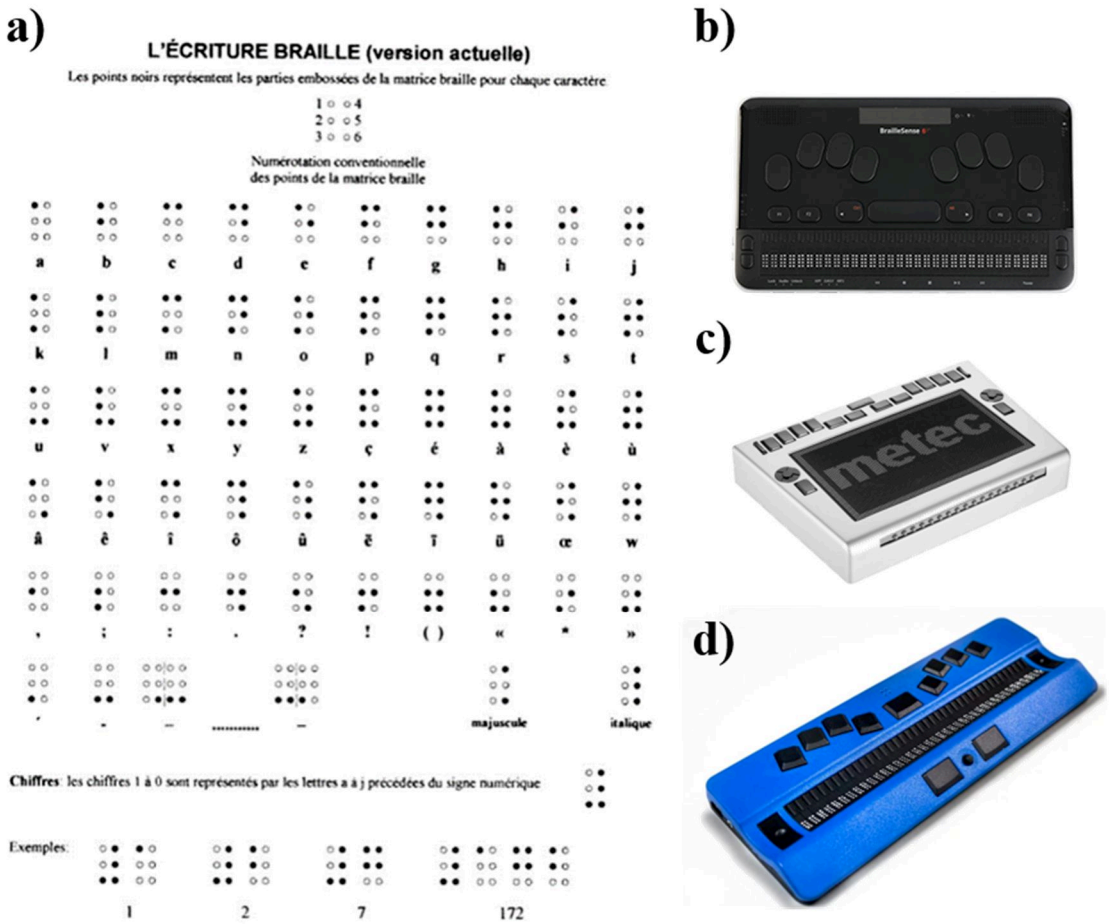



**Figure 1.3:** a) The Braille alphabet in its current form [8]. Commercial Braille displays a) BrailleSense-6, b) Hyperbraille-F and c) ActiveBraille.

With the invention of personal computers, electronic devices started to play a key role in information transfer. Thus, the biggest concern for visually impaired individuals for the last 40 years has become accessing such electronic information. Development of touch screens and its wide spread implementation to electronic devices certainly worsened the situation.

Thus, paperless electronic Braille devices are being developed which can dynamically display Braille characters. On such a device, pins that can reversibly protrude/retract on a surface mimics Braille dots. With such refreshable display provides dynamic reading experience. Actuation of such protrusion/retraction motion requires high precision in order to eliminate errors caused by misperception by touch sensing. Thus, there are also some common properties for dynamic tactile displays based on average human touch perception capabilities. One of these properties are typical dot maximum pin height of $0.7 \pm 0.05$ mm in the protruded state. It is preferred that the pins rest below the reading surface in the retracted state but most commercial devices keep pins at height of 0.25 mm above the surface in their resting state. Pin diameter of 0.5 mm is typically preferred with pin to pin distance of 2.3 mm. Cell to cell distance should be 6.1-6.5 mm. The average force applied by a finger during reading is determined to be 5g for light touch readers while 15g is considered to be maximum. It is stated that a protruded height of 0.25 should be remaining under force for better user experience. Lastly, refresh rate of 1 Hz is considered tolerable for reading long texts but 10 Hz is considered for most devices [9,10].

The bottleneck of this technology has always been the actuation system. The complexity, size and cost of the actuation mechanism of a single pin determines the reparability, bulkiness and production cost of the whole device. It is because a decent Braille system requires movement of 1000s of pins independently. Piezo-electric ceramic bimorph actuators have been extensively utilized for commercial devices due to its precision and cyclic stability. The downside of such actuation is the complexity and bulkiness it induces. Piezo-electric actuators require cantilever to amplify the limited actuation strain which increases the overall size of the device reducing portability. Moreover, the electronic circuitry required for precise electrical triggering results in very complex and expensive system. The majority of commercial Braille displays can only display 10 to 20 Braille characters and cost thousands of euros limiting their affordability [9,11].Other actuation mechanisms were developed such as pneumatic [12], magnetic [13]or shape memory actuators [14] but none of them are commercial yet. Table 1.1 provides a summary of the key capabilities of different systems.

**Table 1.1:** Features of some dynamic tactile devices.

| Product | Actuation Type | # of tactile dots (pins) | Pin Stroke (mm) | Refresh time (ms) |
|---|---|---|---|---|
| Hyperbraille-F [15] | Piezo-electric | 140x60 | 0.7 | <25 |
| Graphiti [16] | Piezo-electric | 60x40 | 0.7 | 37 |
| Dot Cell [17] | Electromagnetic | scalable | 0.6 | >600 |
| SMA-Blind [14] | Shape Memory Alloy | 10x10 | 2 | 300 |
| SMP-Blind [18] | Shape Memory Polymer | 4x4 | 0.33 | 5000 |
| DE-Blind [19] | Dielectric Elastomer | 4x2 | 0.75 | 2000 |
| Pneu-Blind [20] | Pneumatic | 7x8 | 0.75 | 600 |
| Kit-Blind [13] | Electromagnetic | 12x16 | 0.8 | 5 |

### 1.2.2. Key Actuation Technologies for Commercial Braille Devices

Commercial Braille devices today, utilize well known actuation technologies such as pizeo-electric materials, pneumatic systems, magnetic actuators or shape memory alloys. Although production of these systems is well established through the years and they provide good control of the actuation, their common downsides are their complexity, bulkiness and thus high production costs. Nevertheless, they constitute the majority of the commercial Braille device market. In the coming paragraphs we will discuss the working mechanism of each system and point out their limitations.

#### 1.2.2.1. Piezo-electric Actuators for Braille Devices

Piezo-electric materials have the ability of generating small physical deformations upon application of high electrical potentials (50-200V). Piezo-electricity is generally associated with crystalline inorganic materials (quartz) or ceramics such as lead zirconate titanate, potassium niobate[5,21]. Polymeric materials such as polyvinylidene fluoride (PVDF) or polyvinylidene chloride (PVDC) also show pizeo-electric property [22]. The piezo-response of

such polymers are not as significant as crystalline or ceramic materials but the elasticity, light weight and biocompatibility make them low cost, low power consuming alternatives.

Majority of the pizeo-electric actuators for Braille devices are in the form of bimorphs which is a cantilever comprised of two active pizeo-electric layers. Upon introduction of voltage, one layer contracts while the other expands generating actuation. Such systems require several centimeters of length to be able to produce enough actuation for a Braille dot which has been around 0.25-0.5 mm [10]. Additionally, such actuators require high voltage circuitry (200V) both due to complex control system and low actuation efficiency. Thus, very complicated and bulky systems are required resulting in high production cost and low robustness (Fig.1.4). For example, Graphiti and HyperBraille-F are commercial Braille devices utilizing pizeoelectric actuators and weight 4, 4.3 kg, respectively [11].

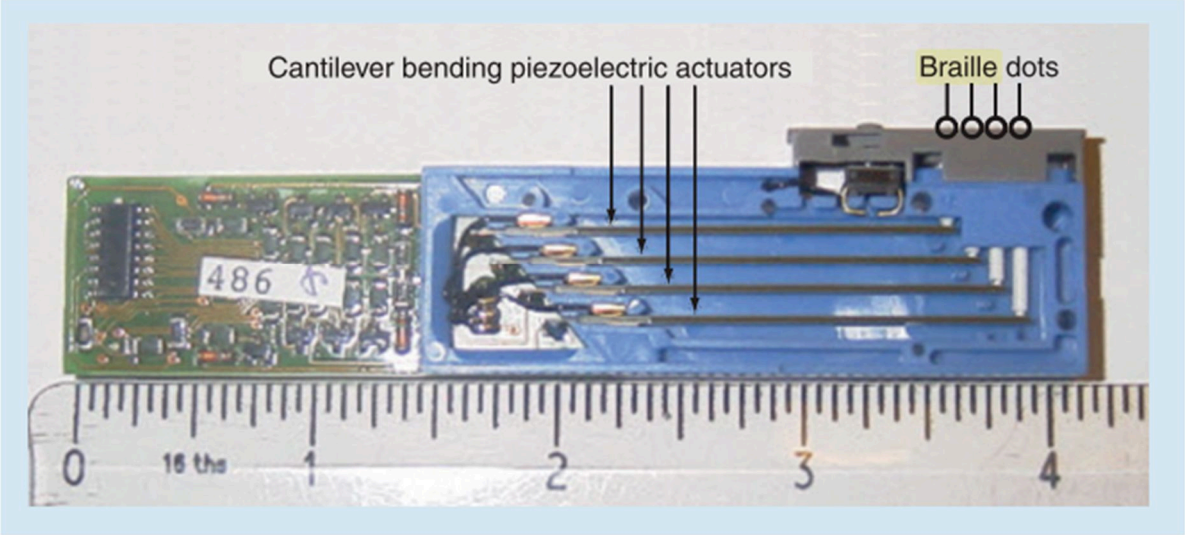



**Figure 1.4:** Lateral view of a typical piezo bimorph Braille Cell [9].

#### 1.2.2.2. Pneumatic Actuators for Braille Devices

Pneumatic actuation is another option for Braille devices. Actuation systems depends on conversion of energy from pressurized air or fluids to mechanical motion. The actuation mechanism relies on channel systems made out of elastomeric materials which are called pneumatic manifolds. This strategy is an alternative to the pizeo-electric system. Several Braille systems have been built based on pneumatic actuation [10,20].

The main drawback is the need for a complicated fluidic channel system (manifold) in which fluid/air pressure should be controlled and requirement for many pumps and valves.

These in turn, affect the overall complexity of the system. Thus, decrease the reparability, controllability and increase the production cost and overall size.

The advances in microfluidics based technology in the last decade enables fabrication of microchannel systems (manifold) with complex structures with methods such multi-layer soft lithography [10]. This way not only the multichannel systems are produced more easily and precise but also the overall size is reduced. Nevertheless, building a Braille device with large numbers of pins remain a challenge since each pin requires individual channel system which exceeds the limits of microfluidic technology.

Moreover, requirement for pressure adjustment remains and brings the pumps/valves into the system (Fig. 1.5). Each pin requires independent pressurization system to be controlled independently which means separate valve and pump is required. Thus, bulkiness is still the biggest drawback of pneumatic actuator based Braille devices. As can be seen in Figure 1.5b, pressure control unit is very bulky. It is also important to emphasize that precise pressure control systems are very expensive and complex to repair.

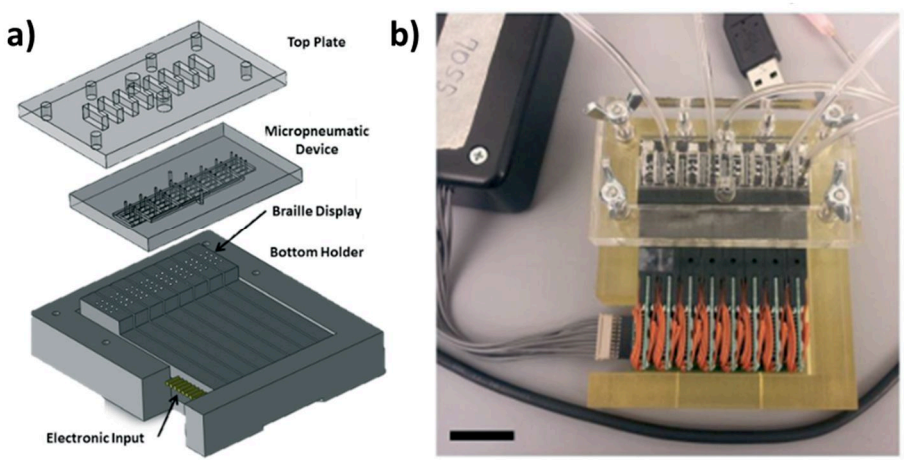



**Figure 1.5:** (a) Braille display with a micro-pneumatic channel (manifold) system, (b) Braille setup with five connected tubes (one for pressure input, four for different output tubes) [10].

#### 1.2.2.3. Magnetic Actuators for Braille Devices

Magnetic materials are also utilized to actuate Braille pins. The method is developed as an alternative to pizeo-electric system. The main principal of the system is to utilize the axial magnetic force exerted by the current run through a solenoid coil. By placing a magnet or a paramagnetic material at the center of a solenoid coil, the motion of such component in the vertical axis can easily be controlled via the direction of current passing through the coil.

Such system can be classified as an electric motor but a linear actuation is obtained without the need of a rotational one. As all electric motor systems, miniaturization is again problematic since system requires many complex structures. There have been studies on overcoming such limitation by using stacked printed circuit boards (PCB) to form solenoid structure but the complexity is still problematic [23]. Thousands of pins with individual magnetic control and actuation systems require sophisticated microfabrication processes which significantly increase the production cost of the Braille device. The low reparability of the systems is another limitation to commercial feasibility of such devices.

Zarate and Shea (2017) have developed a Braille device by utilizing pot-magnets. A magnet was placed over a solenoid coil made of copper wires (Fig 1.6a). By running current through the solenoid, a magnetic force pushing the magnet upwards was generated. Fabrication of small and sophisticated components such as solenoids, magnets and membranes increase the production cost while increasing the level of complication in reparations. Such system does not have the problem of bulkiness as much as the piezo-electric or pneumatic actuators but the production cost and poor reparability remains.

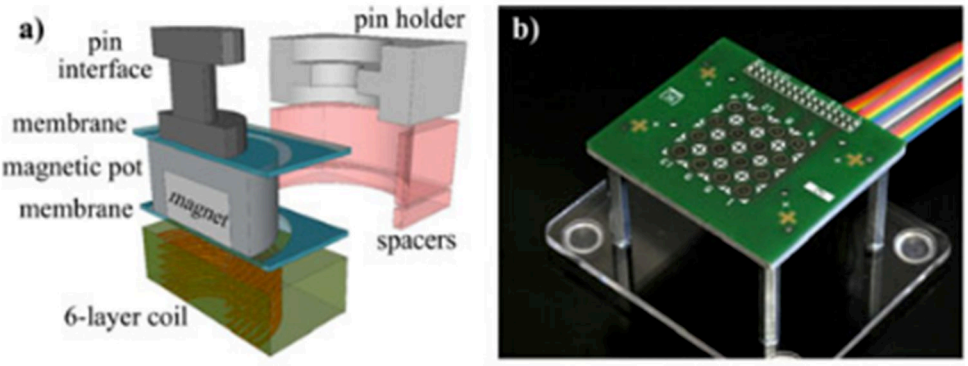



**Figure 1.6**: (a) Schematic of the single pin magnetic actuation components, (b) PCB containing 4x4 haptic display [13].

In another study, the same electro magnetization principal was utilized for actuation but rather than a metallic magnet, a soft magnetic material was used which was actuated by several vertically aligned PCBs which formed solenoids (Fig. 1.7). This way the cost for the manufacturing and assembly of solenoid system was decreased but the complexity, sensitivity and low reparability problems remained due to the actuation method [23].

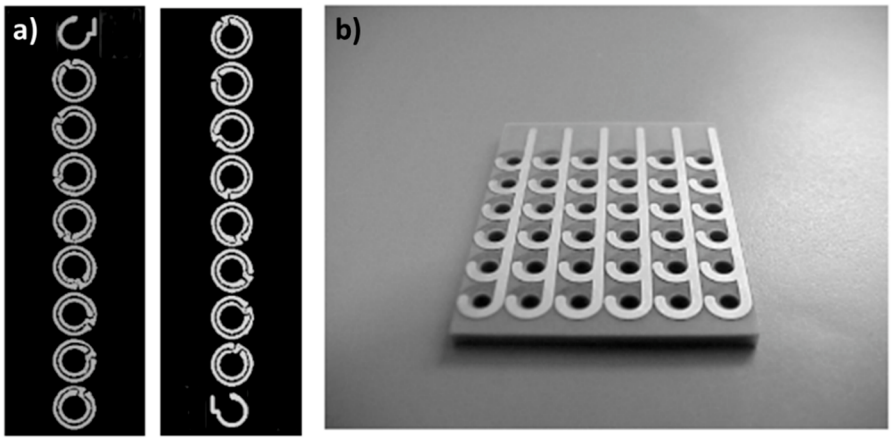



**Figure 1.7:** (a) All 18 layers of copper tracking for a single solenoid, (b) 6x6, 18-layer PCB solenoid [23].

#### 1.2.2.4. Shape Memory Actuators for Braille Devices

Shape memory materials can reversibly change their length/volume upon an external stimulus. Thus, they can be classified as intrinsically active materials. The initial (neutral) volume/length of the material is called the permanent shape whereas secondary shape is attained upon actuation. These secondary/permanent shapes can be restored with very low to no hysteresis. Although there are many types of stimuli such as light, electric field, magnetic field or moisture, the most common stimuli for shape memory materials is heat. Such materials are metal alloys (shape memory alloys, SMA) such as copper-aluminum-nickel, nickel-titanium.

In SMAs shape change occurs due to a phase change from martensite to austenite with the increasing temperature. In these phases, the metal alloys favor different crystal structures resulting in mechanical differences. When a stress is applied to the alloy in its martensite phase the deformation occurs in the form of detwinning which is reversible by heating up to pesudoeleastic austenite phase. It can be said that the shape memory effect is due to the martensite phase while the reversibility of the deformation is due to the austenite phase.

The most frequent form of shape memory alloys in actuators is the coil structure. The SMA is deformed into the coil shape in the martensite phase and thus by heating straightens and exerts force which can be seen in Figure 1.8a.

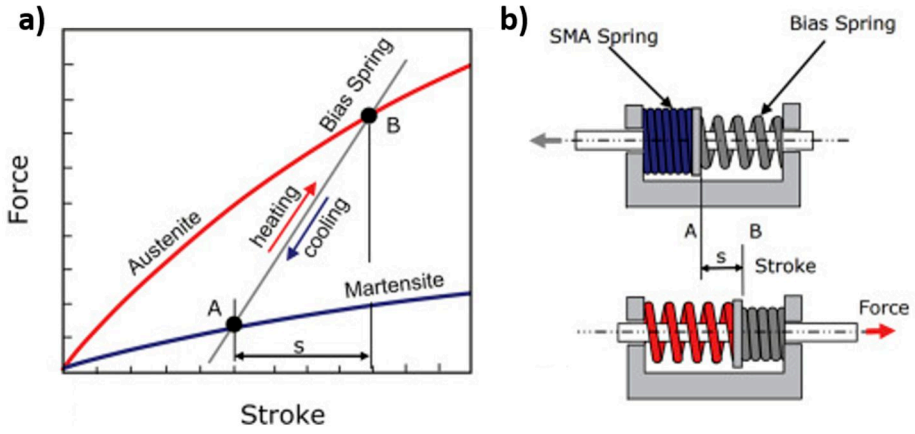



**Figure 1.8:** (a) The characteristic phase diagram and (b) sketch of the SMA coil actuator. The stroke stands for the volume/length change of the SMA coil upon heating/cooling. When the SMA coil extends upon heating, it compresses the bias spring and upon cooling bias coil stretches. Reversible motion is attained by such double coil system [14].

In another study, a tactile display is developed utilizing an SMA based actuators [14]. The working principal of such actuation was based on heating of the SMA upon passage of current through it. As the lower SMA coil unfolded upon heating, the pin elevated and the magnetic material tube is aligned with the permanent magnet. Due to the attraction between magnetic tube and the magnet, the elevated state of the pin is preserved even when no current passes through the SMA. The retraction of the pin is ensured by passing current from the upper coil (Fig. 1.9).

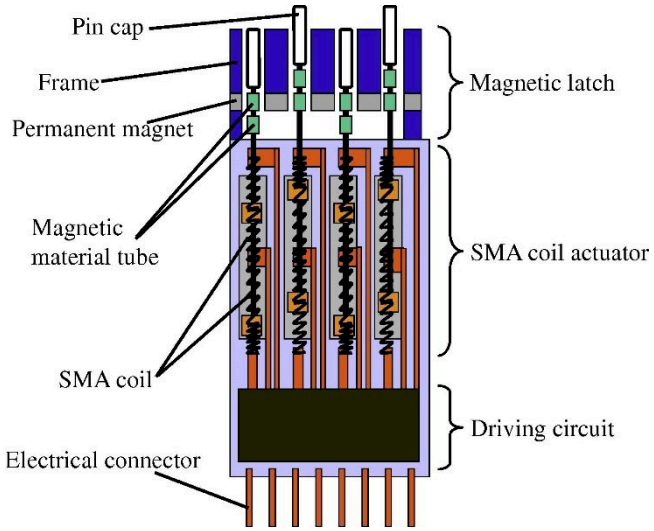



**Figure 1.9**: Schematic of the tactile display utilizing magnetic latch mechanism and SMA coil actuators [14].

## 1.3. Active (Smart) Materials

Previously mentioned actuation systems based on magnetic, shape memory materials or pneumatic systems all depend on complex structures (mechanical parts) to transform produced arbitrary motion into desired actuation. This makes them limited when it comes to development of compact, cost and energy effective Braille devices with smaller actuation systems. Such limitation can only be overcome by utilizing an active material which does not require any complementary system to transform or amplify mechanical response.

For this reason, pizeo-electric active materials have been extensively used in commercial Braille devices. Pizeo-electric materials provide untethered actuation but the produced physical response is in 10-100 μm so an amplification system (cantilever, stepping) is required resulting in bulky structures. So, we need to use other active materials which produce sufficient physical responses to obtain simpler actuation mechanisms.

Active materials have the ability to modify their structure both at molecular and macroscopic scale to give physical responses to environmental stimuli such as light, pH, temperature, magnetic or electric field. Therefore, they are often called smart materials. Such active physical responses can be rephrased as conversion of different types of external energy into mechanical motion which is the base principal of actuation.

As the complexity of the controlled motion increases which requires whole lot more actuators or the size of the overall system decreases, the limitations of down scalability becomes problematic. Thus, soft materials are crucial in filling the gap left by the conventional active materials as the technological progress favors smaller, softer and lighter systems. The key attribute of soft materials in such situation is the extreme adaptability due to the elastic nature overcoming the size and weight limitations.

A classification among soft materials that are widely used in untethered actuator systems in the order of decreasing elastic modulus can be given as conductive polymers, dielectric elastomers, liquid crystalline elastomers and hydrogels.

### 1.3.1. Conductive Polymers

Intrinsic electronic conductivity is obtained in conjugated polymers. In such materials, electrically conductive path is through the molecular backbone of the polymer. Conjugated polymers have linear molecular backbones in which single (sigma) and double (pi) bonds are alternating between adjacent carbon atoms. The delocalization of the electrons in the pi bonds provides a way to transfer electrons along the molecules. However, such phenomena only provide semi-conductivity to the material because the electrons in pi bonds are easier to excite into the conductive band but since the adjacent bonds are stable, electron transfer is still not favored.

Higher conductivity can be achieved through doping. Doping is a mechanism in which an electron is removed or added from/to the atoms in order to create an imbalance in the electronic configuration leading to excitation to an electron transfer between adjacent pi bonds. Thus, the doping agents are either electron deficient species such as Lewis acids which leads to the oxidation (p-Doping) of the polymer or electron rich species such as Lewis bases reducing (n-Doping) the conjugated polymer.

The first example of doping mechanism is the oxidation of the conjugated polyacetylene backbone. Upon doping with a Lewis acid, polyacetylene loses an electron from the pi bond in its backbone which forms a radical cation (polaron). Upon further doping and losing another electron, the radical becomes a bipolaron with even lower band gap. Formation of an electron deficiency causes the electron transfer into it making the structure conductive [24].Doping occurs simultaneously by the oxidants during polymerization process of the conductive polymers such as PEDOT, polypyrrole, etc..

After the discovery of highly conductive polyacetylene by Shikagawa, MacDiarmid and Heeger in 1976, there have been many conjugated conductive polymers developed polypyrrole (PPY), polyaniline (PANI) and poly(3,4-ethylenediocythiophene) (PEDOT) [25]. These materials have been catching a lot of attention in the soft actuator applications due to their conductive and elastic properties.

Acquiring mechanically active materials from such conductive polymers are also possible. When electricity is introduced to the conductive polymer, doping/de-doping occurs. During such phenomena ion exchange between the polymer molecule and either the electrolyte

or dopant molecule is triggered. Such ion exchange results in contraction or expansion of the polymer network.

For example, PEDOT is a widely used polymer for soft actuator purposes either on its own or with its dopant poly(styrene sulfonate) (PSS). PSS is a polymeric p-dopant with relatively big molecular structure. PSS becomes positively charged while PEDOT chains become anionic and affects the shrinking/swelling mechanism during ion exchange due to its large molecular structure. Thus, PEDOT has two types of volume change upon ion exchange mechanism depending on its dopant (Fig. 1.10). When the dopant anion size is small and mobile like p-toluenesulfonic acid (PTSA), upon introduction of negative voltage, the ions are easily expelled from the PEDOT rich region which results in shrinkage at the reduced state (Fig. 1.10a). The process is called anion driven actuation since the migration is anion based. On the other hand, when the dopant anion has large molecules it becomes bonded (ionic bond) on PEDOT during the synthesis process (e.g. PSS). In such case, the cations in the electrolyte migrate to the PEDOT chains to neutralize anions in the reduced state which results in expansion of the polymer. Since the cation migration upon redox reaction is the main reason behind actuation this process is called cation driven actuation [26].

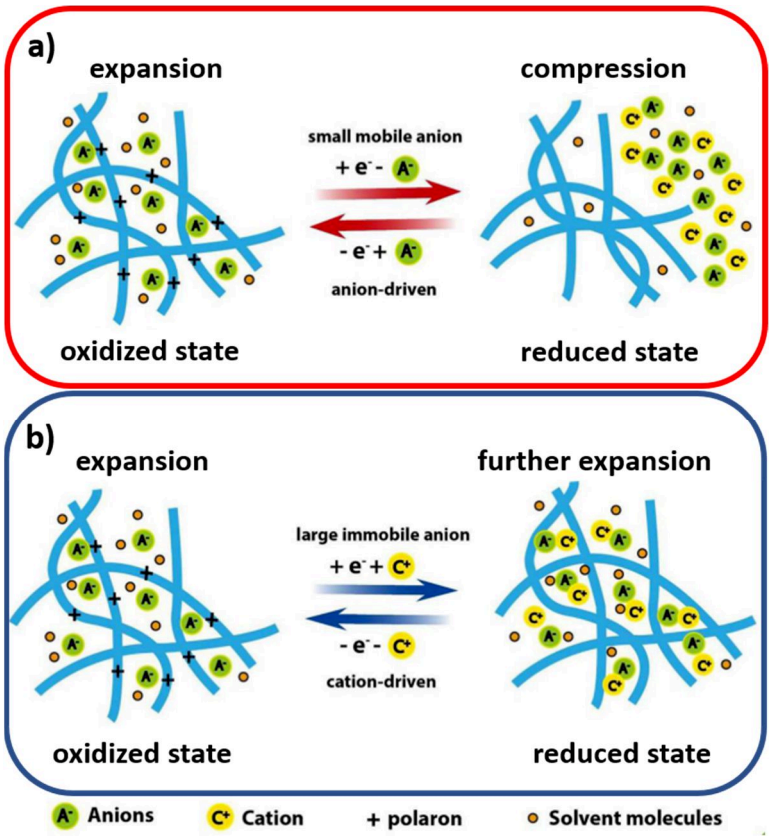



**Figure 1.10:** The ion actuation mechanism of p-doped polymer actuators: a) anion transport dominated when anions are small and mobile (e.g. PEDOT:PTSA), b) cation transport dominated when anion are large and immobile (e.g. PEDOT:PSS) [26].

This property of PEDOT:PSS is widely utilized in soft actuator development since the highly conductive structure require very low voltages (1-3V) for significant actuation strains. The most often used actuator morphology with conducting polymers is the bilayer or trilayer sandwich structure. In such system, a dielectric material ensuring ionic conductivity is sandwiched between two layers (films) of conductive polymer. The two conductive polymer layers are connected to a power supply one to the positive and other to the negative side. As the whole system is ionically in contact with each other, oxidation of the one polymer layer results in reduction of the other upon charge transfer with the ions from the electrolyte which induces a bending motion. Although only a simple bending motion is acquired with such structure, the resulting strain is very significant when the extremely small thickness (1-10 μm) of the polymer layers are considered.

In the study by Simaite et al. (2016), PEDOT:PSS formulations were investigated for inkjet printing of conductive layers. Main drawbacks of PEDOT:PSS was identified to be the poor adhesion to PVDF membranes and unsuitable rheological properties for inkjet printing. Such issues were solved by surface modification of PVDF membranes and using different additives such as glycerol, ethylene glycol, PEG or surfactants such as Triton-X, respectively. A tri-layer structure was developed by adhering PEDOT:PSS layers on PVDF membrane soaked with EmimTFSI ionic liquid (Fig 1.11a). This way, an inkjet printed, PEDOT:PSS based ionic bending actuator was acquired without the need of soaking the whole trilayer structure in electrolyte solution. A bending motion with 0.6 % peak to peak strain was obtained by using ±2 V of potential difference (Fig. 1.11).

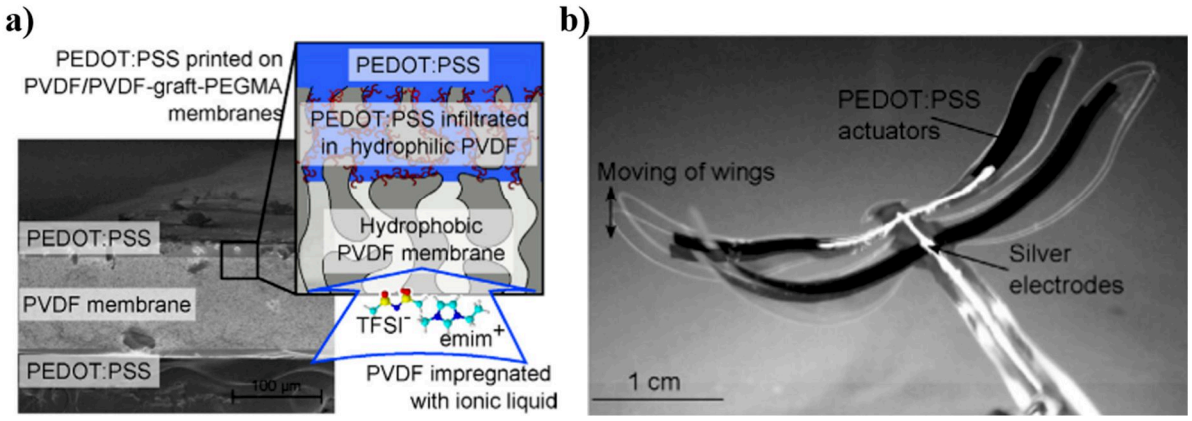



**Figure 1.11:** a) Cross-sectional image of the trilayer PEDOT:PSS/PVDF/PEDOT:PSS structure. b) A dragon-fly shaped inkjet printed PEDOT:PSS actuator and the resulting movement of the wings upon actuation.

### 1.3.2. Dielectric Elastomers (DEAs)

An example of untethered soft actuator is dielectric elastomer actuators (DEAs). DEAs consist of a thin polymer film sandwiched between two compliant electrodes. The electromechanical actuation occurs upon a voltage difference between these two electrodes which induces an electrostatic pressure on the elastomer (Fig. 1.12). Under high voltages (1-5 kV) elastomer is compressed while elongating in two other directions. Therefore, DEA is considered as a 2-D active material.

The optimum material parameters for a good DEA performance are high dielectric constant, low elastic modulus and high electrical breakdown strength. An electrical breakdown occurs when an electrically insulating material is subjected to a high potential difference up to

a point where it starts to conduct electricity. Thus, higher electrical breakdown strength permits operation under higher electrical forces generating bigger actuation strain and force. The most common dielectric elastomers are acrylic elastomers, polyurethanes and silicone elastomers [27,28].

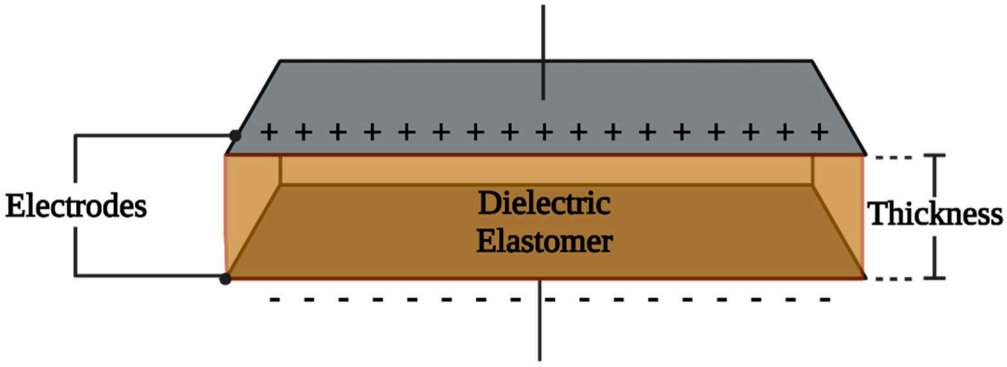



**Figure 1.12:** Illustration of a DEA system.

A good example of DEA is produced by utilizing UV-curable acrylic elastomers as the dielectric material. A multi-stack DEA is developed by having carbon nanotube (CNT) mats in between elastomeric layers as electrodes (Fig. 1.13). CNT electrodes were able to sustain very high applied electric fields (100 V/µm) without suffering from dielectric breakdown. This way, many dielectric layers could be stacked on each other so the amplitude of actuation and amount of force generated is amplified. They were able to produce an artificial muscle system with power density of 18 J/kg which is very similar to actual human muscles (0.4540 J/kg) [29].

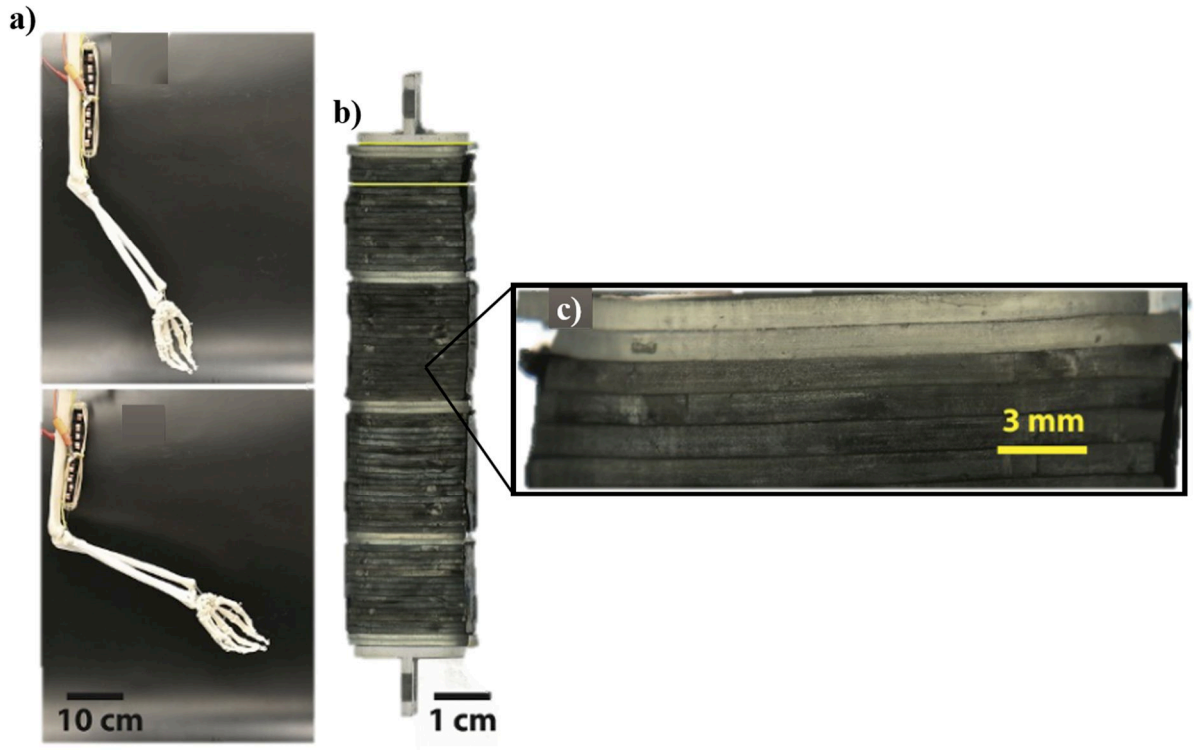



**Figure 1.13:** a) Images showing the contraction of the arm with the help of the DEA. b) Multiple stack of DEAs. The dark gray ones are active layers while light colors are the passive layers. Metallic supports are placed in between to support the system. c) Zoomed in image of the DEA stacks. Each layers consists of 25 individual elastomers with approximately 30µm thicknesses [29].

### 1.3.3. Shape Memory Polymers (SMPs)

Another active polymeric material is shape memory polymers. SMPs can undergo reversible or irreversible shape changes when exposed to external stimuli such as temperature, light or magnetic field. As in SMAs the shape of the SMP can be control between the secondary and permanent shapes with these stimuli. The secondary shape is preserved by the crosslinks in the polymer structure which are also called as net points. These net points can be either chemical or physical crosslinks making SMPs either a thermoset or thermoplastic, respectively. The freely moving molecules on the other hand are called switches and provide the shape-shifting ability to SMPs.

Temperature is the most commonly used stimuli in SMP actuators. Temperature sensitive SMPs can undergo shape change when the temperature is increased over the transition temperature ($T_{trans}$) at which the soft segment (switches) enables alteration of the shape. There are many parameters such as molecular weight, monomer type, crosslinking or degree of polymerization that affects the $T_{trans}$ and enables easier manipulation of the shape memory properties.

In thermoplastic or thermoset SMPs, shape memory effect (SME) consists of three main stages. The first stage is the programming stage in which the temperature is increased over the $T_{trans}$ of the soft segment (switches) and a temporary shape is given. Afterwards, the temporary stage the secondary (temporary) shape is fixed by reducing the temperature below the $T_{trans}$ of the soft segment of the polymer. Finally, the permanent shape is recovered by increasing the temperature over $T_{trans}$ of the soft segment under no external constrained on the material. The permanent shape is preserved thanks to the hard segment (net points) in the structure (Fig. 1.14).

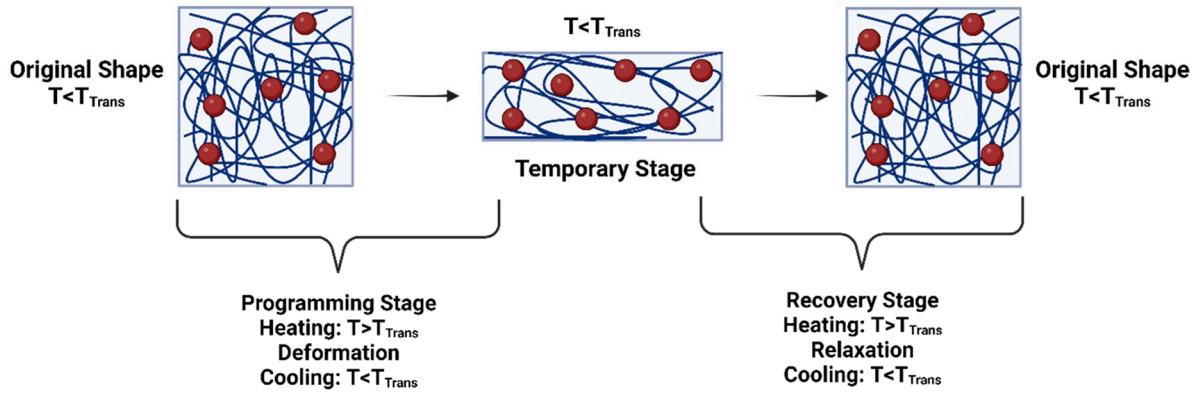



**Figure 1.14:** The stages of thermally induced shape memory effect. Ttrans is the thermal transition temperature of the switching (soft) phase.

SMP actuators were used in developing a swimming robot. Shape memory property of a 3D printed polymer (VeroWhitePlus) with a glass transition temperature ($T_g$) of 60°C (Fig. 1.15) was used for required actuation. SMP was 3D printed in the shape of a beam and deformed into its programmed shape after heating over its $T_g$. The main drawback of shape memory actuation is the slow activation speed. Thus, the actuation stroke is amplified by using bimorph structures attached directly to the shape memory polymer (SMP). The movement of the fins attached to these bimorph fins are programmable by adjusting the SMP beam thickness resulting in different stroke speeds and changing the water temperature. It is known that for the

motion to start, the force generated by the SMP muscle should overcome the energy barrier of the bistable part. Additionally, the actuation speed and the resulting force are directly related to the SMP beam thickness. It was observed that the distance traveled by the robot was related more on the geometry of the bistable structure than the force produced by the SMP muscle [30]. This example shows how SMPs can be utilized for acquiring such complex movements with a simple movement generated by such a light system.

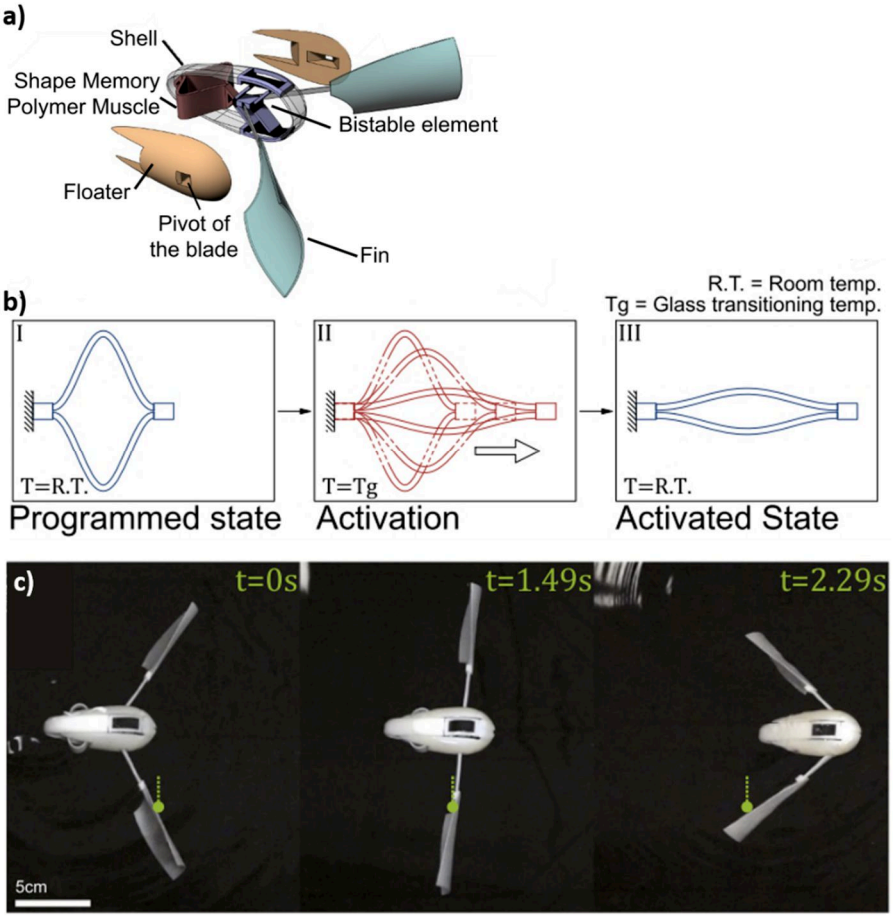



**Figure 1.15:** a) Schematic of the parts of 3D printed swimming robot. b) The SMP muscle in its deployed (I), transitioning (II) and activated (III) phases. c) Images of the soft robot swimming with frontal strokes [30].

### 1.3.4. Liquid Crystalline Elastomers

Liquid crystal elastomers (LCEs) are solid active materials with molecular design and working principal based on well-known liquid crystals. Liquid crystal is a class of material that demonstrates both high intermolecular ordering as in solids while retaining the fluidity of liquids. Typical liquids are comprised of randomly oriented molecules while liquid crystals

possess a degree of long-range order. Thus, they possess anisotropic optical, electrical, magnetic and mechanical properties.

Liquid crystals are comprised of rigid rod or disc-like shaped building blocks called mesogens. These building blocks have affinity for self-organization which is the reason for having crystallinity. Their unique properties such as having anisotropic shape, rigid core, flexible ends and strong dipoles support easy ordering.

Depending on the alignment level of the mesogenic units, LCs have different phases as in Figure 1.16. These phases are called smectic and nematic which can be distinguished by the difference in their level of order. In smectic phase molecules are aligned towards the same direction and ordered layer by layer. In nematic phase although the mesogens are aligned towards the same direction, there is no layered lateral ordering [31]. The temperature at which this change from anisotropic to isotropic phase occurs is called transition temperature. Such temperature sensitive materials are called thermotropic LCEs.

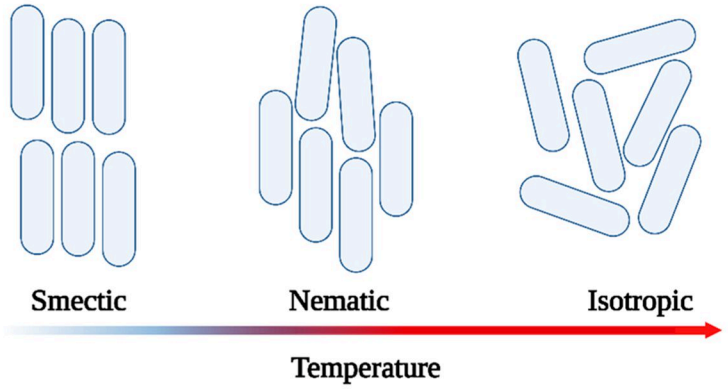



**Figure 1.16:** Different alignment characteristics of mesogens in liquid crystalline phase of thermotropic LCEs with increasing temperature.

In LCEs, mesogenic units are attached to the molecules of the polymeric network. This way, both the elasticity of polymers and smart properties of liquid crystals are combined. The mesogen groups can be position in various way into the polymer backbone (Fig. 1.17). When mesogens are attached to the linear backbone as side chains they are called side-chain elastomer. When mesogens are directly linked in the backbone they are called main chain elastomers.

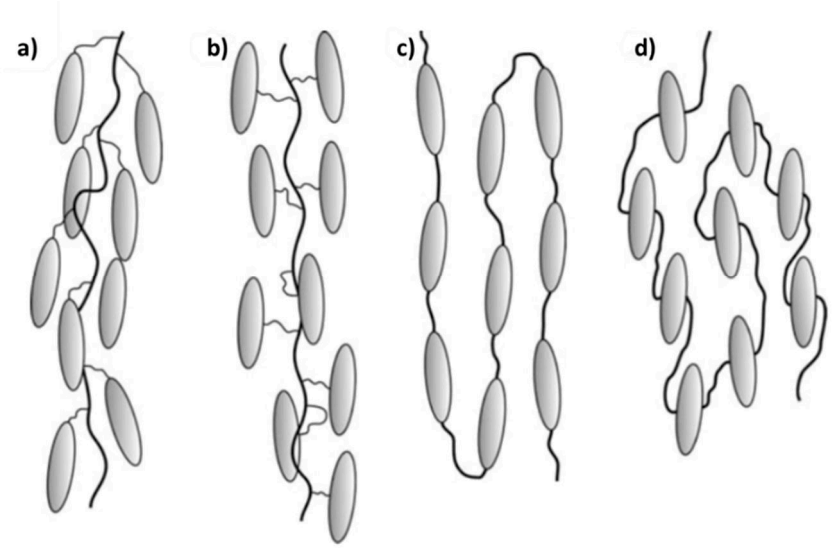



**Figure 1.17:** Different attachment of mesogens on the polymer backbone for the synthesis of LCEs. Side chain elastomer with a) end-on, b) side-on attached meseogens. Main chain elastomers with c) end-on and d) side-on attached mesogenic units [31].

Actuators utilizing LCEs depend on the phase change from nematic to isotropic state to generate mechanical response. The mechanical response in LCE actuators are due to the two main coupling effects. First coupling is between the main elastomeric chain and the mesogenic unit (through bond). Second effect is the coupling between the neighboring anisotropic mesogenic units (steric effect) [31]. The amount of elongation depends on the mesogen arrangement and type (nematic or smectic).

The phase change temperature from nematic to isotropic state ($T_{ni}$) depends on several parameters such flexibility of the polymer backbone, orientation and positioning of the mesogens with respect to the polymer backbone. Stiff and symmetric mesogens result in higher $T_{ni}$ while flexible polymer backbones lower the phase change temperature. Also, mixing different mesogen types can lower the transition temperature [31].

LCE is activated by heating/cooling the material. Swift control of the temperature can be complex. Thus, several methods have been developed to accelerate heat transfer. For example, a fluidic channel system is developed inside the LCE. This way water was flown through the LCE matrix accelerating heat transfer (Fig. 1.18). 15% strain (contraction) was achieved in 2.5s upon passing water 70°C while 30% strain could be achieved in 4s when water temperature was at 90°C. Moreover, a recovery rate of 10%/s was observed when RT water

was passed through the channels. Maximum displacement of 1 cm and maximum force of 0.4 N could be obtained when heated with hot water (90°C) [32].

Several modifications of LCE have been considered to simplify/accelerate the heating process. First approach is introducing conductivity to the LCE with additives such as carbon black [33]. This way, the material could be heated by running electricity through conductive matrix. Nevertheless, we observe delamination and loss of conductive pathways after several actuation cycles.

Modified LCE can also be heated with infrared and visible light by incorporating strong light absorbents such as single-walled carbon nanotubes [34]. This way, the system temperature could be increased by irradiation with light without any undesired sensitivity to physical deformations.

Magnetic field can also be used to indirectly heat LCEs. By introducing ferromagnetic particles such as iron oxide, heat is produced with changing the direction of magnetic field at high frequency imposing vibration [34,35]. This way a contactless trigger mechanism for actuation is ensured.

Finally, UV-sensitive LCE actuators can also be developed by having cis-trans isomerizable groups on the mesogen units. An example for such photo-switchable compound is azobenzene. Thanks to the photoswitchable property of azo groups, the shape of the mesogenic units can be changed from rod-like to kink-like. Such change results in lowering $T_{LC,i}$. Thus, isotropic phase can be achieved without increasing the temperature [19,62.76,20].

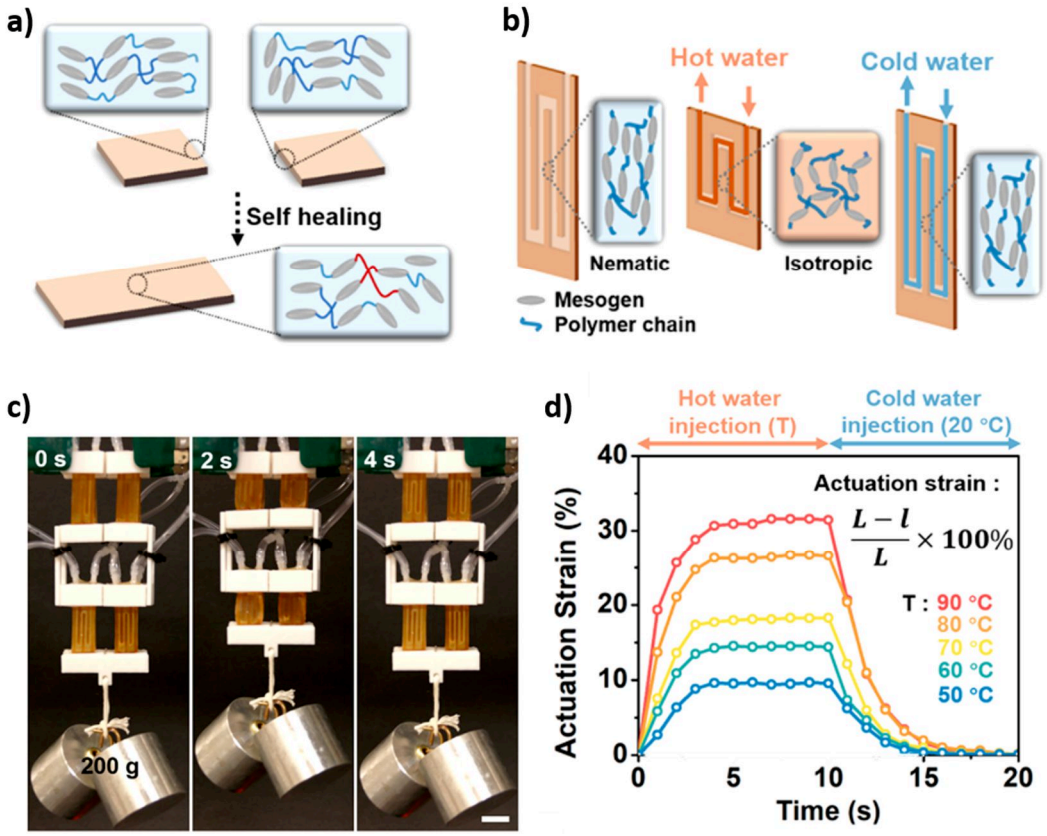



**Figure 1.18:** a) Schematic of the self-healing of the LCE matrix by bond exchange reactions between thiol groups. b) Sandwich structure of the LCE actuator contracting upon passage of hot water due to the nematic to isotropic phase change of the mesogens. c) 8 LCE actuators assembled to achieve ~2cm displacement under 2N (200g) force. d) Graph depicting the actuation strains and rates when water at different temperatures are passed through the channels for 10s followed by cooling with water at RT for 10s [32].

### 1.3.5. Smart Hydrogels

Gel is a crosslinked network of polymeric molecules which has the ability to absorb solvents into the abundant intermolecular spacing. According to the type of solvent, they can be either hydrogels for aqueous solvents and organogels for organic solvents. Up to 90% of the total mass of the resulting system is due to the absorbed solvents. Here we will be focusing on hydrogels as their mechanical properties (elastic moduli between 10 to 1000 kPa) are perfect for mimicking living tissues which enables their application as soft actuators or artificial muscles to be more specific.

Some hydrogel – called Smart hydrogels – can reversibly change their volume by absorbing or releasing solvent. This reversible swelling/shrinking is controlled by various environmental stimuli such as temperature, pH, salinity, solvent composition… The volume change is due to the modifications in solvent affinity of the polymer matrix when the environment is modified. This volume change is often considered for drug delivery. But it is particularly interesting for actuation as the actuation stroke is much larger than for any other active material. A smart gel can change its volume by up to 1000 %.

The major problem before hydrogels as actuators are the swelling/shrinking rate. The solvent diffusion rate is the limiting factor. Thus, hydrogels are mostly used as micro actuators and utilized in the form of thin films (~100 μm thickness). This way the actuation rate is increased by shortening the diffusion path of solvent but the working stroke is limited. Thus, large hydrogel actuators (mm scale) cannot be used for fast actuation and the full potential of hydrogels are not utilized.

The volumetric change in hydrogels is isotropic which limits the control over motion that is generated. More complex movements (actuations) are obtained by producing hydrogels with inhomogeneities showing different swelling amplitudes. Inhomogeneities are produced by various methods such as sequential synthesis, field induced alignment, ionoprinting, photolithography or 3D printing [36]. These methods have enabled extensive control over the actuation modes such as folding, bending, twisting, curling and buckling upon exposure to stimuli. Such motions significantly increase the potential applicability of the hydrogels to various actuation modes such as gripping, crawling, swimming etc.

In sequential synthesis method, several layers of smart hydrogels are printed onto each other. This results in multi-layer structure. Since either the gel material or the additive affecting the modulus of the gel matrix is different in adjoining layers, swelling or shrinking results in anisotropic motions such as bending (Fig. 1.19a).

Field induced anisotropy utilizes alignment of ferromagnetic or conductive materials inside the gel matrix. This way, patterning can be achieved which induces heterogeneity in physical properties and swelling properties (Fig. 1.19b).

Photolithography is a very advantageous method in producing very high precision patterning on the gels. A preformed isotropic gel with a photo-crosslinker is covered with a mask and exposed to light. This way the regions which are exposed to light have higher crosslinking density thus higher elastic modulus (Fig. 1.19d).

3D printing is an additive manufacturing method. Precise and complex single or multi-material structures can be produced. There are two distinct 3D printing methods called stereo lithography and extrusion. In stereo-lithography method, a laser beam is very precisely controlled to crosslink the polymer layer by layer according to a predefined structure. The precision is much higher than the extrusion method. In extrusion method, polymer in molten or dissolved state is extruded on a surface layer by layer. The extruded polymer is either hardened upon cooling or dried on the surface after extrusion to preserve its shape (Fig. 1.19e).

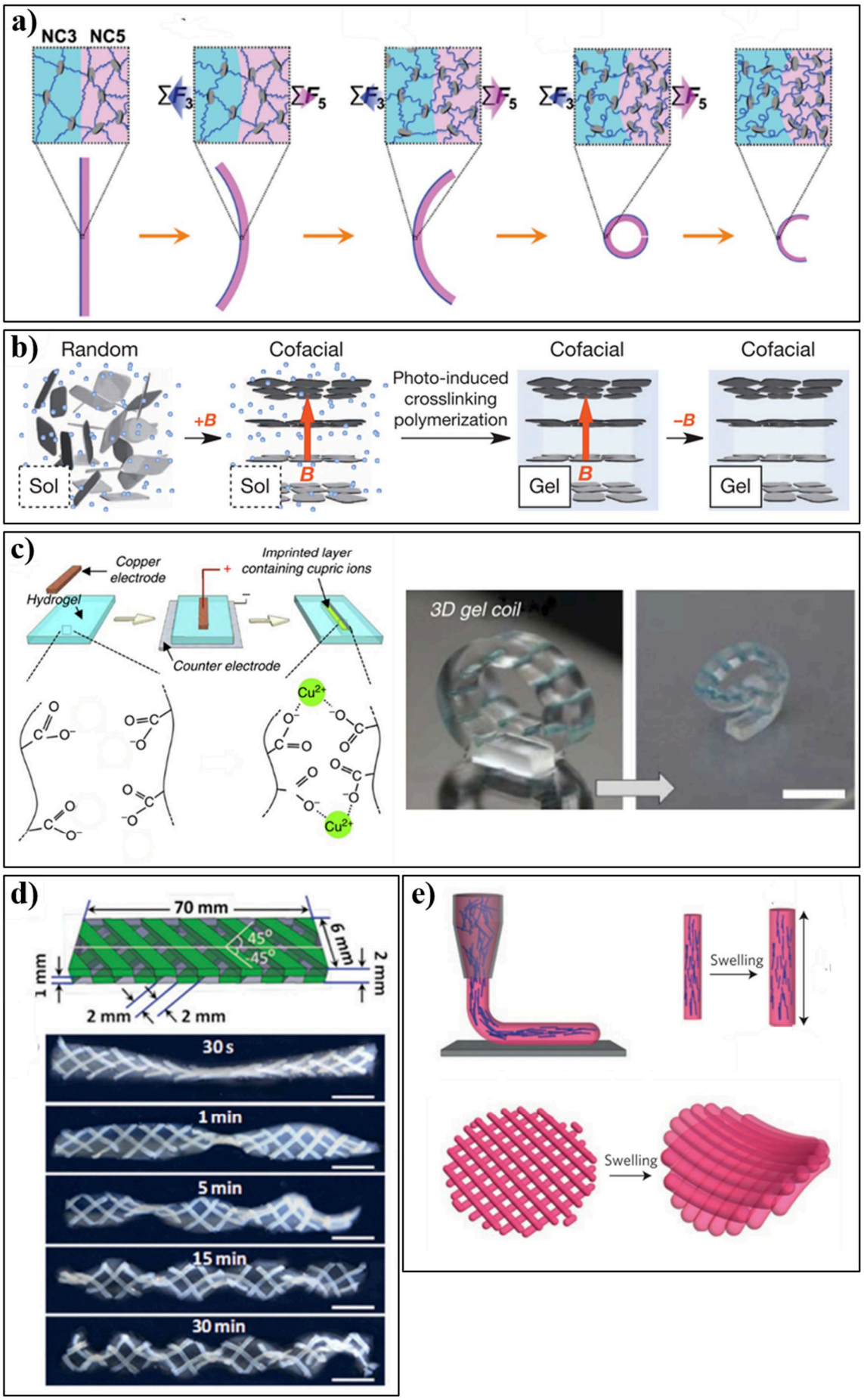

a)
NC3 NC5
$\sum F_3$
$\sum F_5$
b)
Random
Cofacial
Cofacial
Cofacial
+B
B
Sol
Sol
Photo-induced
crosslinking
polymerization
Gel
B
–B
Gel
c)
Copper
electrode
Hydrogel
Imprinted layer
containing cupric ions
Counter electrode
$Cu^{2+}$
$Cu^{2+}$
3D gel coil
d)
70 mm
45°
45°
6 mm
2 mm
1 mm
2 mm
2 mm
30 s
1 min
5 min
15 min
30 min
e)
Swelling
Swelling

**Figure 1.19:** Examples of different methods for providing anisotropic actuation motion to smart hydrogels. a) Sequential synthesis method. Bilayer PNIPAM/Clay nanocomposite (NC) gel The bending motion induced upon heating over volume phase transition temperature (VPTT) [37]. b) Field induced anisotropy method. Titanate nanoscale (TiNS) particles were aligned in the aqueous NIPAM monomer solution by strong magnetic fields before UV initiated polymerization. The thermally triggered volume change of PNIPAM was more prominent in the direction perpendicular to the TiNS layers converting isotropic swelling to bending motion [38]. c) Ionoprinitng on PNaAc gel inducing metal complexation in gel matrix. Ionoprinted gel actuating in coiling mode upon shrinking. Scale bar, 5 mm [39]. d) Schematic of the IPN PNIPAM/PAAc double layer structure. Green zones are PNIPAM gel whereas transparent zones represent PAAc gel and images of the resulting buckling when the pH is increased from 1 to 9. Scale bar is 1 cm [40]. e) Extrusion of the PNIPAM/clay solution containing cellulose nanofibrils through a nozzle with 200 μm internal diameter. The printed grid structure and resulting bending motion upon heating due to the anisotropy generated by the aligned nanofibrils [41].

Anisotropic volume change is achieved in these gels which enables more complex actuations but all these actuators operate in aqueous environment. In other words, the actuation is mostly depending on dipping the gels into different solvents. Thus, most of the time there is no real control over the actuation. For real untethered systems, stimuli enabling more precise control over the actuation are required such as temperature and chemical reagents.

There are also stimuli such as magnetic field [42–44], electricity [45,46], or light [47,48]. But these stimuli are not aiming directly the gel but the additives in the gel matrix. Their secondary effect on the gel either by heat dissipation (photo-thermal effect, joule heating, etc.), chemical changes or stress generation induces actuation. On the other hand, stimuli such as temperature and chemical changes are generating actuation due to the intrinsic properties of temperature sensitive and chemically sensitive gels, respectively. Thus, thermo-responsive poly(N-isopropylacrylamide) (PNIPAM) and pH-responsive poly(acrylic acid) (PAAc) gels constitute majority of the studies on hydrogel based actuators.

## 1.4. Compliance of Smart Hydrogels for Untethered Actuation

In this study, we aimed to obtain a small, simple, fast and efficient actuation system to be used in Braille devices and artificial muscle applications. Such applications not only require compact designs but also fast actuation (<1 min). Thus, we need intrinsically active materials for untethered actuations. Smart gels fulfill all of the requirements above as they are elastic, soft materials that can generate high actuation ratios (~1000%) upon many types of stimuli. These stimuli should enable precise and swift control over the actuation. Here, we will report different types of smart hydrogels in terms of respective stimulation mechanisms.

### 1.4.1. Smart Gels Sensitive to Different Stimuli

#### 1.4.1.1. Temperature Sensitive Actuation

Some gels are sensitive to changes in temperature thus can shrink/swell upon heating/cooling. These smart gels are particularly interesting since adjusting temperature is relatively simple enabling good control over actuation.

In temperature sensitive gels, we observe a sharp change of volume at critical temperatures. This is due to the change in solubility of the monomers constituting the gel. This temperature is either called lower or higher critical solution temperature depending on the phase separation occurring below or over the critical temperature, respectively. These gels are also named as positively thermosensitive (shrinking over LCST) or negatively thermosensitive (swell over UCST) (Fig. 1.20).

The majority of the polymers in the literature are positively sensitive and poly(n-isopropylacrlamide) (PNIPAM) is by far the most studied thermosensitive polymer. Its temperature responsşve properties were first reported in 1960's [49]. It attracted increasing attention due to its high potential in many areas such as drug delivery systems [50–53], dosimeters [54,55], enzyme immobilization systems [56,57] and mechanical actuators [43,58–60]. Moreover, LCST of PNIPAM can be adjusted by adding co-monomers such as methacrylate (19-36 °C), acrylamide (35-100 °C), 4 pentonic acid (19-36 °C), vinyl laurate (<19 °C) etc. [61].

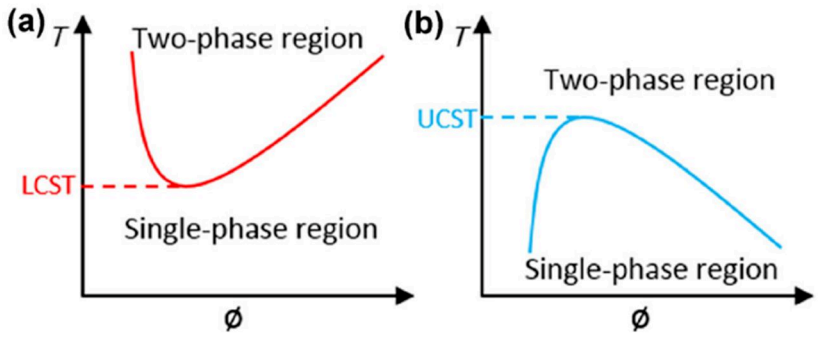



**Figure 1.20:** Temperature vs polymer volume fraction graphs as phase diagrams of polymer solution with a) LCST and b) UCST behavior [49].

Such phase transition happens because NIPAM has both hydrophilic amide and hydrophobic propyl groups in its molecular backbone. The affinity between these reagents are highly affected by temperature change. Below 34°C (LCST of NIPAM), the amide groups become highly hydrated resulting in repulsion of the propyl groups from each other. This causes the overall polymer matrix to become hydrophilic and swell. Upon heating over LCST, the vice versa occurs and the matrix repels water resulting in shrinking. Such change in intermolecular attractions result in reversible transformation of the molecular entanglements from random coil (hydrophilic) to globular (hydrophobic) upon heating. This results in significant volume change ratio (3D actuation) capabilities.

However, there is a factor limiting the volume change rate of PNIPAM hydrogel which is called skin-effect. During heating over LCST, molecules on the surface of the gel becomes hydrophobic faster than the inner matrix. Thus, diffusion rate of water from the gel is limited by the hydrophobic skin formed at the surface. Such limitation can be eliminated by shortening the average diffusion path of water inside the gel with pores. The gel itself is highly porous but the pores are all in the scale of 1-100 nm. Such small pores highly contribute to the absorption capability of the gel but they are not big enough to overcome the diffusion limitation and skin effect. Macropores (diameter >75 μm) are required to overcome such capillary limitations.

Moreover, soft nature of the PNIPAM gel (E=<10 kPa) limits the amount of actuation force that can be generated upon swelling (<1.0 g) [62,63]. For this reason, toughening mechanisms are utilized such as introduction of additives [62,64] or another gel (double network gels) [58,65]. Unfortunately, such toughening mechanisms decrease the actuation rate and ratio while increasing the mechanical properties. This is because they act as physical barriers either to diffusion or the rigid elements restricting volume changes.

#### 1.4.1.2. pH Sensitive Actuation

pH-sensitive gels can swell and shrink reversibly as function of the pH. This property derives from the presence of acid-base reactive pendant groups which acquire charges through the exchange of proton when the solution pH is modified. These groups can ionize upon being exposed to aqueous solutions with appropriate pH. When the polymer gets charged, it becomes much more hydrophilic and the gel swells. The amplitude of swelling can reach up to 1000% and depends on the monomer concentration and on the gel elastic modulus [66].

The pH response of the gel depends on the type of monomer. For instance, triggered volume change behavior is categorized according to the nature of the ionizable pendant groups in the molecules. Proton acceptor hydrogels are ionized at pH greater than their acidic dissociation constant (pKa) which results in swelling behavior due to the osmotic pressure generated. The most common examples to anionic ionizable monomers are aryclic acid (AAc) and methacylic acid (MAAc) [67,68].

Other main group of pH sensitive gels are proton donor hydrogels. These hydrogels contain proton accepting pendant groups which ionize at pH levels lower than their pKa resulting in swelling behavior. Important monomers with cationic pendant groups are dimethylamineoethyl methacrylate (DMAEMA) and diethylaminoethyl methacrylate (DEAEMA) [67].

There are also some examples to natural polymers such as albumin, gelatin, alginate and chitosan which show sensitivity to pH. Protein based polymers such as albumin and gelatin tend to form helices which acts as physical crosslinks in their gel matrix. Such crosslinks can be stabilized upon hydrogen bonding at certain pH and temperature conditions resulting in swelling behavior. For the polysaccharides such as chitosan and alginate, physical crosslinks can be generated through hydrophobic or charge interactions again at certain pH conditions [67].

#### 1.4.1.3. Chemically Sensitive Actuation

Another type of smart hydrogel is chemically sensitive gels. In the presence of the target molecules, these gels either form complexes or induce changes in pH, temperature or electrical charges in their environment to show volumetric changes. Gel molecules basically become hydrophobic upon complexation or environmental changes and thus shrink. Such property is widely used in areas such as drug release as chemical recognition capability becomes highly advantageous.

Main sub-groups of chemically sensitive gels are glucose sensitive, enzyme responsive or molecularly imprinted gels. The common property for all these types of gels is the capability of showing volumetric change upon exposure to specific chemicals that form complexes with the gels molecular backbone.

Hydrogels with glucose sensitive reagents are glucose-oxidase gels, caoncavalin A gels and phenylboronic acid gels according to their glucose detection/response mechanisms. While concavalin A and phenylboronic acid gels form complexes with glucose to induce volume change, glucose oxidase gel undergoes volume change upon shift in pH with oxidation of glucose [67].

Enzyme responsive gels generally consist of peptide chains either as pendant group linkers or chemical crosslinks which can be removed (cleaved) in the presence of specific enzymes. When these peptide groups link pendant groups, they are generally utilized to trigger drug release upon exposure to certain enzymes. More importantly, when these peptide chains are utilized as chemical crosslinks, swelling can be irreversibly triggered upon degradation by enzymes [67].

Last and the most widely studied group of chemically sensitive gels is the molecularly imprinted gels. These gels are made to complex with specific chemical reagents. The monomers of the hydrogel are functionalized with the target molecules before polymerization. This way, monomers are made to recognize and complex with target molecules. Then, target molecules are removed from the monomers before polymerization into a hydrogel. As a result, hydrogel has the ability to recognize the target molecules and form complexes upon second exposure [67].

#### 1.4.1.4. PAAc Gel Sensitive to Metallic Ions

Poly(acrylic acid) (PAAc). PAAc is a linear polymer produced by radical polymerization of acrylic acid monomers which contains a large number of carboxyl groups. Since carboxyl groups are highly sensitive to both ionic strength and pH, the equilibrium swelling ratio of the PAAc hydrogels are dependent on both parameters. PAAc was reported to show a phase change upon introduction of Cu(II) ions into the solution. These cations form a complex with the carboxyl groups in the molecular backbone and bridging the chains. This results in shrinking of the PAAc hydrogel matrix (Fig. 1.21).

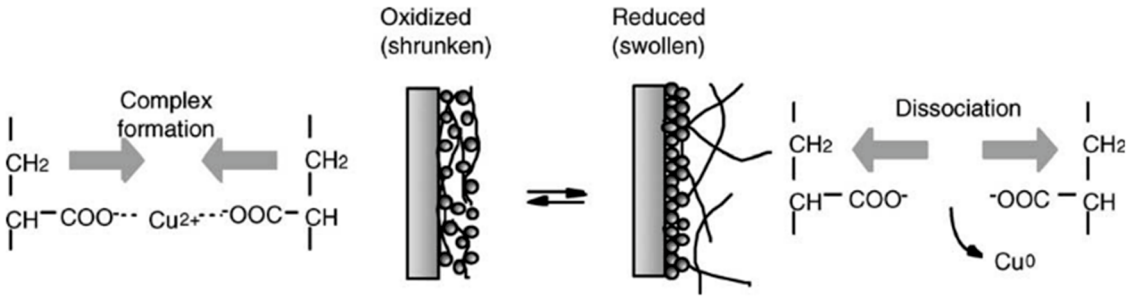



**Figure 1.21:** Mechanism of the volume change of PAA hydrogel upon redox reaction of copper [69].

Such sensitivity of PAAc gel to metallic ions and the ability to show distinct volume changes provides great potentials in artificial muscle applications. With the introduction of electrically controlled trigger mechanism on the reversible complexation with copper ions, PAAc hydrogel can be utilized as a redox actuator [70,71]. The actuation rate/ratio can even be enhanced by introduction of electronic conductivity to the PAAc gel. This would result in higher charge densities on the gel upon applying voltage and thus, more ion transfer.

There are also other gels which contain carboxyl or catechol groups that can form reversible complexes and additional crosslinking with cationic metal ions in their molecular backbones. This property can be used to induce patterning since increased crosslinking density results in increase in hydrophilicity and elastic modulus. Such local changes in mechanical properties induces anisotropic stress distribution which results in oriented deformation of the gel. Palleau and Morales (2013) were able to induce ionoprinting on sodium polyacrylate (PNaAc) gel which is a chemically sensitive hydrogel. A copper anode was brought in contact with the gel and $Cu^{2+}$ ions were complexed with the carboxylic groups of the gel upon oxidation increasing the modulus locally (Fig. 1.20c). Moreover, when subjected to EDTA, the cupric

ions were removed from the gel molecules making the process reversible. By changing the solvent from water to ethanol, the patterned gel was shrunk producing predetermined motion [39].

#### 1.4.1.5. Other Light Sensitive Gel

Light is also utilized as direct or indirect stimuli to trigger volume change on smart hydrogels. It is considered to be highly advantageous since it allows contactless stimulation of the gel. The downside of light stimulation is the limitation in penetration (light transmittance) through opaque surfaces.

In light sensitive actuation, photo-initiated reactions are utilized to either adjust the cis-trans isomerization of the gel molecules. This way, the polarization and the hydrophilicity of the molecules can be changed which leads to either direct volume change or pH sensitivity. Azobenzenes or spirobenzopyran can be given as an example to reagents which can be used either as UV sensitive monomer or crosslinker in hydrogels [72,73].

#### 1.4.1.6. Indirect Heating for Hydrogel Actuation

There are also gels developed which can be actuated by stimulation through introduced light, magnetic field or electricity. Majority of these gels depend on indirect generation of heat of chemical reagents. Here, we will briefly discuss such stimulation methods.

For the secondary heating effect, stimuli (light, magnetic field, electric field) are generally utilized to induce actuation upon temperature change by photo-thermal effect [74,75], vibration or joule heating [76], respectively. In order to utilize light to trigger actuation, additives such as chromophores [77] , carbon nanotubes [60], graphene oxide [78] are introduced to the gel matrix to increase the light absorptivity and induce heat generation by radiation. Magnetic field sensitive gels contain additives with magnetic properties. Such magnetic particles in the gel matrix either amplify the swelling/shrinking upon thermal/chemical triggers (induce heat generation when exposed to high frequency fluctuating magnetic field) or provide anisotropic mechanical properties under magnetic field [42–44,53]. Lastly, conductive additives such as metal or carbon-based particles are added to gels to induce a level of conductivity (semi-conductivity). Upon passage of electrical current through the gel, it acts as a resistor and heats up [79,80].

## 1.5. Response Dynamics of Hydrogels

Hydrogels are very advantageous materials to be utilized as actuators due to their soft, elastic and smart properties. The physical response to the aforementioned stimuli is in the form of isotropic volume (3D) change. This makes hydrogels very efficient actuators since their volume can change up to 10x their initial size. As a result, high actuation strokes are acquired from small actuator systems. This way no external system or excess material is required to amplify the actuation stroke. Moreover, their elastic nature and polymeric structure enables easy, cheap production in any size to with easy handling. All these properties make hydrogels good candidate for compact and simple actuators in

On the other hand, the biggest drawback is the slow response limiting the potential applications. Main reason behind such slow response is the limited diffusion rate (diffusion coefficient of $10^{-11}$-$10^{-10}$ $m^2.s^{-1}$) of solvents inside the micro/mesoporous gel matrix which is crucial for volumetric changes [71].

Here we will focus on the poroelastic swelling kinetics of hydrogels. Volume change rate of gel is diffusion limited. Thus, we will investigate the flow characteristics such as permeability of gels diffusion coefficient of water in the gel matrix. Moreover, we will investigate the effect of macroporosity on the swelling kinetics of hydrogels.

In order to overcome such limitation, macroporosity is introduced into the gel matrix. Porous structure not only permits faster diffusion but also increases the toughness of the hydrogel [71]. Moreover, in order to better understand the poroelastic behavior of the gel structure, studies such as Biot's theory and Tanaka, Hocker, Benedek theory are developed. In the next section, we will be discussing such linear theories of poroelastic swelling to better understand the phenomena.

### 1.5.1. Poroelastic Swelling of Hydrogels

Gels are polymer networks that can imbibe great amounts of solvent. While having elastic solid properties due to the crosslinked polymer network, mobility of solvent molecules is possible in the micro/mesoporous matrix. Due to such unique properties, the gel deformation mechanics have been studied under a unique area of poroelasticity.

Mesoporous hydrogel matrix consists of pores with 10-100 μm diameters. Thus, gels act as porous media and show unique poroelastic properties. Despite the porous structure, water diffusion through gels is very slow due to the small sizes of the pores compared to the gel matrix. With increasing overall gel volume, diffusion limiting effect of gel matrix amplifies. Gel samples of 1.0 cm size take from hours to days to swell or shrink [63]. Due to such porous structure, water diffusion also follows a unique poroelastic behavior which can be partly described by linear theories.

Biot's theory (1941) is the first comprehensive linear theory to explain the solvent transfer upon mechanical deformation of porous media. It was originally developed to describe the migration of liquids in soils under compressive stresses which results in settlement of the porous media (soil consolidation). In this theory, the porous media and the solvent imbibed are taken into account as a single body in which pore pressure is a state variable [81].

In the Biot's theory of linear elasticity, the gel is initially taken to be homogeneous without any stress applied. The main variables to be taken in to account are the solvent concentration and chemical potential of the solvent inside the gel. The driving force for the solvent migration during any deformation is attributed to the difference in chemical potential between the solvent inside and outside the gel matrix. Moreover, the whole system is thermodynamically in equilibrium meaning that the change in free energy is due to the work done by stress and migration of solvent. Assuming both the polymer and solvent molecules are incompressible, the volume change is due the change in solvent concentration. This allows to obtain a direct relation between the applied stress, strain and difference in chemical potential of the solvents inside and outside the gel. Such relation shows the important role of elastic modulus and Poisson's ratio in explaining the poroelastic behavior of hydrogels under stress (Eq. 1.1),

$$\sigma_{ij} = 2G\left(\varepsilon_{ij} + \frac{\nu}{1-2\nu}\,\varepsilon_{kk}\delta_{ij}\right) - \frac{\mu-\mu_0}{\Omega}\delta_{ij} \tag{1.1}$$

where σ represents the stress, ε strain, ν Poisson's ratio, Ω volume per solvent molecule, μ chemical potential of the solvent and G elastic modulus.

To understand this model, let's look at the strain induced swelling of a hydrogel predicted by Biot's theory. We consider a homogeneous gel cylinder with an initial diameter and length in equilibrium with its surrounding solvent (Fig. 1.22). At the instant of elongation upon pulling from the ends, the gel behaves as an incompressible elastic solid (Poisson's ration

of 0.5) thus the lateral strain is proportional to the 0.5 times the vertical applied strain. According to the relation given above, the vertical applied stress becomes proportional to the elastic modulus of the gel ($\sigma_{zz}=3G\varepsilon$) while there is no lateral stress. Upon the resulting strain, the chemical potential of the solvent inside the gel decreases below the solvent outside the gel. Consequently, gel imbibes more solvent and the gel volume increases relaxing the pulling force. When the new equilibrium is reached, the chemical potential inside the gel becomes equal to the chemical potential outside. The gel behaves like a compressible solid with certain elastic modulus and Poisson's ratio. Thus, the equilibrium volume is directly related to the Poisson's ratio and the elastic modulus of the gel. In other words, Poisson's ratio determines the amount of solvent uptake of a hydrogel in response to applied stress [82].

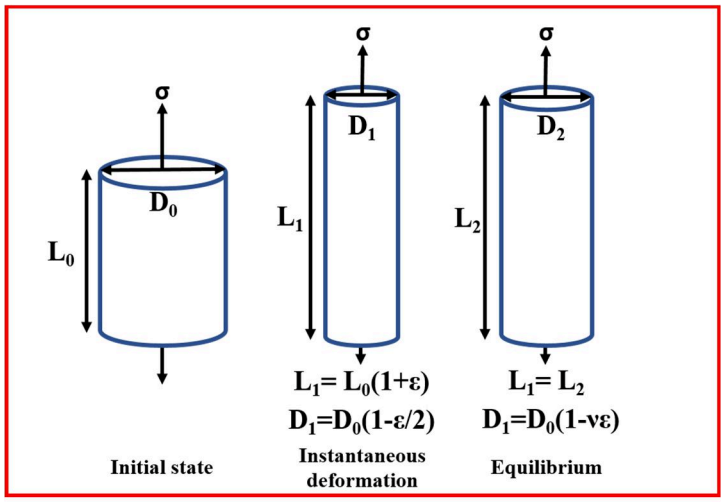



**Figure 1.22:** Schematic of the hypothetical gels swelling induced by elongation [82].

### 1.5.2. Free Swelling of PNIPAM Gel

In order to validate Biot's theory of poroelastic swelling with experimental results, Yoon et al. (2010) observed swelling of a thin (100 μm) layer of PNIPAM gel without any constraints via fluorescence microscopy. Upon immersing the gel into a solvent with certain chemical potential, the gel freely swells and after enough time equilibrates with the external solvent. Since there is no constraint, the gel does not experience any stress during swelling. Taking these conditions into account, we obtain the thickness at equilibrium which is directly related to Poisson's ratio, difference in chemical potential and initial thickness of the gel while being inversely related to the elastic modulus of the gel. During the transient condition, in which swelling continuous to occur, chemical potential of the solvent inside the gel, gel

thickness and in plane strains are all time dependent variables. The in-plane swelling is equal to the vertical swelling since there is no constraint and thus, the shape of the gel remains the same. Considering these parameters, a kinetic partial differential equation explains the free swelling of the gel. During the free swelling of a gel layer, in plane deformation cannot be neglected which is always equal to lateral deformation making numerical solution not possible. Thus, Yoon and coworkers incorporated experimental data to obtain an analytical solution. On the other hand, numerical solution was achieved for the constrained swelling where deformation only occurred in the vertical plane. For such case the analytically solvable equation;

$$\frac{\Delta(t)}{\Delta(\infty)} = \frac{2}{H}\sqrt{\frac{Dt}{\pi}} \tag{1.2}$$

was obtained. Where Δ(x) is the change in thickness of the gel, Δ(∞) is the maximum change in thickness at equilibrium, H is the initial gel thickness of the gel, t is the time and D is the diffusion constant of the solvent in the gel. Such equation could be further solved to model the transient part of the swelling process. The comparison of the experimental swelling and analytical solution can be seen in Figure 1.23 [82].

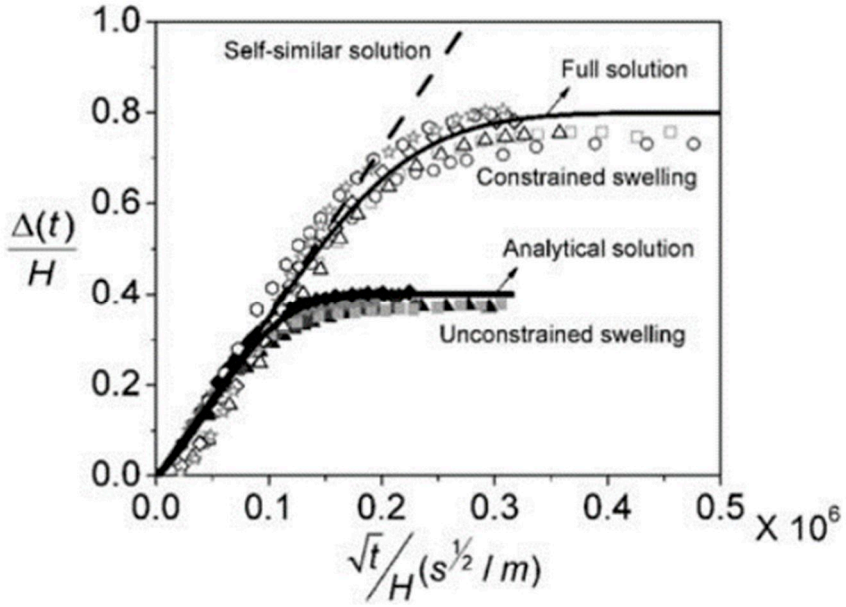



**Figure 1.23:** Comparison of the experimental results and theoretical predictions of both constrained and unconstrained swelling of PNIPAM gel. The diffusion coefficient data was

obtained from the initial slope of the constrained swelling results then used with the equilibrium swelling ratios to plot the analytical solution [82].

### 1.5.3. Macroporous Gel

Smart hydrogels are widely used as actuators. Currently, their utilization as fast actuators are limited due to the slow solvent diffusion in the mesoporous gel matrix during shrinking/re-swelling. To overcome such limitation, best strategy has been reducing the average diffusion path length of solvents inside the gel. Hydrogel actuators have been produced in very thin layers (thickness <10 μm) to obtain fast actuation (~1s) [71]. This in turn, resulted in smaller actuation strokes.

Another way to reduce diffusion path length of solvent is by creating large voids (macro pores) where solvent can freely flow through without experiencing any diffusion limitation. This way not only the actuation is accelerated, the volume change ratio and toughness of the gel is improved.

Many methods were studied too induce macroporosity to hydrogels which are based on templates. These templates are sacrificial meaning they are removed after crosslinking the hydrogel leaving pores. The templates can be made of emulsion [83–85], foam [86,87] or solid [63,88–90] sacrificial materials.

By producing a highly porous hydrogel matrix the actuation rate is increased (< 1 min for mm sized gels) [63]. Moreover, size limitation on the hydrogel actuators are removed. This means the bigger hydrogel actuators can be produced without increasing the average diffusion path length of solvent.

## 1.6. Motivation and Problem Statement

The goal of this thesis is to develop small, fast and efficient actuators for Braille device and artificial muscle applications. For this purpose, smart hydrogels are utilized as they can produce high actuation amplitudes despite their low volume and weight. Main problems before development of better hydrogel actuators was limited control mechanism and slow actuations rates. We utilized thermo-sensitive and electro active gels as active materials since temperature and electrical potential are easily controllable external stimuli for triggering actuation. Moreover, we investigated different methods for introducing macroporousity to the gel matrices to overcome the diffusion limitation on the volume phase change dynamics. We further investigated the effect of different levels of macroporousities on the poroelastic shrinking/re-swelling dynamics.

## 1.7. Thesis Structure

### Chapter 2

In the following chapter, we present both covalently crosslinked and physically crosslinked PNIPAM gels. Firstly, we investigate the effect of intermolecular bonds on the thermo-sensitive shrinking/re-swelling rate/ratio of PNIPAM gels. Then, by introducing two different geometries and levels of porosities the volume phase change rate/ratios are enhanced. It is observed that there is no symmetry in shrinking and re-swelling rates for the bulk gels. This asymmetry is minimized with enabling faster diffusion during both shrinking/re-swelling by introduction of 60% macro porosity in the gel matrix. Moreover, a heating/cooling system is also developed for utilizing macro porous PNIPAM gel actuator in Braille devices. A single pin heating/cooling system is developed and the heating/cooling efficiency is investigated by numerical simulation and experimental methods.

### Chapter 3

In this chapter, we investigate the effect of porosity level on the poroelastic swelling and water permeability of PNIPAM gels We use 3D printed shellac scaffold to have more control on the porosity level of the gel and pore. The water insoluble nature of shellac at low pH allowed us to utilize it with aqueous NIPAM solutions. We dissolve the shellac scaffolds in concentrated NaOH solution to obtain engineered macro porous PNIPAM gels. We observe swelling rate/ratio by imaging and analyzed them to compare the poroelastic swelling kinetics. Finally, we place the porous gels in a pressure controlled microfluidic chamber to determine the effect of geometry and density of pores on water permeability of PNIPAM gels. Finally, we observe the behavior of poroelastic gel under flow induced compression.

### Chapter 4

In the final chapter, we present development of an electroactive PAAc/PEDOT:PSS double network (DN) actuator. First, we investigate three different methods to produce an electrically conductive double network gel using PEDOT:PSS and PAAc. Afterwards, we characterize the electrochemical properties of the acquired DN gel. We also introduce macroporousity to the DN gels and observe the effect on electrochemical properties. Finally, we investigate the shrinking/re-swelling behavior of PAAc gel in the presence of Cu(II) cations.

## 1.8. References


[1] H. Elahi, M. Eugeni, P. Gaudenzi, F. Qayyum, R.F. Swati, H.M. Khan, Response of piezoelectric materials on thermomechanical shocking and electrical shocking for aerospace applications, Microsyst. Technol. 24 (2018) 3791–3798. https://doi.org/10.1007/s00542-018-3856-8.

[2] H. Habibullah, 30 Years of atomic force microscopy: Creep, hysteresis, cross-coupling, and vibration problems of piezoelectric tube scanners, Meas. J. Int. Meas. Confed. 159 (2020) 107776. https://doi.org/10.1016/j.measurement.2020.107776.

[3] M.G. Ruppert, S.I. Moore, M. Zawierta, A.J. Fleming, G. Putrino, Y.K. Yong, Multimodal atomic force microscopy with optimized higher eigenmode sensitivity using on-chip piezoelectric actuation and sensing, Nanotechnology. 30 (2019). https://doi.org/10.1088/1361-6528/aae40b.

[4] Z. Zhu, X. Zhou, Z. Liu, R. Wang, L. Zhu, Development of a piezoelectrically actuated two-degree-of-freedom fast tool servo with decoupled motions for micro-/nanomachining, Precis. Eng. 38 (2014) 809–820. https://doi.org/10.1016/j.precisioneng.2014.04.009.

[5] J. Johari, J. Yunas, B.Y. Majlis, Piezoeletric micropump for drug delivery system fabricated using two optical masks, Adv. Mater. Res. 74 (2009) 279–282. https://doi.org/10.4028/www.scientific.net/AMR.74.279.

[6] M. Li, A. Pal, A. Aghakhani, A. Pena-Francesch, M. Sitti, Soft actuators for real-world applications, Nat. Rev. Mater. 7 (2022) 235–249. https://doi.org/10.1038/s41578-021-00389-7.

[7] Y. Kim, Y. Cha, Soft Pneumatic Gripper With a Tendon-Driven Soft Origami Pump, Front. Bioeng. Biotechnol. 8 (2020) 1–11. https://doi.org/10.3389/fbioe.2020.00461.

[8] J. Jiménez, J. Olea, J. Torres, I. Alonso, D. Harder, K. Fischer, Biography of Louis Braille and Invention of the Braille Alphabet, Surv. Ophthalmol. 54 (2009) 142–149. https://doi.org/10.1016/j.survophthal.2008.10.006.

[9] N.H. Runyan, F. Carpi, Seeking the “holy Braille” display: Might electromechanically active polymers be the solution?, Expert Rev. Med. Devices. 8 (2011) 529–532. https://doi.org/10.1586/erd.11.47.

[10] B. Mosadegh, A.D. Mazzeo, R.F. Shepherd, S.A. Morin, U. Gupta, I.Z. Sani, D. Lai, S. Takayama, G.M. Whitesides, Control of soft machines using actuators operated by a Braille display, Lab Chip. 14 (2014) 189–199. https://doi.org/10.1039/c3lc51083b.

[11] W. Yang, J. Huang, R. Wang, W. Zhang, H. Liu, J. Xiao, A Survey on Tactile Displays for Visually Impaired People, IEEE Trans. Haptics. 14 (2021) 712–721. https://doi.org/10.1109/TOH.2021.3085915.

[12] X. Wu, S.H. Kim, H. Zhu, C.H. Ji, M.G. Allen, A refreshable braille cell based on pneumatic microbubble actuators, J. Microelectromechanical Syst. 21 (2012) 908–916. https://doi.org/10.1109/JMEMS.2012.2190043.

[13] J.J. Zárate, H. Shea, Using pot-magnets to enable stable and scalable electromagnetic tactile displays, IEEE Trans. Haptics. 10 (2017) 106–112. https://doi.org/10.1109/TOH.2016.2591951.

[14] T. Matsunaga, K. Totsu, M. Esashi, Y. Haga, Tactile display using shape memory alloy micro-coil actuator and magnetic latch mechanism, Displays. 34 (2013) 89–94. https://doi.org/10.1016/j.displa.2013.03.001.

[15] metec AG, Hyberbraille F Display 6240, (2019) 2. https://web.metec-ag.de/downloads/hyperbraille-f.pdf.

[16] Orbit Research, Graphiti, (n.d.) 1. http://www.orbitresearch.com/ (accessed April 4, 2023).

[17] No Title, (n.d.). https://www.dotincorp.com/page/32?gbn2=DotCell (accessed May 27, 2023).

[18] N. Besse, S. Rosset, J.J. Zárate, E. Ferrari, L.G. Brayda, H.R. Shea, Understanding Graphics on a Scalable Latching Assistive Haptic Display Using a Shape Memory Polymer Membrane, IEEE Trans. Haptics. 11 (2018) 30–38.

[19] G. Frediani, J. Busfield, F. Carpi, Enabling portable multiple-line refreshable Braille displays with electroactive elastomers, Med. Eng. Phys. 60 (2018) 86–93. https://doi.org/10.1016/j.medengphy.2018.07.012.

[20] A. Russomanno, Z. Xu, S. O'Modhrain, B. Gillespie, A pneu shape display: Physical buttons with programmable touch response, 2017 IEEE World Haptics Conf. WHC 2017. (2017) 641–646. https://doi.org/10.1109/WHC.2017.7989976.

[21] R. Fei, W. Li, J. Li, L. Yang, Giant piezoelectricity of monolayer group IV monochalcogenides: SnSe, SnS, GeSe, and GeS, Appl. Phys. Lett. 107 (2015). https://doi.org/10.1063/1.4934750.

[22] L. Lu, W. Ding, J. Liu, B. Yang, Flexible PVDF based piezoelectric nanogenerators, Nano Energy. 78 (2020) 105251. https://doi.org/10.1016/j.nanoen.2020.105251.

[23] A. Bowles, A. Rahman, T. Jarman, P. Morris, J. Gore, A new technology for high density actuator arrays, Smart Struct. Mater. 2005 Smart Struct. Integr. Syst. 5764 (2005) 680. https://doi.org/10.1117/12.598455.

[24] T.H. Le, Y. Kim, H. Yoon, Electrical and electrochemical properties of conducting polymers, Polymers (Basel). 9 (2017). https://doi.org/10.3390/polym9040150.

[25] X. Guo, A. Facchetti, The journey of conducting polymers from discovery to application, Nat. Mater. 19 (2020) 922–928. https://doi.org/10.1038/s41563-020-0778-5.

[26] F. Hu, Y. Xue, J. Xu, B. Lu, PEDOT-Based Conducting Polymer Actuators, Front. Robot. AI. 6 (2019) 1–17. https://doi.org/10.3389/frobt.2019.00114.

[27] F.B. Madsen, A.E. Daugaard, S. Hvilsted, A.L. Skov, The Current State of Silicone-Based Dielectric Elastomer Transducers, Macromol. Rapid Commun. 37 (2016) 378–413. https://doi.org/10.1002/marc.201500576.

[28] G.Y. Gu, J. Zhu, L.M. Zhu, X. Zhu, A survey on dielectric elastomer actuators for soft robots, Bioinspiration and Biomimetics. 12 (2017). https://doi.org/10.1088/1748-3190/12/1/011003.

[29] M. Duduta, E. Hajiesmaili, H. Zhao, R.J. Wood, D.R. Clarke, Realizing the potential of dielectric elastomer artificial muscles, Proc. Natl. Acad. Sci. U. S. A. 116 (2019) 2476–2481. https://doi.org/10.1073/pnas.1815053116.

[30] T. Chen, O.R. Bilal, K. Shea, C. Daraio, Harnessing bistability for directional propulsion of soft, untethered robots, Proc. Natl. Acad. Sci. U. S. A. 115 (2018) 5698–5702. https://doi.org/10.1073/pnas.1800386115.

[31] R. Zentel, M. Brehmer, F. Brommel, G. Cordoyiannis, W.H. de Jeu, H. Finkelmann, D. Kramer, Z. Kutnjak, A. Lebar, C. Ohm, B.I. Ostrovskii, P. Palffy-Muhoray, K. Urayama, B. Zalar, Liquid Crystal Elastomers:Materials and Applications, Springer Berlin Heidelberg, 2017. https://doi.org/10.1201/9780203746684.

[32] Q. He, Z. Wang, Y. Wang, Z. Song, S. Cai, Recyclable and Self-Repairable Fluid-Driven Liquid Crystal Elastomer Actuator, ACS Appl. Mater. Interfaces. 12 (2020) 35464–35474. https://doi.org/10.1021/acsami.0c10021.

[33] C. Wang, K. Sim, J. Chen, H. Kim, Z. Rao, Y. Li, W. Chen, J. Song, R. Verduzco, C. Yu, Soft Ultrathin Electronics Innervated Adaptive Fully Soft Robots, Adv. Mater. 30 (2018) 1–9. https://doi.org/10.1002/adma.201706695.

[34] V. Cresta, G. Romano, A. Kolpak, B. Zalar, V. Domenici, Nanostructured composites based on liquid-crystalline elastomers, Polymers (Basel). 10 (2018) 1–27. https://doi.org/10.3390/polym10070773.

[35] R.S. Kularatne, H. Kim, J.M. Boothby, T.H. Ware, Liquid Crystal Elastomer Actuators : Synthesis , Alignment , and Applications, (2017) 395–411. https://doi.org/10.1002/polb.24287.

[36] F.M. Cheng, H.X. Chen, H.D. Li, Recent progress on hydrogel actuators, J. Mater. Chem. B. 9 (2021) 1762–1780. https://doi.org/10.1039/d0tb02524k.

[37] C. Yao, Z. Liu, C. Yang, W. Wang, X.J. Ju, R. Xie, L.Y. Chu, Poly(N-isopropylacrylamide)-clay nanocomposite hydrogels with responsive bending property as temperature-controlled manipulators, Adv. Funct. Mater. 25 (2015) 2980–2991. https://doi.org/10.1002/adfm.201500420.

[38] M. Liu, Y. Ishida, Y. Ebina, T. Sasaki, T. Hikima, M. Takata, T. Aida, An anisotropic hydrogel with electrostatic repulsion between cofacially aligned nanosheets, Nature. 517 (2015) 68–72. https://doi.org/10.1038/nature14060.

[39] E. Palleau, D. Morales, M.D. Dickey, O.D. Velev, Reversible patterning and actuation of hydrogels by electrically assisted ionoprinting, Nat. Commun. 4 (2013) 1–7. https://doi.org/10.1038/ncomms3257.

[40] W. Hong, Z. Liang, Programmed planar-to-helical shape transformations of composite hydrogels with bioinspired layered fibrous structures, 4 (2016). https://doi.org/10.1039/c6tb02178f.

[41] A.S. Gladman, E.A. Matsumoto, R.G. Nuzzo, L. Mahadevan, J.A. Lewis, Biomimetic 4D printing, 15 (2016). https://doi.org/10.1038/NMAT4544.

[42] Y. He, J. Tang, Y. Hu, S. Yang, F. Xu, M. Zrínyi, Y. Mei Chen, Magnetic hydrogel-based flexible actuators: A comprehensive review on design, properties, and applications, Chem. Eng. J. 462 (2023) 142193. https://doi.org/10.1016/j.cej.2023.142193.

[43] J.C. Breger, C. Yoon, R. Xiao, H.R. Kwag, M.O. Wang, J.P. Fisher, T.D. Nguyen, D.H. Gracias, Self-folding thermo-magnetically responsive soft microgrippers, ACS Appl. Mater. Interfaces. 7 (2015) 3398–3405. https://doi.org/10.1021/am508621s.

[44] Y. Li, G. Huang, X. Zhang, B. Li, Y. Chen, T. Lu, T.J. Lu, F. Xu, Magnetic hydrogels and their potential biomedical applications, Adv. Funct. Mater. 23 (2013) 660–672. https://doi.org/10.1002/adfm.201201708.

[45] S.R. Shin, S.M. Jung, M. Zalabany, K. Kim, P. Zorlutuna, S.B. Kim, M. Nikkhah, M. Khabiry, M. Azize, J. Kong, K.T. Wan, T. Palacios, M.R. Dokmeci, H. Bae, X. Tang, A. Khademhosseini, Carbon-nanotube-embedded hydrogel sheets for engineering cardiac constructs and bioactuators, ACS Nano. 7 (2013) 2369–2380. https://doi.org/10.1021/nn305559j.

[46] C. Yang, Z. Liu, C. Chen, K. Shi, L. Zhang, X.J. Ju, W. Wang, R. Xie, L.Y. Chu, Reduced Graphene Oxide-Containing Smart Hydrogels with Excellent Electro-Response and Mechanical Properties for Soft Actuators, ACS Appl. Mater. Interfaces. 9 (2017) 15758–15767. https://doi.org/10.1021/acsami.7b01710.

[47] I.K. Han, T. Chung, J. Han, Y.S. Kim, Nanocomposite hydrogel actuators hybridized with various dimensional nanomaterials for stimuli responsiveness enhancement, Nano Converg. 6 (2019). https://doi.org/10.1186/s40580-019-0188-z.

[48] A. Zhang, F. Wang, L. Chen, X. Wei, M. Xue, F. Yang, S. Jiang, 3D printing hydrogels for actuators: A review, Chinese Chem. Lett. 32 (2021) 2923–2932. https://doi.org/10.1016/j.cclet.2021.03.073.

[49] S. Qiao, H. Wang, Temperature-responsive polymers: Synthesis, properties, and biomedical applications, Nano Res. 11 (2018) 5400–5423. https://doi.org/10.1007/s12274-018-2121-x.

[50] B.S. Qin, Y. Geng, D.E. Discher, S. Yang, Temperature-Controlled Assembly and Release from Polymer Vesicles of Poly ( ethylene oxide ) - block -poly ( N - isopropylacrylamide )**, (2006) 2905–2909. https://doi.org/10.1002/adma.200601019.

[51] N. Ultrasound-responsive, J.L. Paris, M.V. Caba, Polymer-Grafted Mesoporous Silica, (2015) 11023–11033.

[52] Y. You, K.K. Kalebaila, S.L. Brock, D. Oupicky, Temperature-Controlled Uptake and Release in PNIPAM-Modified Porous Silica Nanoparticles, (2008) 3354–3359.

[53] S. Purushotham, R. V Ramanujan, Thermoresponsive magnetic composite nanomaterials for multimodal cancer therapy, Acta Biomater. 6 (2010) 502–510. https://doi.org/10.1016/j.actbio.2009.07.004.

[54] S. Mohammad, M. Abtahi, V. Anaraki, B. Farhood, S. Rabi, Assessment of photon energy and dose rate dependence of U-NIPAM polymer gel dosimeter, Radiat. Phys. Chem. 172 (2020) 108784. https://doi.org/10.1016/j.radphyschem.2020.108784.

[55] A. Karlsson, Dose integration and dose rate characteristics of a NiPAM polymer gel MRI dosimeter system Related content Dose integration and dose rate characteristics of a NiPAM polymer gel MRI dosimeter system, (2017). https://doi.org/10.1088/1742-6596/847/1/012063.

[56] G. Gao, J.F. Kadla, F. Ko, Enzymatic synthesis of ionic responsive lignin nano fi bres through surface, (2014) 3890–3898. https://doi.org/10.1039/c4gc00757c.

[57] A. Rosenthal, S. Rauch, K. Eichhorn, M. Stamm, Enzyme immobilization on protein-resistant PNIPAAm brushes : impact of biotin linker length on enzyme amount and catalytic activity, Colloids Surfaces B Biointerfaces. 171 (2018) 351–357. https://doi.org/10.1016/j.colsurfb.2018.07.047.

[58] W.J. Zheng, N. An, J.H. Yang, J. Zhou, Y.M. Chen, Tough Al-alginate/Poly(N - isopropylacrylamide) hydrogel with tunable LCST for soft robotics, ACS Appl. Mater. Interfaces. 7 (2015) 1758–1764. https://doi.org/10.1021/am507339r.

[59] C. Ma, W. Lu, X. Yang, J. He, X. Le, L. Wang, J. Zhang, M.J. Serpe, Y. Huang, T. Chen, Bioinspired Anisotropic Hydrogel Actuators with On – Off Switchable and Color-Tunable Fluorescence Behaviors, (n.d.). https://doi.org/10.1002/adfm.201704568.

[60] X. Zhang, C.L. Pint, M.H. Lee, B.E. Schubert, A. Jamshidi, K. Takei, H. Ko, A. Gillies, R. Bardhan, J. Urban, M. Wu, R. Fearing, A. Javey, Optically- and Thermally-Responsive Programmable Materials Based on Carbon Nanotube-Hydrogel Polymer Composites, (2011) 3239–3244.

[61] R. Liu, M. Fraylich, B.R. Saunders, Thermoresponsive copolymers: From fundamental studies to applications, Colloid Polym. Sci. 287 (2009) 627–643. https://doi.org/10.1007/s00396-009-2028-x.

[62] M.A. Haq, Y. Su, D. Wang, Mechanical properties of PNIPAM based hydrogels: A review, Mater. Sci. Eng. C. 70 (2017) 842–855. https://doi.org/10.1016/j.msec.2016.09.081.

[63] R.B. Yilmaz, Y. Chaabane, V. Mansard, Development of a Soft Actuator from Fast Swelling Macroporous PNIPAM Gels for Smart Braille Device Applications in Haptic Technology, ACS Appl. Mater. Interfaces. (2023). https://doi.org/10.1021/acsami.2c17835.

[64] J. Wang, L. Lin, Q. Cheng, L. Jiang, A strong bio-inspired layered PNIPAM-clay nanocomposite hydrogel, Angew. Chemie - Int. Ed. 51 (2012) 4676–4680. https://doi.org/10.1002/anie.201200267.

[65] M. Hua, D. Wu, S. Wu, Y. Alsaid, X. He, 4D Printable Tough and Thermoresponsive Hydrogels, (2021). https://doi.org/10.1021/acsami.0c17532.

[66] S.K. Ahn, R.M. Kasi, S.C. Kim, N. Sharma, Y. Zhou, Stimuli-Responsive Polymer Gels, Soft Matter. 4 (2008) 1151–1157. https://doi.org/10.1039/b714376a.

[67] M.C. Koetting, J.T. Peters, S.D. Steichen, N.A. Peppas, Stimulus-responsive hydrogels: Theory, modern advances, and applications, Mater. Sci. Eng. R Reports. 93 (2015) 1–49. https://doi.org/10.1016/j.mser.2015.04.001.

[68] W. Li, Q. Guan, M. Li, E. Saiz, X. Hou, Nature-inspired strategies for the synthesis of hydrogel actuators and their applications, Prog. Polym. Sci. 140 (2023) 101665. https://doi.org/10.1016/j.progpolymsci.2023.101665.

[69] K. Takada, N. Tanaka, T. Tatsuma, A redox actuator based on reversible formation of bond between poly(acrylic acid) gel and Cu2+ ion, J. Electroanal. Chem. 585 (2005) 120–127. https://doi.org/10.1016/j.jelechem.2005.07.024.

[70] T. Tatsuma, K. Takada, T. Miyazaki, UV-light-induced swelling and visible-light-induced shrinking of a TiO 2-containing redox gel, Adv. Mater. 19 (2007) 1249–1251. https://doi.org/10.1002/adma.200602386.

[71] V. Mansard, A macroporous smart gel based on a pH-sensitive polyacrylic polymer for the development of large size artificial muscles with linear contraction, Soft Matter. 17 (2021) 9644–9652. https://doi.org/10.1039/d1sm01078f.

[72] Y. Kageyama, N. Tanigake, Y. Kurokome, S. Iwaki, S. Takeda, K. Suzuki, T. Sugawara, Macroscopic motion of supramolecular assemblies actuated by photoisomerization of azobenzene derivatives, Chem. Commun. 49 (2013) 9386–9388. https://doi.org/10.1039/c3cc43488e.

[73] S. Sugiura, A. Szilágyi, K. Sumaru, K. Hattori, T. Takagi, G. Filipcsei, M. Zrínyi, T. Kanamori, On-demand microfluidic control by micropatterned light irradiation of a photoresponsive hydrogel sheet, Lab Chip. 9 (2009) 196–198. https://doi.org/10.1039/b810717c.

[74] Y. Zhao, C. Xuan, X. Qian, Y. Alsaid, M. Hua, L. Jin, X. He, Soft phototactic swimmer based on self-sustained hydrogel oscillator, Sci. Robot. 4 (2019) 1–11. https://doi.org/10.1126/scirobotics.aax7112.

[75] Z. Zhao, H. Wang, L. Shang, Y. Yu, F. Fu, Y. Zhao, Z. Gu, Bioinspired Heterogeneous Structural Color Stripes from Capillaries, Adv. Mater. 29 (2017) 1–8. https://doi.org/10.1002/adma.201704569.

[76] C. Yu, Z. Duan, P. Yuan, Y. Li, Y. Su, X. Zhang, Y. Pan, L.L. Dai, R.G. Nuzzo, Y. Huang, H. Jiang, J.A. Rogers, Electronically programmable, reversible shape change in two- and three-dimensional hydrogel structures, Adv. Mater. 25 (2013) 1541–1546. https://doi.org/10.1002/adma.201204180.

[77] K. Sumaru, T. Takagi, T. Satoh, T. Kanamori, Photo- and Thermoresponsive Dehydration of Spiropyran-Functionalized Polymer Regulated by Molecular Recognition, Macromol. Rapid Commun. 39 (2018) 1–6. https://doi.org/10.1002/marc.201700234.

[78] Y. Yang, Y. Tan, X. Wang, W. An, S. Xu, W. Liao, Y. Wang, Photothermal Nanocomposite Hydrogel Actuator with Electric-Field-Induced Gradient and Oriented Structure, ACS Appl. Mater. Interfaces. 10 (2018) 7688–7692. https://doi.org/10.1021/acsami.7b17907.

[79] A. Dallinger, P. Kindlhofer, F. Greco, A.M. Coclite, Multiresponsive Soft Actuators Based on a Thermoresponsive Hydrogel and Embedded Laser-Induced Graphene, ACS Appl. Polym. Mater. 3 (2021) 1809–1818. https://doi.org/10.1021/acsapm.0c01385.

[80] N. Kato, T. Morito, F. Takahashi, An energy-saving method of heating for a chemomechanical poly(N-isopropylacrylamide) gel with Joule's heat, Mater. Sci. Eng. C. 6 (1998) 27–31. https://doi.org/10.1016/S0928-4931(98)00032-0.

[81] M.A. Biot, General theory of three-dimensional consolidation, J. Appl. Phys. 12 (1941) 155–164. https://doi.org/10.1063/1.1712886.

[82] J. Yoon, S. Cai, Z. Suo, R.C. Hayward, Poroelastic swelling kinetics of thin hydrogel layers: comparison of theory and experiment, Soft Matter. 6 (2010) 6004. https://doi.org/10.1039/c0sm00434k.

[83] M.S. Silverstein, N.R. Cameron, PolyHIPEs - Porous Polymers from High Internal Phase Emulsions, Encycl. Polym. Sci. Technol. (2010). https://doi.org/10.1002/0471440264.pst571.

[84] P. Krajnc, D. Štefanec, I. Pulko, Acrylic acid “reversed” PolyHIPEs, Macromol. Rapid Commun. 26 (2005) 1289–1293. https://doi.org/10.1002/marc.200500353.

[85] N.C. Grant, A.I. Cooper, H. Zhang, Release of Polymeric Colloids via Hydrophilic Emulsion-Templated Porous Polymers, 2 (2010). https://doi.org/10.1021/am100049r.

[86] W. Busby, N.R. Cameron, C.A.B. Jahoda, Emulsion-derived foams (PolyHIPEs) containing poly(Sε-caprolactone) as matrixes for tissue engineering, Biomacromolecules. 2 (2001) 154–164. https://doi.org/10.1021/bm0000889.

[87] A. Barbetta, G. Rizzitelli, R. Bedini, R. Pecci, M. Dentini, Porous gelatin hydrogels by gas-in-liquid foam templating, Soft Matter. 6 (2010) 1785–1792. https://doi.org/10.1039/b920049e.

[88] H. Warren, D.J. Shepherd, M. in het Panhuis, D.L. Officer, G.M. Spinks, Porous PNIPAm hydrogels: Overcoming diffusion-governed hydrogel actuation, Sensors Actuators, A Phys. 301 (2020) 111784. https://doi.org/10.1016/j.sna.2019.111784.

[89] S.J. Bryant, J.L. Cuy, K.D. Hauch, B.D. Ratner, Photo-patterning of porous hydrogels for tissue engineering, Biomaterials. 28 (2007) 2978–2986. https://doi.org/10.1016/j.biomaterials.2006.11.033.

[90] Y. Cui, C. Tao, S. Zheng, Q. He, S. Ai, J. Li, Synthesis of Thermosensitive PNIPAM-co -MBAA Nanotubes by Atom Transfer Radical Polymerization within a Porous Membrane a, (2005) 1552–1556. https://doi.org/10.1002/marc.200500373.

## 2. Development of a Braille Device Utilizing Thermo-Sensitive Macroporous PNIPAM Hydrogel as the Fast Actuator

In this chapter, we demonstrate the development of a soft actuator based on a thermo-sensitive poly(n-isopropylacrylamide) (PNIPAM) gel. We introduced macroporosity to the gel (pores of 10 to 100 μm) to overcome the diffusion-which is the limiting factor- and reduced the gel response time from hours for bulk gels to seconds for macroporous gel. We studied the actuation and mechanical properties of porous gels. Also, we compared a mechanically reinforced nanocomposite gel (PNIPAM/Laponite) to a "classic" gel. Ultimately in this chapter, we developed a fast actuating gel with high cyclic performance and a single pin Braille device, enabling swift temperature control of the macroporous gel cylinder. We introduced a simple and cost-efficient alternative to existing actuators for Braille devices.

## 2.1. Introduction

In this study, we explore a new actuation strategy using mechanically active gels that are called smart gels [1–3]. We particularly focused on thermo-sensitive gels based on poly(N-isopropylacrylamide) (PNIPAM) [4,5]. The PNIPAM gel shows a volume phase transition with temperature. For temperatures above 34 °C, the PNIPAM gel shrinks reversibly with a very large swelling ratio (i.e., volume ratio between a swollen and shrunk gel sample), which can reach 1000% [6,7]. This large volume change is due to a modification of the solubility of the PNIPAM, which induces the transfer of water in or out of the polymer matrix [4,8,9]. The NIPAM monomer contains a hydrophilic amide and a hydrophobic propyl moiety. The prevailing characteristic of each moiety changes with the temperature. This results in a conformational change of molecules from a random coil (hydrophilic) at low temperature to a globule (hydrophobic) at high temperature.

PNIPAM gels are commonly used for drug delivery [10,11], dosimeter [12,13], and bio sensing [14] applications. Few studies have demonstrated that it can also be used for soft-actuation purposes [15,16]. A PNIPAM gel shows several key characteristics suitable for development of a smart braille tablet. Thanks to the very large swelling ratio, only a small quantity of active material is required to produce a large enough displacement (actuation). Furthermore, controlling the actuation only requires local control of the temperature. It can also be implemented relatively easily with small heating resistances. Furthermore, the low-temperature transition (below 40 °C) is user-friendly and safe with no risk of burning the user's finger.

Hydrogels face two major limitations for actuation: the high fragility of the polymer matrix and very slow response to stimuli. In this study, we combine two recent developments to overcome these limitations. The first development is the synthesis of a hydrogel with improved mechanical robustness [17–21] often called a tough gel. The second development is the synthesis of a fast-reacting gel with a macroporous structure [22]. These two scientific leaps which make a smart gel adapted to soft actuation are applied and results are described below.

For introducing macroporosity to the gels, we used scaffolding method. In this method, a sacrificial scaffold is produced with the desired pore shape and density. As the gel is polymerized and cross-linked around the scaffold, after selectively dissolving the scaffold material, a porous gel is acquired.

### 2.2. Macroporous Gels

The swelling kinetics of smart gels is controlled by the diffusion of water through the polymer matrix [23,24]. Bulk hydrogels behave as poroelastic media with a pore size of about 10−100 nm in diameter. Because of this small pore size, bulk gels are very slow to swell. Gel samples of 1.0 cm size take from hours to days to swell or shrink. Thus, fast actuation is only obtained for a thin layer of bulk gels of below 100 μm, in which the diffusion rate limitation is eliminated 52.

Synthesizing gels with larger pores facilitate the solvent transfer and accelerates the swelling speed [22,25]. Macroporous gels (MP gels) with pore sizes of about 10−100 μm in diameter show a fast-enough reaction for soft actuation. Thus, many methods have been developed for induction of macroporosity on hydrogels such as incorporation of sacrificial templates [22,25,26], sacrificial additives (e.g., poly(ethylene glycol)) [27], or solvent freezing [28–31]. Freezing the solvent contained in the gel offers a quick way to generate pores. For instance, Gil et al. [32] generated macropores with a diameter of 380 μm on a PNIPAM gel by freeze-drying. They were able to decrease the actuation time of a macroporous PNIPAM/silk hybrid hydrogel from 24 h to 1 min. Nevertheless, solvent freezing offers poor control on the pore structures, which highly depends on the freezing kinetics and therefore on the gel sample shape. In contrast, porosity based on a sacrificial template offers better control. For instance, Zhao et al. [26] developed macroporous PNIPAM gels with tunable pore sizes of between 20 to 70 μm using sacrificial dodecyl dimethyl benzyl ammonium bromide (DDBAB) particles, reducing the actuation time down to 1 min. In a similar strategy, Warren et al. [22] synthesized a macroporous PNIPAM- alginate hydrogel using sacrificial shellac fibers. The specific fiber shape of the sacrificial template is particularly suited as it ensures that the pores are interconnected for good solvent transfer and fast actuation speed.

In this study, we utilized sacrificial scaffolding method to induce macroporosity to the organically reticulated (OR) and nanocomposite (NC) gels. This method is based on producing a scaffold with the desired pore size, density and geometry. Afterwards, the scaffold is merged into the monomer solution so the monomer can penetrate inside and cover all the surfaces. After polymerization of PNIPAM, the scaffold is leached out to obtain hollow pore structures. Since gels are fragile and soft materials due to their low crosslinking density and average molecular weight, it is important to be able to selectively dispose of the scaffold without damaging polymer matrix. For example, we used PMMA as one of the scaffold materials which

requires ethyl acetate as the solvent. Such chemically violent solvent is very abrasive on the hydrogel matrix. The nanocomposite gel could not retain the physical crosslinks against such chemical and thus we could not use PMMA microspheres for porous NC gels. On the other hand, shellac is very beneficial in such manner since it is hydrophobic and easily dissolvable at high pH aqueous solutions while having very low (~70 °C) melting temperature. These properties make shellac the best candidate for scaffold materials in macroporous hydrogel production. The sintered PMMA micro spherical and melt spun shellac microfibrous scaffolds can be seen in Figure 2.1 a and b, respectively. Details on preparation of both bulk and macroporous OR and NC gels are in Appendix A.2.1-2.4.

We have observed good agreement between the scaffold morphology and the pores in the gels through SEM imaging and Confocal microscopy, respectively (Fig. 2.1). Thus, the porosity of the gels could be directly related to the scaffold density. For the LP gels, the measured porosity was 15% according to the microfibers packing density. This value could not be increased by compressing shellac fibers due to its brittle nature.

We can also estimate the pore sizes from the SEM images of the scaffold. The average diameters of spherical PMMA particles and shellac fibers were determined to be 75 ± 30 and 12 ± 5 μm, respectively. The average diameter of the fibers and spherical particles were determined from the SEM images. It was unfortunately not possible to obtain fibers with sizes similar to those of PMMA particles.

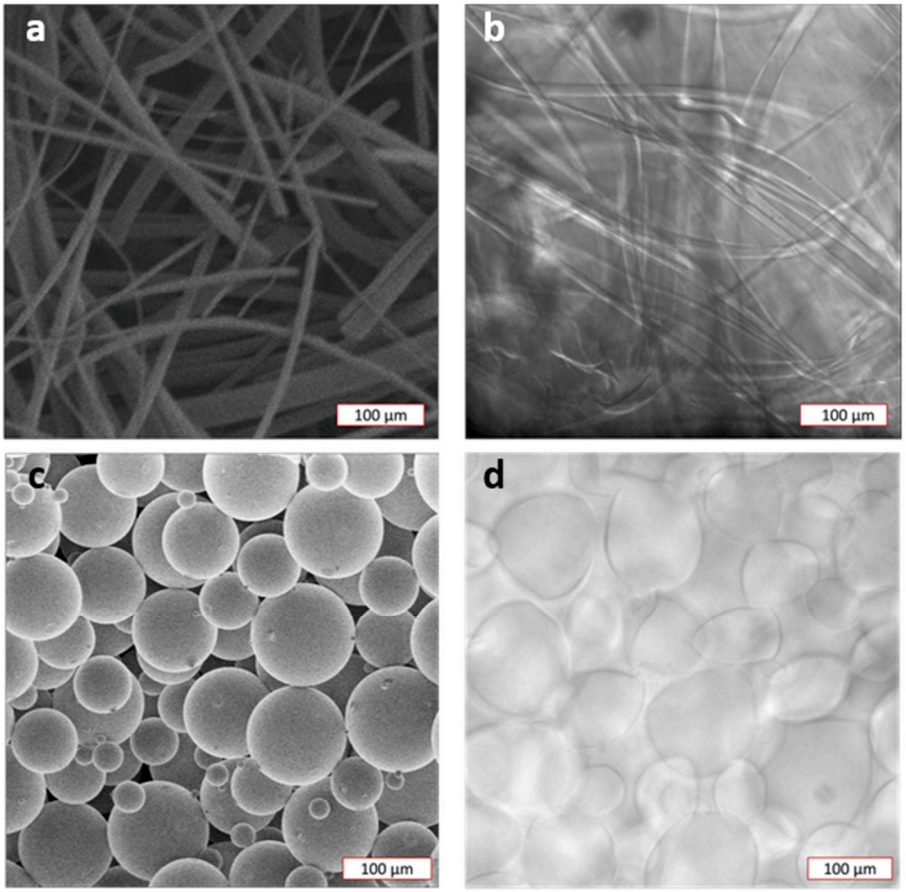



**Figure 2.1 :** (a, c) SEM images of the sacrificial template: (a) melt spun shellac fibers and (c) PMMA microspheres. (b, d) Images of the MP gel using DIC microscopy to observe the macroporosity: (b) LP-OR gel and (d) HP-NC gel. SEM images and DIC microscopy images are at the same scale to emphasize the similarity between the initial sacrificial scaffold and the final porosity. No SEM images of the porous gels are shown here, as drying the gel dramatically affects the gel structure.

### 2.3. Shrinking/Re-Swelling of PNIPAM Gels

Volume change of the gels upon shrinking/re-swelling was observed by dipping the gels into hot (60 °C) and cold (RT) water baths. The water baths size was kept much bigger than the gel volume (d x h = 7x10 mm) to ensure generation of symmetrical temperature gradient throughout the system. As the fully swollen gels at room temperature were dipped into hot water, very fast (≤1s) color change from transparent to opaque white occurred on the gel volume. This was due to the quick transition of the PNIPAM molecular structure from random coil to globular upon abrupt decrease in the hydrophilicity. Such change in hydrophilicty is triggered by increase of the temperature over the LCST of NIPAM at 34 °C. Such swift color change shows us that the temperature increase is very quick. On the other hand, the volume change does not occur as fast. This indicates the volume change rate of PNIPAM gels are controled fundementally by the diffusion kinetics of water. The classical way of determining the volume change rate/ratio of such gel samples include immersing the gels in hot/cold water baths, controlling the temperature and periodically the weighing the gels. From the direct relation between the gel weight and volume, the volume change rate/ratios are obtained. We indeed conducted such experiment in which the gel samples were immersed in hot/cold water and weighed periodically. According to the results (Fig. 2.2a), bulk OR and NC gels took 4 days, 2 h to reach 20%, 10% of their initial volume, respectively. The macroporous gel needed much less time to reach equilibrium shrunk volume which was 10% of their initial volumes. Since such method does not let us acquire high temporal resolution due to the time required for individual weighing, we could not obtain the shrinking rate data for the macroporus gels. The re-swelling experiment revealed that for all the samples, re-swelling was much slower than shrinking. Esspecially for the bulk gels, several days were needed to re-acquire only a fraction of their initial volume (Fig. 2.2b).

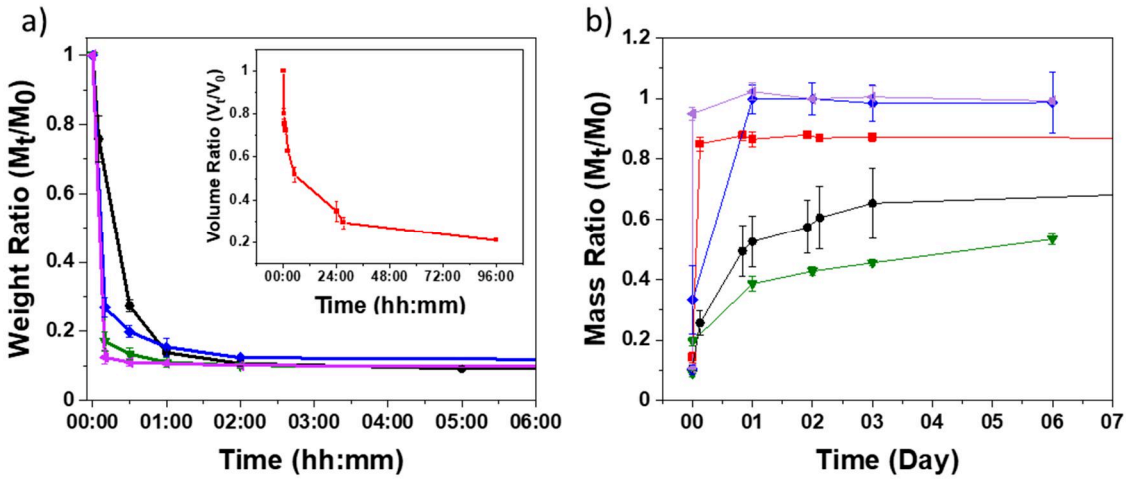



**Figure 2.2 :** Long-term (a) shrinking and (b) re-swelling graphs of PNIPAM gels. Data is obtained by periodic weighing of gels. Color indicators show red as OR, black as NC, green as LP-NC, blue as LP-OR and purple as HP-OR gels.

In order to overcome the drawbacks of weighing method such as low temporal resolution and possible air entrapment in the gel during partial drying, weighing process, we have developed an imaging method. In such experiment, we took images of the gel during shrinking/re-swelling of the gel upon immersing into water bath (Fig. 2.3). Such visualization of the gels provided high temporal resolution (1 image/s). We were able to obtain numerical data on the gel surface area with a simple image recognition algorithm on ImageJ. We deduced the evolution of volume from the change in the surface area, as the size variation was isotropic.

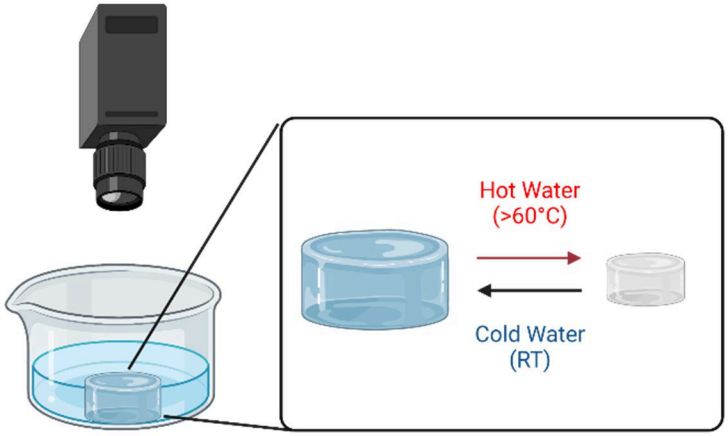



**Figure 2.3 :** Schematic of the real-time imaging setup for the shrinking/re-swelling tests.

MP gels showed a much faster shrinking dynamics than bulk gels, as expected. 20 s after the temperature increase, bulk OR gel and bulk NC gel only shrink to 90% and 80% of their initial volumes, respectively. However, on the same time scale, LP-OR and LP-NC gels

shrank to 50% and 40% of their initial volumes, respectively. Furthermore, HP-OR gels shrank to 20% in the first 20 s thanks to the higher porosity and larger pore sizes (Fig. 2.4a).

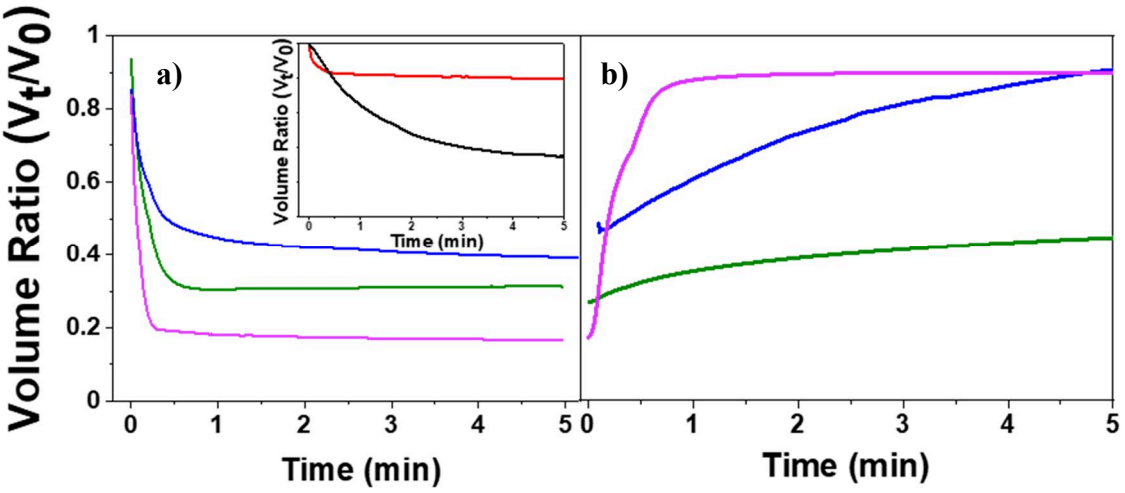



**Figure 2.4 :** Evolution of the volume ratio $V/V_0$ (where $V_0$ is the initial gel volume at room temperature before shrinking) as a function of time when the gel is successively dipped (b) in hot water and then (c) in cold water for (blue) LP-OR, (green) LP-NC, and (pink) HP-OR gel. The inset in (b) gives the dynamic of shrinking for bulk gel: (black) NC gel, (red) OR gel.

LP-NC gel shrank faster than LP-OR gel. This has been previously observed for bulk gels [33]. This acceleration is due to the presence of clay nanoparticles. They help to obtain larger nanopores. They also avoid the formation of a hydrophobic skin layer which prevents the water from being transported out of the gel.

After 30 s, the volume ratio of MP gels reached a plateau phase. The volume reached at the plateau depended on the gel porosity. It was equal to 20%, 30%, and 50% of the initial volume for respectively the HP-OR, LP-NC and LP-OR gels. This plateau was actually a pseudo-equilibrium stage. MP gel kept shrinking very slowly (less than 1% of volume change over 15 min). All samples reached about 10% of the initial volume after 24 h in hot water.

During the gel shrinking, the size of the pores decreased and eventually closed up. The pore closure would explain this pseudo equilibrium state. Introduction of larger pores (larger nanopores for LP-NC gel or larger macropores for HP-OR gel) helped to drain the water out of the gel. But it did not prevent the pore closure and the appearance of pseudo equilibrium where the gel is not fully shrunk. For actuation, we could not use the full amplitude of volume variation (i.e. a volume changing by a factor 10 between swollen and shrunk states). We could only use a smaller fraction of the amplitude (volume change by factors of 5, 3, and 2.5, respectively, for HP- OR, LP-NC, and LP-OR gel).

We then studied the gel re-swelling dynamic. To do so, we took the hot gel samples (which were at 60 °C for 5 min) and transferred them quickly to a water bath at room temperature (about 20 °C). Once again, we observed a very fast color change (from white to transparent) followed by the gel swelling.

The re-swelling dynamic did not show the same behavior as the shrinking. We need to distinguish OR and NC gels at this point (Figure 2.4b). For OR gels we observed that the introduction of macroporosity highly accelerated the swelling as expected. While it took 1 day for the bulk OR gel to regain 88% of its initial volume upon re-swelling, LP-OR and HP-OR gels needed only 4.5 and 1 min, respectively.

Nevertheless, we observed that re-swelling is significantly slower than shrinking. Such asymmetry with a slow re-swelling has been also observed for a bulk PNIPAM gel [27,32–35]. However, no extensive insight into this phenomenon is available. The slow re-swelling is thought to be due to the hysteresis upon fully closed (collapsed) pores resisting the inward solvent diffusion.

The difference of dynamic cannot be due to different heat transfer kinetics when we heated and then cooled the gel sample. The temperature change was produced by dipping the gel in a very large excess of water. Thus, heating and cooling happened at the same rate. Furthermore, we observed a very fast color change in ∼1 s, which indicated a very fast transition of molecular conformation between globular and random coil. To emphasize that heat transfer has no impact on the shrinking/swelling dynamic, we reproduced the experiments using a cold-water bath at three different temperatures: 20, 7, and 0 °C. We observed no significant difference of dynamics among the three different temperatures.

For a better understanding of the kinetic limitation in OR gel, we produced a gel with high porosity but a smaller pore size of 60 μm. This gel was called HP60μm-OR gel. It was produced with the same process as for the regular HP-OR gel but using smaller PMMA particles (diameter 60 ± 20 μm). The smaller PMMA microspheres can be seen from the SEM images on the sintered particles (Fig. 2.5).

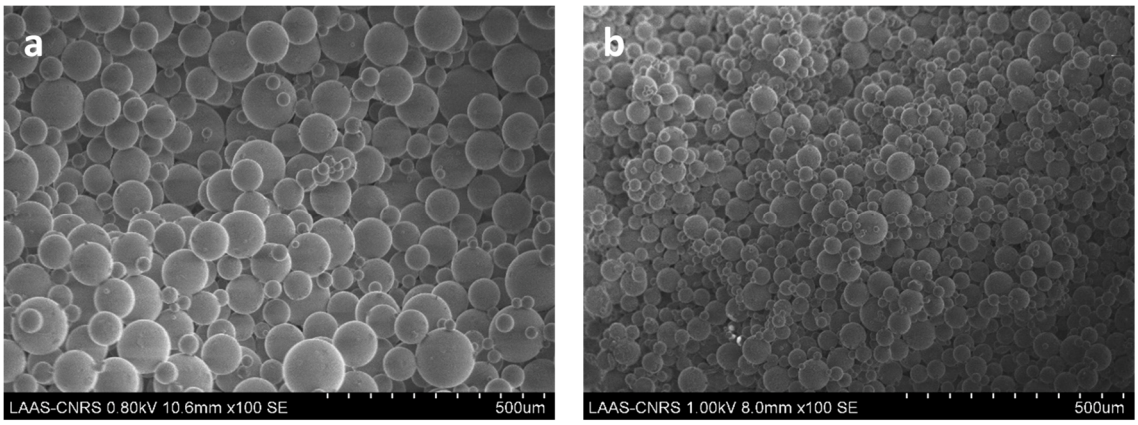



**Figure 2.5 :** SEM images of sintered PMMA scaffold cross-sections with average particle diameters of (a) 75 ± 30 µm and (b) 60 ± 20 µm.

Upon testing, we observed a slightly faster dynamic of shrinking and swelling than for the regular HP-OR gel (Table 2.1). This proved that convection through the macropores was not a limiting process, as convection would be slowed down for smaller pores. For HP-OR gel, the limiting kinetic factor remained to be the solvent diffusion through the gel walls to the macropores.

**Table 2.1 :** Shrinking/Re-swelling and modulus data of Porous PNIPAM gel samples.

| | Porosity | Pseudo-Equilibrium Volume (%) | $t_{shrink}$ (s) | $t_{swell}$ | Elastic Modulus (kPa) |
|---|---|---|---|---|---|
| NC | LP | 30 | 10 | >6h | 4 |
| OR | LP | 50 | 21 | 3 min | 18 |
| | HP (Big Pore) | 20 | 4 | 18 s | 3 |
| | HP (Small Pore) | 15 | 2 | 12 s | 1 |

Re-swelling of the LP-NC gel was much slower than that of the LP-OR gel. During the initial 5 min, the LP-NC gel re-swelled to only 45% of its initial volume, whereas the LP-OR gel reached 90%. Actually, LP-NC re-swelled even slower than bulk OR despite its macroporosity. And we observed a very similar swelling dynamics for both bulk and macroporous NC gel. These results suggested that the swelling kinetics of NC gel is not limited by the solvent transfer.

The very different time scales for swelling demonstrated that different limiting factors were involved for OR and NC gels. The slow dynamic of NC gel was probably due to reorganization of the Laponite nanoparticles interacting at a microscopic level. Indeed,

Laponite is made of disk-shaped nanoparticles carrying both positive and negative surface charges. They create electrostatic bonds between them to form a house-of-cards like structure. At high temperature, the gel shrank and the distance between nanoparticles decreased. The interaction between particles increased, which likely induced reorganization of the clay structure and formation of the new physical bonds. When we cooled the gel, this new clay network prevented the gel from swelling back. And the swelling kinetics was now controlled by the time required to disrupt the bonds between clay particles.

For actuation, it appeared that the swelling kinetics of PNIPAM gel was the limiting aspect. However, the discussion in the literature is often limited to the shrinking kinetics. For NC gel, the introduction of macroporosity does not accelerate the swelling. Thus, NC gel cannot be adapted for actuation. In contrast, MP gels based on the OR gel showed very interesting kinetics. Especially, HP-OR gel showed significant swelling and shrinking (within less than 30 s) thanks to the very large porosity levels.

The fast MP gel response enabled us to easily obtain the volume variation as a function of the temperature (Fig. 2.6). MP gel samples were dipped in water bath at room temperature and heated on a hot plate. The volume change was recorded by imaging while measuring the temperature increase. The heating rate (1 °C/min) was chosen to be slow enough to always be in the pseudo-equilibrium stage.

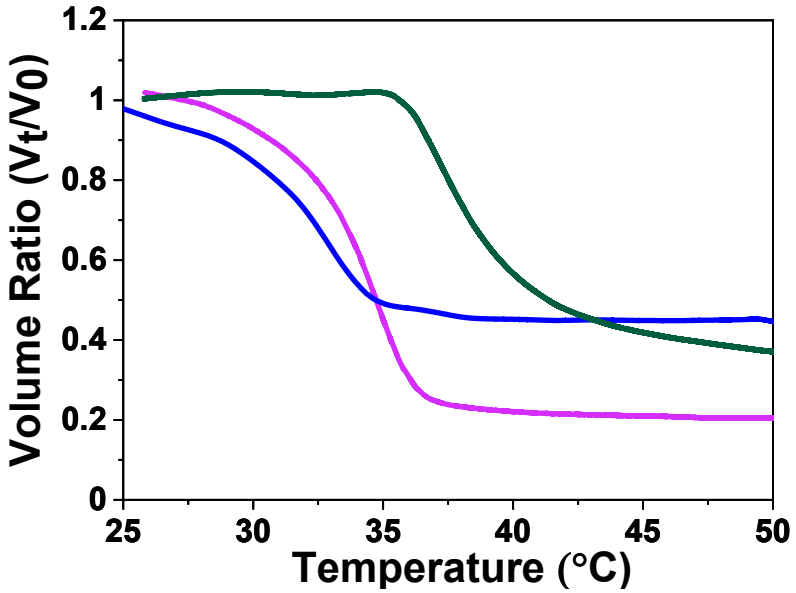



**Figure 2.6 :** Evolution of the volume ratios V/V0 (where V0 is the initial gel volume) as a function of temperature when we slowly raise the temperature of the surrounding water bath (at 1 °C/min) for (green) LP-NC, (blue) LP-OR, and (purple) HP-OR gel.

We observed a sharp volume transition at about 34 °C for the OR gels and 40 °C for NC gel. The volume reached at high temperature depended on the gel type and on the porosity. It complied with the volume reached at the plateau during the previous experiment.

## 2.4. Mechanical Properties of Macroporous PNIPAM Gels

### 2.4.1. Effect of Macroporosity on Mechanical Properties of PNIPAM Gels

All gel samples were characterized under compression which corresponds to the deformation applied to the sample in the braille setup. The details on the mechanical testing method is in appendix A.2.5. The samples showed an elastic linear response at deformation ε < 20%, from which we extracted the Young's modulus E (Fig. 2.7). Bulk OR gel showed a higher modulus than bulk NC gels. Actually, the modulus of our NC gels is lower than those reported in the literature [36]. Indeed, in our experiment the gel samples were kept in the water (and happened to swell) before measurement, while in other articles, the modulus was measured right after synthesis.

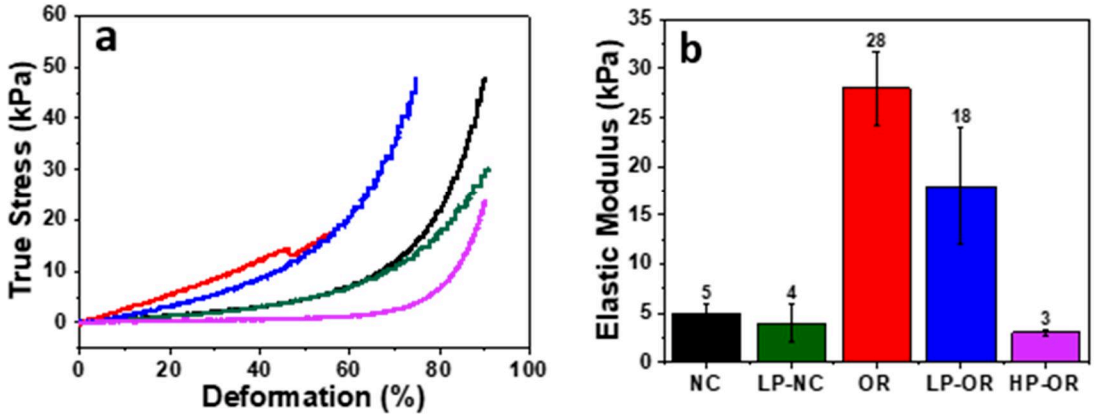



**Figure 2.7 :** (a) True stress−strain curves of (red) bulk OR, (black) bulk NC, (green) LP-NC, (blue) LP-OR, and (pink) HP-OR gel. (b) Elastic modulus values of the gel samples (same color coding).

The addition of macroporosity decreases the Young's modulus of the material. This decrease was dependent on the porosity. To characterize it, one calculates typically the modulus ratio between bulk material and porous material $E_{bulk}/E_{porous}$. If the modulus of the bulk material is the same as the modulus of the wall of the porous material, then the ratio depends only on the porosity ρ and is equal to;

$$\frac{E_{bulk}}{E_{porous}} = \frac{1}{(1-\rho)^2} \tag{2.1}$$

For both LP-OR and LP-NC gels we found $E_{bulk}/E_{LP}$ = 1.3− 1.5, which is compatible with a porosity of ρ= 15%

For HP-OR gel, the porosity has a stronger impact on the elastic modulus. We observed a modulus ratio $E_{bulk}/E_{HP} = 10$. This ratio was significantly larger than what we expected. It was not in agreement with eq 1 and the estimated porosity $\rho = 60\%$. This discrepancy was amplified for the $HP_{60\mu m}$-OR gel with a smaller pore size (Table 2.1). This MP gel had the same porosity as the regular HP-OR gel but showed a much lower modulus with $E_{bulk}/E_{HP60\mu m} = 28$. Furthermore, previous work studied an MP gel made of poly(acrylic acid) (PAA) which was produced with the same protocol and therefore presumably with the same porous structure [25]. PAA MP gels showed the modulus ratio $E_{bulk}/E_{porous} = 6$, which agrees with Eq. 2.1.

This important gel weakening (characterized by a modulus ratio larger than expected) probably happened during the selective dissolution of the solid template. The dissolution required the gel to be washed in ethyl acetate. It generated a change of solvent, which drove the gel to fully shrink. It created important mechanical stress on the sample, which could explain the observed weakening once the gel was swollen back in water. We believe that a process with no change of solvent would lead to MP gels able to sustain larger forces (about 2 times larger).

Introduction of porosity also improved the deformability and robustness of the gel. Bulk OR gel broke from a compressive strain of above 50%. LP-OR gel showed an improved maximum strain of 70%. HP-OR gel fully recovered its original shape even when compressed at a very high strain of 90% (Figure 2.8a). We tested all the MP gels under cyclic compression tests (Figure 2.8a−c). Even after 100 cycles, we observed only a very small modification of the mechanical properties and their moduli were decreased by less than 15%.

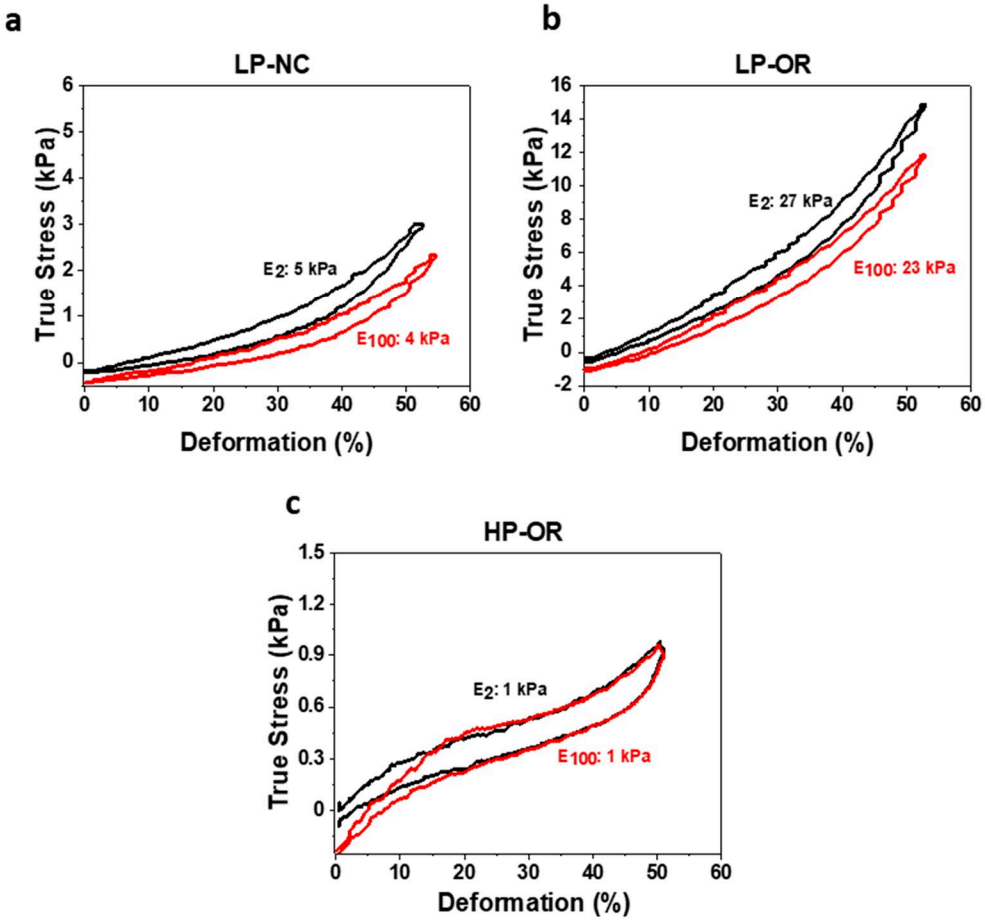



**Figure 2.8 :** (a−c) True stress versus strain graphs of gel samples under cycling deformation : (black) 1st cycle and (red) 100th cycle.

We also conducted tensile test on the HP-OR gel. The gel was glued (acrylic glue) to a transparent acetate paper from both ends of the cylinder (Fig. 2.9). The acetate papers were clamped to the tensile test heads. The speed of the test was selected to be the same as the compression test (2 mm/min) up to fracture. According to the result, the gel endured elongation up to 155% of its initial length having 40 kPa of tensile strength.

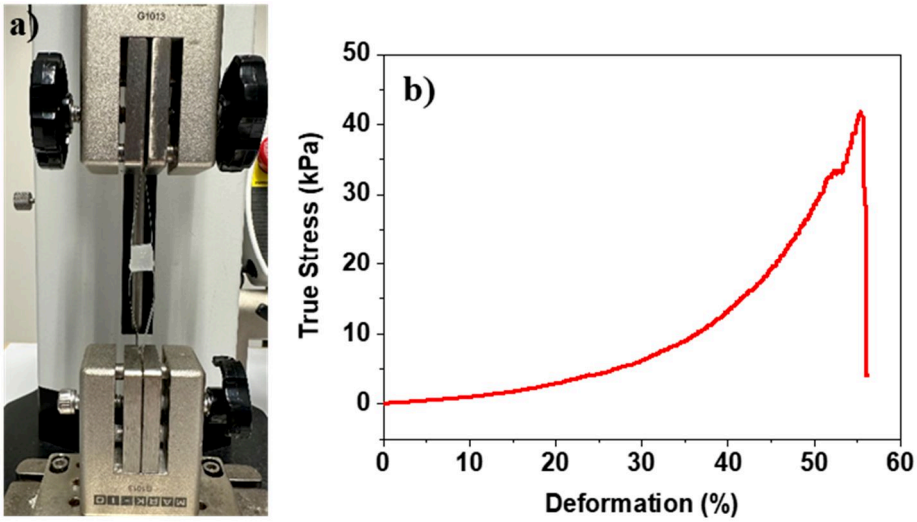



**Figure 2.9 :** a) Tensile test setup for the gel samples, b) tensile test data of the HP-OR gel.

Finally, smaller pored HP-OR gel was also mechanically analyzed with compression test. The resulting sample was tested with the same compression experiment and the results revealed an even lower elastic modulus (0.95 kPa) was observed (Fig. 2.10). This was due to the lower average particle size resulted in higher porosity and thus stronger plasticizing effect. As expected, the highly porous gel was also able to withstand 90% deformation upon compression.

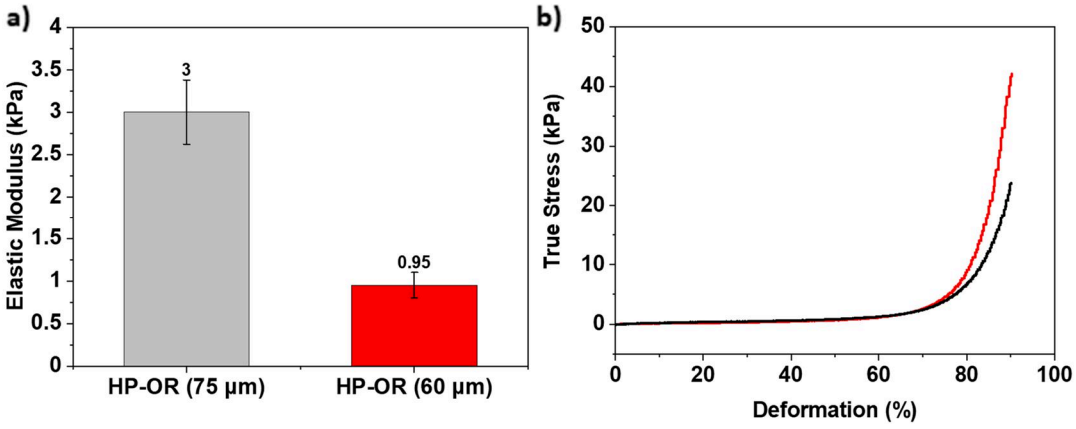



**Figure 2.10 :** (a) Elastic modulus data of HP-OR gels with different average pore diameters. (b) True stress/deformation curves of small pored (red) and big pored (black) HP-OR gel upon compression test.

## 2.5. Single Pin Braille Device

### 2.5.1. Fabrication of The Single Pin Braille Device

To demonstrate the capacity of our new actuation strategy, we built a single-pin braille setup (Fig. 2.11a, b). It consisted of a 3D-printed containment unit for the gel and water and a small pin which could move vertically through a hole in the center. A Peltier device (placed underneath the gel) and a nichrome electrical wire (wrapped around the gel) enabled respectively cooling and heating the system. A thin stainless-steel sheet was folded into a cylinder and was placed between the gel cylinder and the nichrome wire. It improved temperature homogeneity. It also reduced the friction to facilitate displacement of the plastic pin.

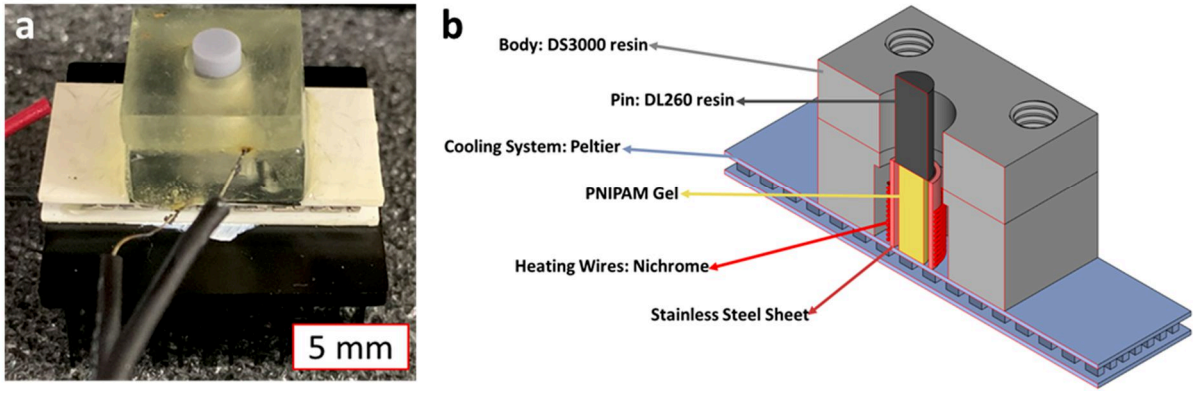



**Figure 2.11 :** (a, b) Image and 3D representation of the single-pin braille setup.

The nichrome wire has a high electrical resistance. It enables heating the system by a Joule effect. The heating power of the nichrome wire was controlled between 0 and 7.75 W using pulse width modulation (PWM) thanks to an Arduino microcontroller.

The heating/cooling power of the single pin braille setup is adjusted by using an Arduino microcontroller via pulse-width modulation. The power is referred in terms of percentage. Voltage fed to the nichrome wires or the Peltier is kept constant while the duration of the on/off state is controlled. As can be seen in Eq. 2.2, the ratio of the duration in which the voltage is fed to the system ($t_{on}$) to unit time ($t_{total}$= 1000 ms) is the controlled parameter in our experiments.

$$Power = \frac{t_{on}}{t_{total}} \times 100 \qquad (2.2)$$

We first investigated the capabilities of our system to tune the temperature. A thermocouple was positioned in place of the gel cylinder inside the containment unit that was filled only with water. We heated the system at constant power and observed a quick increase of the temperature which reached an equilibrium temperature after ~2 min. Both the equilibrium temperature and the heating speed increased with the heating power. The equilibrium was nearly linear with the heating power (Fig. 2.12a). It reached the transition temperature of 42 °C for a heating power of only 12% and could go up to 65 °C with 30% power. Higher power levels enabled obtaining much faster heating and higher temperatures. But they induced fast water evaporation. It is important to emphasize here that our PNIPAM hydrogel was always saturated and was in contact with water. We did not operate the gel in a dry or semidry state in any process.

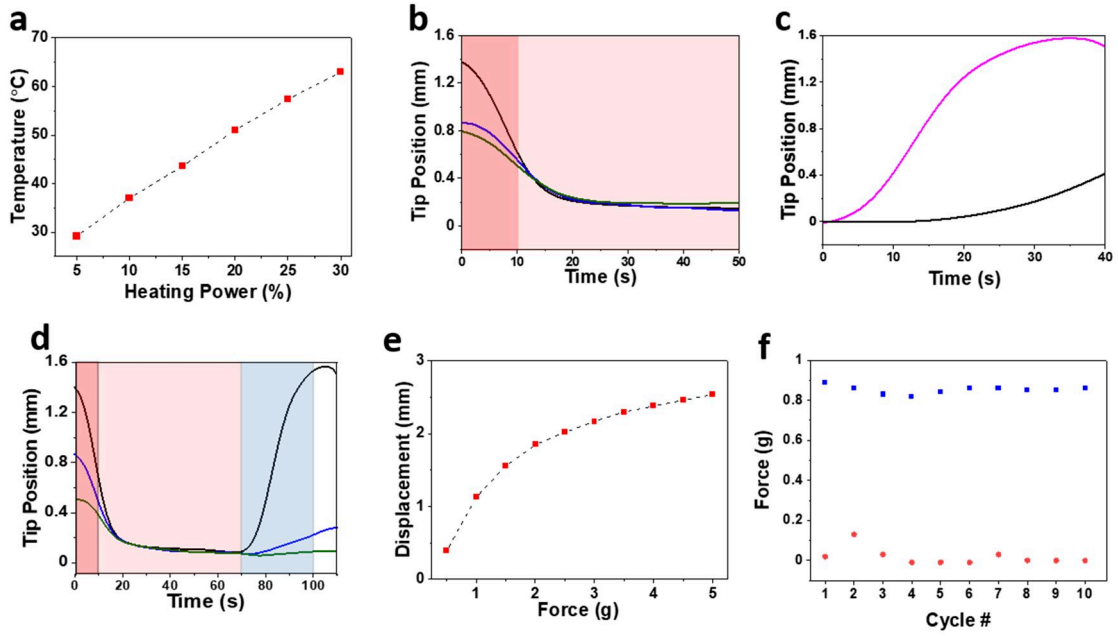



**Figure 2.12 :** (a) Equilibrium temperature of the gel containment unit as a function of the heating powers. (b) Evolution of the pin tip position as a function of time during forced heating under (black) no force or constant and (blue) 2.5 g and (green) 5.0 g forces applied. The heating procedures is as described: (dark red) 100% power for 10 s and (light red) 12% power. (c) Evolution of the pin position under (black) natural cooling and (blue) forced cooling. (d) Pin tip position during forced heating− forced cooling cycle under (black) no force or constant and (blue) 2.5 g and (green) 5.0 g forces applied. The heating procedure is as described previously. The forced cooling phase happens after 70 s and is shown in blue. (e) Pin tip displacement

versus applied force. (f) Minimum (red circle) and maximum (blue square) forces exerted by the braille tip over 10 heating−cooling cycles.

Upon measurement of the dynamic temperature during heating, we constructed the optimum heating program. We quickly increased the system temperature up to 40 °C by heating at 100% for 10 s. We then maintained the temperature above 34 °C by heating at 12%. This program ensured a very swift control over the temperature. We visually observed the gel during this heating procedure. We observed a quick color change (transparent to opaque white) of the entire gel cylinder (within less than 1 s) indicating a quick phase transition.

When we heated the system, we observed a rapid descent of the tip which start with a few-second delay. This delay corresponded to the time required to go above 34 °C. We observed a descent of the pin of 1.2 mm within less than 30 s (Fig. 2.12b). After 30 s we observed that the pin kept going down slowly (0.2 mm over 120 s). This slow descent did not correspond to the slow gel shrinking observed in the pseudo-equilibrium as the amplitude of the descent was too large. It was due to a slow increase of the overall temperature of the system.

When we turned off the heating, the system cooled naturally. The cooling was slow, and we observed that the tip ascends back to its initial position in 10 min (Fig. 2.12c). The Peltier plate below the gel enabled a significant acceleration of the cooling. It was powered at 2.5 A and enabled to remove of about 8 W from its top to bottom surface. The Peltier was very efficient in cooling the system. The tip climbed back to the initial position in only 35 s (Fig. 2.12c-d). Nevertheless, powering the Peltier plate required 12 W, which was dissipated into heat. It drove a temperature increase of the entire system (heat buildup). The heat sink placed underneath helped to cool the system.

In order to observe the active force exerted by the braille tip during cooling, we conducted a cyclic force test. Our force sensor was maintained at a fixed position over the tip. We then applied a heating/cooling cycle while the tip was maintained at the low position and we measured the force under an isostatic condition. The system was able to produce a force of 0.9 g over 10 cycles (Fig. 2.12f). The heating−cooling program was adjusted so that no heat buildup occurred even after all cycles. If we dipped the same HP-OR gel sample in a hot water bath, its height would quickly decrease from 5 to 2.9 mm. Therefore, we would expect a tip displacement of 2.1 mm, which is 30% larger than the 1.4 mm actually measured.

The single pin tip was tested under constant force to simulate the situation where a finger was kept on the pin tip throughout the actuation process (Fig. 2.12b, d, e). In the cold state, when we pressed on the tip it went down because of the gel softness. Nevertheless, we still observed a relatively important actuation amplitude. It was observed that when a certain force was applied to the gel at the swollen state, it pinched a bit (Fig. 2.12e). On the other hand, in the shrunk state the gel was stiff enough to hold the tip at its place.

This experiment with constant force applied to the pin tip simulated the situation in which a finger would be held on top of the pin throughout the actuation process. When 2.5 and 5.0 g forces were applied to the tip, 0.75 and 0.66 mm displacements upon actuation were achieved, respectively. On the other hand, 75% and 60% of total displacement achieved during heating was recovered after 10 min of natural cooling, respectively (Fig. 2.12c). These results showed that, even under 5.0 g of constant force on the braille tip, more than 0.5 mm of displacement was reversibly preserved.

Then, the same pin tip displacement measurements were done by utilizing the Peltier for cooling. Under 2.5 g of force, the braille pin tip descended for 0.8 mm upon heating but recovered 44% (0.35 mm) of the total displacement upon force cooling for 30 s. Similarly, when 5.0 g was applied, the pin tip descended for 0.5 mm, recovering only 8% (0.04 mm) (Fig. 2.12d).

From these results we can conclude that the same tip displacement could not be achieved under different stress conditions but the gel could still operate with considerable displacement values. According to the literature, these values are more than enough for a visually impaired individual to be able to sense the height difference of the pins during operation [37].

### 2.5.2. Thermal Efficiency Analysis of the Single Pin Braille Device

To understand the discrepancy between the two experiments, we simulated the temperature through the entire braille unit at equilibrium using the COMSOL software (Fig. 2.13a, b). In the simulation model, the heat was injected homogeneously from the nichrome, which was considered as a uniform 0.13 mm layer. The heat dissipation only happened through the bottom plate, which was maintained at room temperature (20 °C). Heat transport through the entire system only happened through diffusion, considering the heat diffusion coefficient of each specific material. The convection in the water part was neglected.

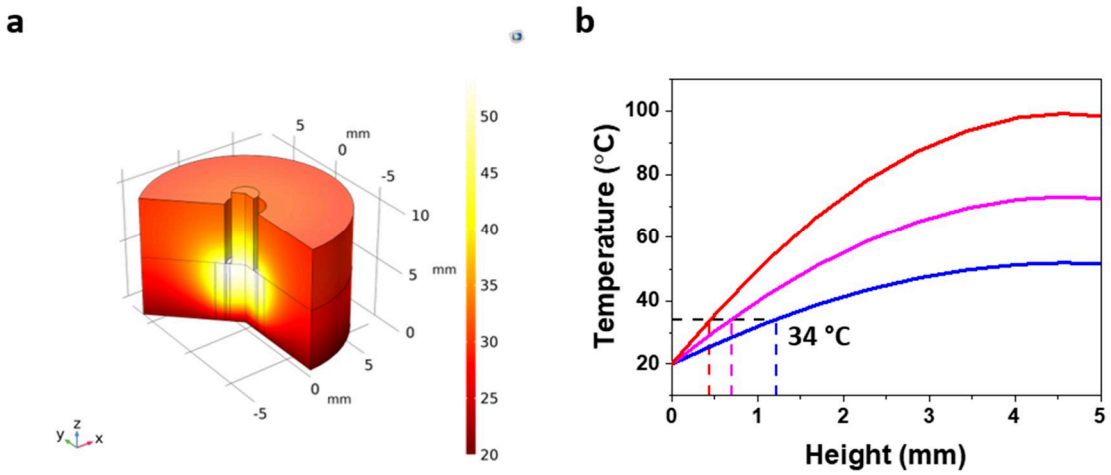



**Figure 2.13 :** (a, b) 3D temperature distribution for the single-pin braille device obtained from a COMSOL simulation operated at 12% heating power. (b) Temperature in the gel center along the vertical axis center at various heating powers: (blue) 12%, (purple) 20%, and (red) 30% power. Only a fraction of the gel was above the transition temperature (34 °C) and shrank.

The temperature through the gel was not homogeneous (Fig. 2.13a, b). It was maximum at the top of the gel and minimum at the bottom (Fig. 2.13), which was in contact with the plate where dissipation happened. Only a fraction of the gel had a temperature above the transition temperature (34 °C). Therefore, only a fraction of the gel was going to shrink. For instance, at a heating power of 12%, only the top 75% of the gel was above 34 °C and would shrink. Therefore, we expected the displacement to be only 2.1 mm × 75% = 1.6 mm.

The tip displacement can be modeled for various heating powers. At higher heating power, the maximum temperature increased and the gel fraction with a temperature above the transition temperature also increased. The tip displacement increased as a result. This prediction was actually confirmed with experiment. And we observed a good agreement

between the model and the experimental observation (Fig. 2.14). Despite its simplicity, our model shows that the temperature homogeneity is a limit to our system which reduces the actuation amplitude.

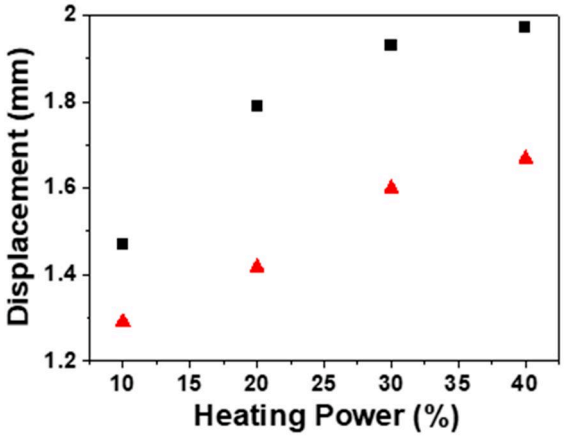



**Figure 2.14 :** Variation of the tip displacement amplitude for different heating powers: (red triangles) experimental measurement and (black squares) theoretical prediction based on COMSOL simulations.

## 2.6. Conclusions

In this study, a fast-actuating PNIPAM hydrogel was developed. The actuation speed was enhanced toward the requirements of a braille device. To do so, we accelerated the solvent diffusion by the introduction of macroporosity through the gel. We characterized the impact of two distinct pore geometries and densities. We demonstrated that measuring the re-swelling dynamic is critical, as swelling is much slower than shrinking. This difference of dynamics has also been observed in the literature but is poorly understood. Comprehension of this asymmetry would be key for future work. Nevertheless, producing a gel with a very high porosity enables a strong reduction of this asymmetry. Hence, the HP-OR gel showed a quick dynamic of both shrinking and re-swelling. Additionally, we tested a nanocomposite gel which showed enhanced mechanical robustness. Unfortunately, we demonstrated that this physically cross-linked gel did not perform optimally and was not suitable for actuation. It showed a very slow re-swelling dynamic which could not be improved by adding porosity.

The effect of macroporosity on the mechanical properties was also investigated. Adding porosity decreased the gel elastic modulus and therefore the potential force produced by the gel when swelling. Especially, HP-OR gel showed a more important modulus decrease than expected. This was probably due to an inadaptated process to generate macroporosity. Macroporous PNIPAM gel offers a high potential for future improvement.

The HP-OR gel showed good enough properties for actuation. Therefore, we have developed a cost-efficient braille device. We demonstrated that our device enabled quick tuning of the temperature of a water reservoir. An MP gel sample (placed in the center of the reservoir) could efficiently lift a pin. We demonstrated the cyclic performance and the high potential of our novel actuator for future smart braille devices. We also provided a precise analysis of the temperature distribution. This will help to improve the design of our device and to increase the heating efficiency. Especially, the development of a braille system with an array of pins (8 pins for a single array) is planned for a future work. This way we will be able to display letters and even images.

## 2.7. References


[1] E.S. Gil, S.M. Hudson, Stimuli-responsive polymers and their bioconjugates, Prog. Polym. Sci. 29 (2004) 1173–1222. https://doi.org/10.1016/j.progpolymsci.2004.08.003.

[2] S.-K. Ahn, R.M. Kasi, S.-C. Kim, N. Sharma, Y. Zhou, Stimuli-responsive polymer gels, Soft Matter. 4 (2008) 1151. https://doi.org/10.1039/b714376a.

[3] L. Ionov, Polymeric Actuators, Langmuir. 31 (2015) 5015–5024. https://doi.org/10.1021/la503407z.

[4] M.A. Haq, Y. Su, D. Wang, Mechanical properties of PNIPAM based hydrogels: A review, Mater. Sci. Eng. C. 70 (2017) 842–855. https://doi.org/10.1016/j.msec.2016.09.081.

[5] J. Liu, L. Jiang, S. He, J. Zhang, W. Shao, Recent progress in PNIPAM-based multi-responsive actuators: A mini-review, Chem. Eng. J. 433 (2022) 133496. https://doi.org/10.1016/j.cej.2021.133496.

[6] K. Depa, A. Strachota, M. Šlouf, J. Hromádková, Fast temperature-responsive nanocomposite PNIPAM hydrogels with controlled pore wall thickness: Force and rate of T-response, Eur. Polym. J. 48 (2012) 1997–2007. https://doi.org/10.1016/j.eurpolymj.2012.09.007.

[7] H. Hosseini, H. Tenhu, S. Hietala, Rheological properties of thermoresponsive nanocomposite hydrogels, J. Appl. Polym. Sci. 133 (2016) 2–7. https://doi.org/10.1002/app.43123.

[8] S. Kim, K. Lee, C. Cha, Refined control of thermoresponsive swelling/deswelling and drug release properties of poly(N-isopropylacrylamide) hydrogels using hydrophilic polymer crosslinkers, J. Biomater. Sci. Polym. Ed. 27 (2016) 1698–1711. https://doi.org/10.1080/09205063.2016.1230933.

[9] S. Belali, H. Savoie, J.M. O'Brien, A.A. Cafolla, B. O'Connell, A.R. Karimi, R.W. Boyle, M.O. Senge, Synthesis and Characterization of Temperature-Sensitive and Chemically Cross-Linked Poly(N-isopropylacrylamide)/Photosensitizer Hydrogels for Applications in Photodynamic Therapy, Biomacromolecules. 19 (2018) 1592–1601. https://doi.org/10.1021/acs.biomac.8b00293.

[10] J. Li, D.J. Mooney, Designing hydrogels for controlled drug delivery, Nat. Rev. Mater. 1 (2016) 1–18. https://doi.org/10.1038/natrevmats.2016.71.

[11] Y. Chen, W. Liu, G. Zeng, Y.J. Liu, Microporous PDMAEMA-based stimuli-responsive hydrogel and its application in drug release, J. Appl. Polym. Sci. 134 (2017) 1–12. https://doi.org/10.1002/app.45326.

[12] V. Anaraki, S.M.M. Abtahi, B. Farhood, M. Ejtemai-fard, A novel method for increasing the sensitivity of NIPAM polymer gel dosimeter, Radiat. Phys. Chem. 153 (2018) 35–43. https://doi.org/10.1016/j.radphyschem.2018.09.006.

[13] R.J. Senden, P. De Jean, K.B. McAuley, L.J. Schreiner, Polymer gel dosimeters with reduced toxicity: A preliminary investigation of the NMR and optical dose-response using different monomers, Phys. Med. Biol. 51 (2006) 3301–3314. https://doi.org/10.1088/0031-9155/51/14/001.

[14] S. Inal, J.D. Kölsch, F. Sellrie, J.A. Schenk, E. Wischerhoff, A. Laschewsky, D. Neher, A water soluble fluorescent polymer as a dual colour sensor for temperature and a specific protein, J. Mater. Chem. B. 1 (2013) 6373–6381. https://doi.org/10.1039/c3tb21245a.

[15] X. Hu, Z. Ge, X. Wang, N. Jiao, S. Tung, L. Liu, Multifunctional thermo-magnetically actuated hybrid soft millirobot based on 4D printing, Compos. Part B Eng. 228 (2022) 109451. https://doi.org/10.1016/j.compositesb.2021.109451.

[16] J.C. Breger, C. Yoon, R. Xiao, H.R. Kwag, M.O. Wang, J.P. Fisher, T.D. Nguyen, D.H. Gracias, Self-folding thermo-magnetically responsive soft microgrippers, ACS Appl. Mater. Interfaces. 7 (2015) 3398–3405. https://doi.org/10.1021/am508621s.

[17] J.P. Gong, Y. Katsuyama, T. Kurokawa, Y. Osada, Double-network hydrogels with extremely high mechanical strength, Adv. Mater. 15 (2003) 1155–1158. https://doi.org/10.1002/adma.200304907.

[18] W.J. Zheng, N. An, J.H. Yang, J. Zhou, Y.M. Chen, Tough Al-alginate/Poly(N - isopropylacrylamide) hydrogel with tunable LCST for soft robotics, ACS Appl. Mater. Interfaces. 7 (2015) 1758–1764. https://doi.org/10.1021/am507339r.

[19] Q. Chen, H. Chen, L. Zhu, J. Zheng, Fundamentals of double network hydrogels, J. Mater. Chem. B. 3 (2015) 3645–3886. https://doi.org/10.1039/C5TB00123D.

[20] E.S. Gil, S.M. Hudson, Effect of silk fibroin interpenetrating networks on swelling/deswelling kinetics and rheological properties of poly(N-isopropylacrylamide) hydrogels, Biomacromolecules. 8 (2007) 258–264. https://doi.org/10.1021/bm060543m.

[21] J. Wang, L. Lin, Q. Cheng, L. Jiang, A strong bio-inspired layered PNIPAM-clay nanocomposite hydrogel, Angew. Chemie - Int. Ed. 51 (2012) 4676–4680. https://doi.org/10.1002/anie.201200267.

[22] H. Warren, D.J. Shepherd, M. in het Panhuis, D.L. Officer, G.M. Spinks, Porous PNIPAm hydrogels: Overcoming diffusion-governed hydrogel actuation, Sensors Actuators, A Phys. 301 (2020) 111784. https://doi.org/10.1016/j.sna.2019.111784.

[23] M. Quesada-Pérez, J.A. Maroto-Centeno, J. Forcada, R. Hidalgo-Alvarez, Gel swelling theories: the classical formalism and recent approaches, Soft Matter. 7 (2011) 10536. https://doi.org/10.1039/c1sm06031g.

[24] J. Yoon, S. Cai, Z. Suo, R.C. Hayward, Poroelastic swelling kinetics of thin hydrogel layers: Comparison of theory and experiment, Soft Matter. 6 (2010) 6004–6012. https://doi.org/10.1039/c0sm00434k.

[25] V. Mansard, A macroporous smart gel based on a pH-sensitive polyacrylic polymer for the development of large size artificial muscles with linear contraction, Soft Matter. 17 (2021) 9644–9652. https://doi.org/10.1039/d1sm01078f.

[26] Q. Zhao, J. Sun, Q. Ling, Q. Zhou, Synthesis of macroporous thermosensitive hydrogels: A novel method of controlling pore size, Langmuir. 25 (2009) 3249–3254. https://doi.org/10.1021/la8038939.

[27] B. Ziółkowski, L. Florea, J. Theobald, F. Benito-Lopez, D. Diamond, Porous self-protonating spiropyran-based NIPAAm gels with improved reswelling kinetics, J. Mater. Sci. 51 (2016) 1392–1399. https://doi.org/10.1007/s10853-015-9458-2.

[28] K. Haraguchi, H.J. Li, Mechanical properties and structure of polymer-clay nanocomposite gels with high clay content, Macromolecules. 39 (2006) 1898–1905. https://doi.org/10.1021/ma052468y.

[29] G. Huerta-Angeles, K. Hishchak, A. Strachota, B. Strachota, M. Šlouf, L. Matějka, Super-porous nanocomposite PNIPAm hydrogels reinforced with titania nanoparticles, displaying a very fast temperature response as well as pH-sensitivity, Eur. Polym. J. 59 (2014) 341–352. https://doi.org/10.1016/j.eurpolymj.2014.07.033.

[30] Y. Alsaid, S. Wu, D. Wu, Y. Du, L. Shi, R. Khodambashi, R. Rico, M. Hua, Y. Yan, Y. Zhao, D. Aukes, X. He, Tunable Sponge-Like Hierarchically Porous Hydrogels with Simultaneously Enhanced Diffusivity and Mechanical Properties, Adv. Mater. 33 (2021) 1–9. https://doi.org/10.1002/adma.202008235.

[31] M. Hua, S. Wu, Y. Ma, Y. Zhao, Z. Chen, I. Frenkel, J. Strzalka, H. Zhou, X. Zhu, X. He, Strong tough hydrogels via the synergy of freeze-casting and salting out, Nature. 590 (2021) 594–599. https://doi.org/10.1038/s41586-021-03212-z.

[32] E.S. Gil, S.-H. Park, L.W. Tien, B. Trimmer, S.M. Hudson, D.L. Kaplan, Mechanically Robust, Rapidly Actuating, and Biologically Functionalized Macroporous Poly( *N* -isopropylacrylamide)/Silk Hybrid Hydrogels, Langmuir. 26 (2010) 15614–15624. https://doi.org/10.1021/la102509a.

[33] K. Haraguchi, T. Takehisa, S. Fan, Effects of clay content on the properties of nanocomposite hydrogels composed of poly(N-isopropylacrylamide) and clay, Macromolecules. 35 (2002) 10162–10171. https://doi.org/10.1021/ma021301r.

[34] K. Depa, A. Strachota, M. Šlouf, J. Brus, Poly(N-isopropylacrylamide)-SiO2 nanocomposites interpenetrated by starch: Stimuli-responsive hydrogels with attractive tensile properties, Eur. Polym. J. 88 (2017) 349–372. https://doi.org/10.1016/j.eurpolymj.2017.01.038.

[35] Z. Deng, R. Yu, B. Guo, Stimuli-responsive conductive hydrogels: Design, properties, and applications, Mater. Chem. Front. 5 (2021) 2092–2123. https://doi.org/10.1039/d0qm00868k.

[36] K. Haraguchi, L. Song, Microstructures formed in co-cross-linked networks and their relationships to the optical and mechanical properties of PNIPA/clay nanocomposite gels, Macromolecules. 40 (2007) 5526–5536. https://doi.org/10.1021/ma070695p.

[37] N.H. Runyan, F. Carpi, Seeking the “holy Braille” display: Might electromechanically active polymers be the solution?, Expert Rev. Med. Devices. 8 (2011) 529–532. https://doi.org/10.1586/erd.11.47.

## 3. Characterization of Poroelastic Properties of Macroporous PNIPAM Hydrogel

In this chapter we demonstrate our studies conducted to investigate the poroelastic properties of macroporous PNIPAM hydrogel. Attaining full control over the pore geometry and the level of gel porosity was crucial to thoroughly analyze the poroelastic properties of hydrogels. Thus, we first developed a novel sacrificial scaffold from shellac by melt extrusion 3D printing method. By using such method, we were able to achieve porosities in the range of 30-50 % (v/v) in the gel matrix. Moreover, we conducted the same imaging method mentioned in the previous chapter on 60% porous gels produced by PMMA templates and 50% porous gel produced with 3D printed scaffold. We calculated the diffusion constant of water through the gel during swelling with the help of the Biot's theory of poroelasticity. Lastly, we constructed an experimental setup and obtained a controlled (water pressure and temperature) flow through macroporous gel matrix. Since diffusion of water through the poroelastic matrix obeys the Darcy's law, flow rate of water is directly related to the pressure field gradient, viscosity of water and the permeability of the gel. Using such relation, we were able to acquire the permeability data of the macroporous gel. Moreover, we also observed and analyzed the poroelastic deformation of the gel upon compression by the fluid flow. By flowing hot water through the gel, we were also able to obtain the evolution of pressure gradient, decreasing flow rate and eventually the change in water permeability of the gel upon shrinking.

### 3.1. Introduction

In this study we aimed to develop a macroporous gel with controlled porosity and characterize its poroelastic properties. As previously, we used sacrificial scaffolding technique to introduce macroporosity to the gel since it provides high control over the pore geometries and the porosity level of the resulting gel. In such method, the polymeric gel is formed around a solid sacrificial template which can be selectively dissolved at the end to acquire a macroporous matrix.

In the previous chapter we used PMMA microspheres as the building blocks of our scaffold. This material provided very high porosity value (60% v/v) but changing the porosity was not possible since packing density was at its natural limit. Moreover, we had to use ethyl acetate to leach the PMMA out of the hydrogel which is a chemically violent solvent affecting the gel matrix in the process.

For this reason, we started to work with another material called shellac to produce sacrificial scaffolds. Shellac is a natural material which melts easily at 75-80 °C [1]. Moreover, while shellac is insoluble in water, it is soluble in high pH aqueous solutions. This property makes shellac a very advantageous material to be utilized in sacrificial scaffolding process for producing macroporous hydrogels.

We initially produced microfibers by melt spinning shellac (A.2.4). We were able to obtain fibrous scaffolds but we could not control the level of porosity in the gel since we could not compress the fibers. The melt spun shellac fibers were too brittle and broke into smaller fibers upon smallest compressive forces. Thus, we were not able to obtain densely packed scaffolds which limited the gel porosity to maximum 15% (v/v).

In this chapter we introduce a novel approach to produce a scaffold which enable to obtain controlled porosity. We used 3D printing method to produce a sacrificial template. The commercial materials for 3D printing such as polylactic acid (PLA), polyurethane (PU) or polyvinylalcohol (PVA) were not suitable for our case since they either do not easily dissolve without affecting the hydrogel itself or soluble in water therefore cannot withstand the hydrogel production process.

We used melt extrusion printing to obtain shellac scaffolds. Since shellac was not used before for 3D printing, we first conducted optimization experiments on the process parameters such as nozzle temperature, extrusion pressure and print head speed. We designed the scaffolds

to obtain specific porosities. By writing gcode commands, we printed multilayered grid design with variable volumetric (v/v) densities. We were able to control the porosity level of the gel between 30-50 % by such method.

We analyzed the swelling process of the macroporous gels via the imaging method mentioned in the previous chapter. With the help of the Biot's theory of poroelasticity, we were able to calculate the diffusion coefficient of water through the macroporous gel matrices during swelling.

Moreover, we constructed a setup to obtain a controlled flow through our macroporous PNIPAM gels. We acquired the flow rate and inlet/outlet pressure data. Since such flow through porous media was in good agreement with Darcy's law, we were able to obtain the permeability data of the gel.

Finally, we were able to observe the increase in the pressure gradient while decrease in the flow rate upon controlled increase of the fluid temperature which led to shrinking of the gel. We were not able to obtain accurate permeability of the shrunk gel because of the cracks at the hydrogel/silicone interface at high temperatures.

### 3.2. Development of 3D Printed Shellac Scaffolds

For 3D printing, we used melt extrusion method. Shellac melts at 75-80 °C which makes it a suitable material for melt extrusion. We used the Bio-X (Cellink) 3D printer. For the design of the template, we used GCode on the dedicated software "HeartWare" (Cellink). For the template, we used layers with grid design (Fig 3.4a, b). By adjusting the distance in between adjacent lines, we were able to change the overall density of the structure.

Before starting optimization of parameters, we checked the nozzle diameter. Thus, we took images of the nozzle by optical microscope and verified the actual nozzle diameter. The nozzle had average tip internal diameter of 0.3 mm. We used this number in the coming steps of optimization process.

Ideally, the optimum parameters should result in printed lines with the exact same diameter of the nozzle used. Having thicker lines means either applied pressure, temperature is too high or printing speed is too low. Either way it is a sign of excess material is being extruded. Thus, homogeneity cannot be obtained throughout the printing. The opposite is also problematic. When the printed lines are thinner than the nozzle diameter, it is a sign that not enough material is being extruded.

Naturally produced by an organism (bug), shellac has a composite macromolecular structure composed of different polyesters. Thus, it shows slight variances in its physical properties depending on the origin and types of processing applied. Shellac does not have a distinct melting point. It starts to soften at 65-70 °C and melt at about 80 °C [1].

We realized that below 90 °C, continuous extrusion was not possible due to the high viscosity of shellac. Also, upon trying 100 °C for printing, we realized that the viscosity if the molten shellac started to increase back. This was due to the esterification induced polymerization of shellac which is catalyzed at high temperatures. Thus, we decided to use the 92.5 °C as the printing temperatures since it allowed more precise printing along with slightly higher shellac viscosity. This way, we were able to print for 1 hour until shellac viscosity increased beyond extrudable point.

Then we optimized the applied pressure to extrude molten shellac during printing. We printed parallel vertical lines by applying different pressures and analyzed them by using optical microscope images. We used 92.5 °C as the nozzle temperature and 7 mm/s as the nozzle speed during printing. According to the results, lines printed with 20, 30 and 40 kPa all

had homogeneous thicknesses of 280, 360 and 420 µm, respectively (Fig. 3.1a-c). These results showed that 20 kPa was too low while 30 and 40 kPa pressures resulted in excess material extrusion. On the other hand, considering the slight increase of shellac viscosity along the printing, the thickness of the printed lines would eventually decrease. Thus, we chose 30 kPa as the optimum printing pressure.

Moreover, we conducted the same experiment by changing the travel speed of nozzle during printing. For this, we used 1, 5 and 7 mm/s to print straight lines. According to the results, with 1, 3 and 5 mm/s nozzle speeds, lines with 280, 320 and 580 µm thicknesses were achieved, respectively (Fig. 3.1d-f). Again, we chose 5 mm/s as the printing head (nozzle) speed since it produced slightly thicker lines without any inhomogeneities throughout the printing. As our main design required printing many layers on top of each, the thickness would eventually decrease with increasing viscosity. Printing the whole design would take 45-60 minutes depending on the spacing between adjacent lines.

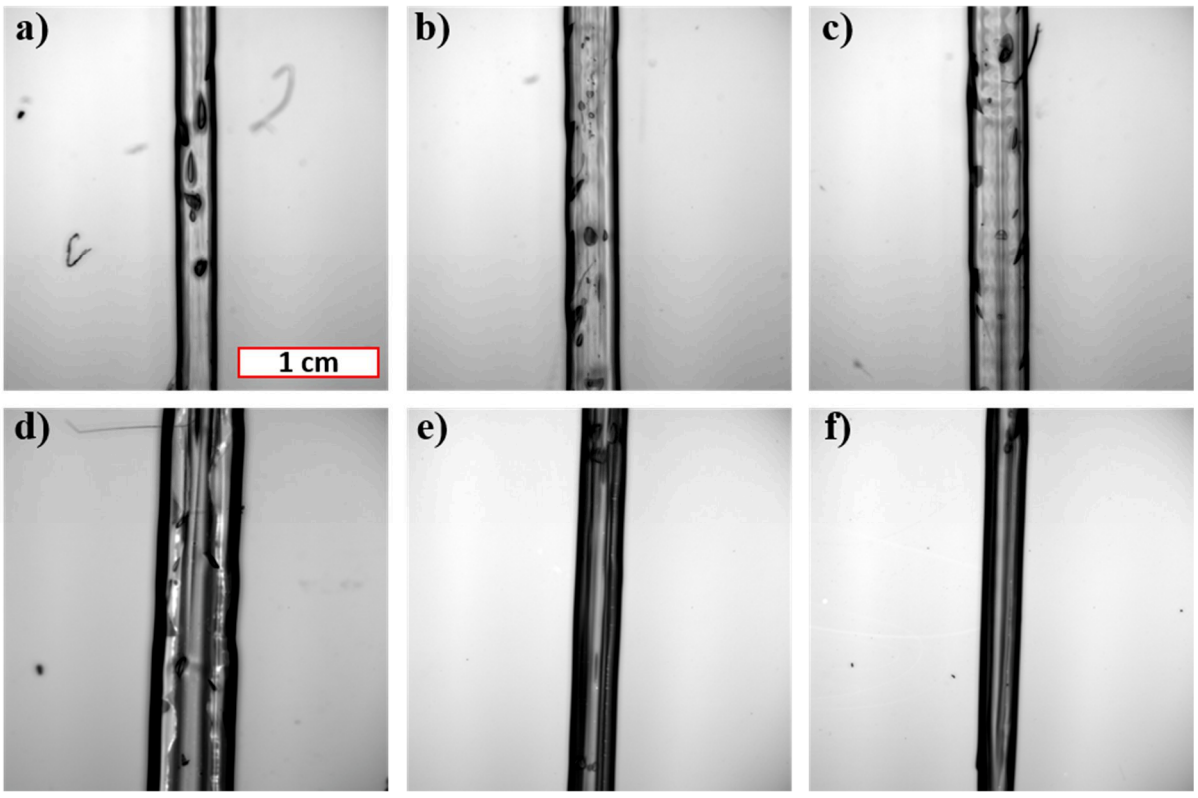



**Figure 3.1:** Optical microscope images of lines printed at 92.5 °C with a) 20, b) 30 and c) 40 kPa extrusion pressure. Optical microscope images of lines printed at 92.5 °C using 30 kPa pressure with d) 1, e) 5 and f) 7 mm/s printer head travel speed. Scale bar applies to all images.

Afterwards, we wanted to see the difference between unidirectional printing and bi-directional printing. In unidirectional printing, after finishing printing a line in one direction, the nozzle had to travel to start extruding again. In bidirectional printing, after the initial line is printed, the nozzle traveled in the perpendicular direction to start extruding the adjacent parallel line. According to the SEM images, bidirectional printing resulted in merged adjacent lines (Fig. 3.2a) while unidirectional printing ensured fully separate adjacent lines (Fig 3.2b). The poorly printed parts in Figure 3.2b was due to the delay between pressure application to the shellac and extrusion of the material. This is due to the elastic nature of molten shellac. The problem was solved by purging shellac for 0.25 seconds before nozzle starts moving to print the full line.

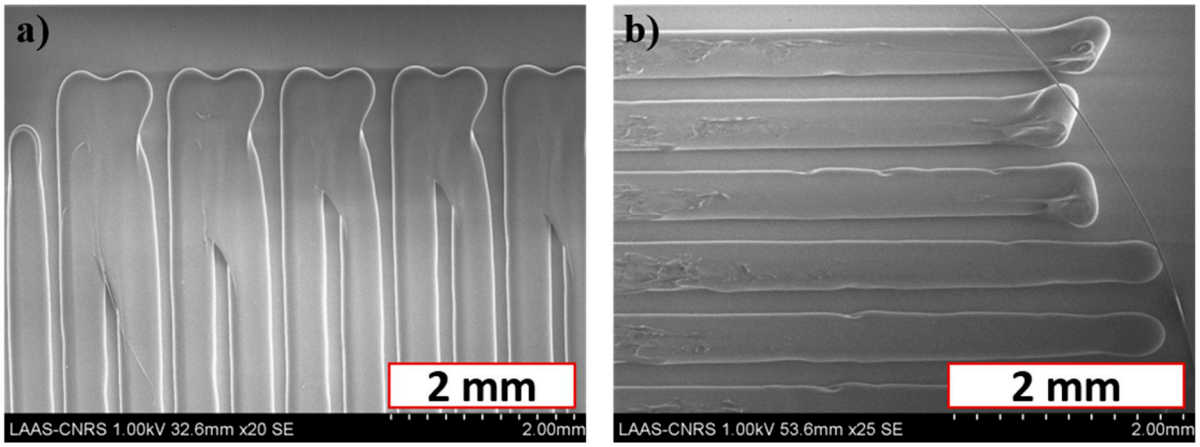



**Figure 3.2:** SEM images of adjacent lines in the grid structured first layer of design printed using a) bidirectional, b) unidirectional printing.

Finally, we printed 2 layers onto each other and took SEM images. We wanted to observe the possible drooping occurring on the overhangs second layer. Since we used a grid structure, lines in 2$^{nd}$ layers and above required to overhang between the adjacent lines beneath them (Fig. 3.3a, b). If the material viscosity is too low, these overhangs cannot support themselves and collapse (droop) (Fig. 3.3a). Moreover, we wanted to see the effect of different layer height because too low layer height would result in compression on every layer by the nozzle tip while printing the next layer. On the other hand, too high layer height would not even result in any printing since the extruded material could not reach the surface of the previous layer. Thus, we printed two layers for ach sample. We used 0.2 mm and 0.3 mm as the layer height for the first and 2$^{nd}$ sample, respectively. Results revealed that when we used 0.2 mm layer height, the lines in the 2$^{nd}$ layer were compressed during printing, Thus the thickness of lines in the second layer

increased at points in contact with the previous layer (Fig. 3.3c). On the other hand, no drooping or compression issue when 0.3 mm was used as layer height (Fig. 3.3d)

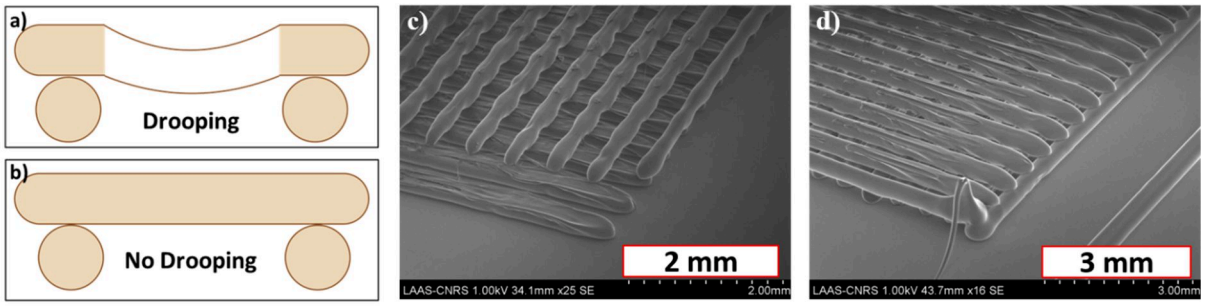



**Figure 3.3:** Schematic representation of a) drooping and b) non-drooping phenomena at the overhanging shellac lines. SEM images of 2 layers printed with using c) 0.2 and d) 0.3 mm as layer height.

The optimized parameters were 92.5 °C nozzle temperature, 30 kPa extrusion pressure and 5 mm/s travel speed of the nozzle during extrusion. Then, we obtained a cubic scaffold composed of layers stacked over each other. Each adjacent layer had lines perpendicular to the ones in neighboring layers (grid structure). Upon optimization of the printing parameters, we obtained lines with 0.3 mm thickness. Finally, we acquired 30, 40 and 50% porous gels by adjusting the distance between adjacent lines to 0.6, 0.45 and 0.3 mm, respectively (Fig. 3.4c-e). The porosity of the gel is calculated by first calculating the porosity of the scaffold. The size and weight of the produced scaffold are measured after printing to calculate the density of the scaffold. The porosity of the scaffold is then calculated from the ratio of obtained density to the density of shellac.

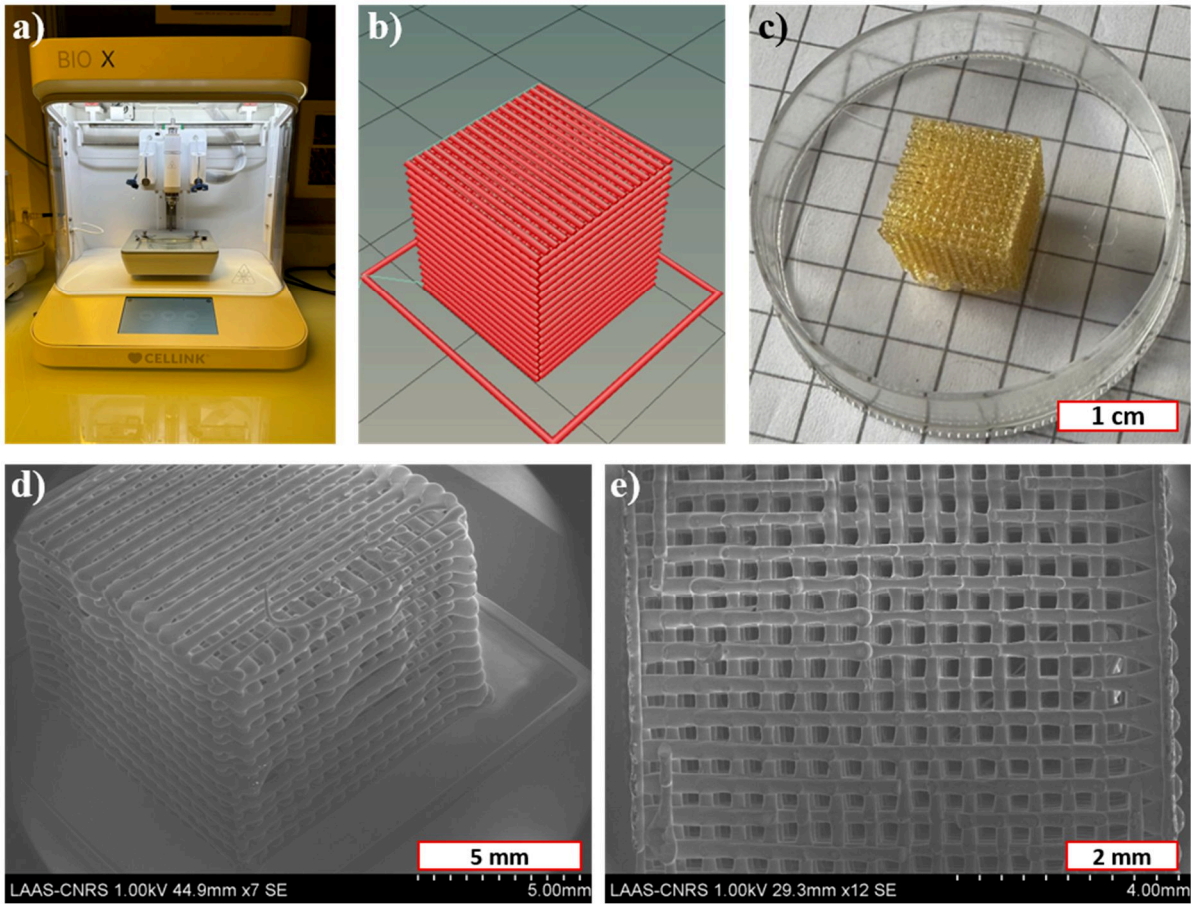



**Figure 3.4:** Images of the a) 3D printer BioX (Cellink), b) grid design of the scaffold on Heartware software, c) photograph of the printed shellack scaffold with 0.3 mm horizontal distance between adjacent lines, d, e) perspective and top SEM image of the same scaffold' respectively.

### 3.3. Development of Porous PNIPAM Hydrogel

After 3D printing the porous scaffold, we placed it inside a 5 ml Eppendorf. Then, we poured NIPAM solution with UV initiator into the Eppendorf until the scaffold was fully immersed. The same NIPAM solution is used as in previous section. Afterwards, we cut the tip of the Eppendorf and placed them in a desiccator for degassing. After 30 minutes of degassing under dynamic vacuum, we placed the gels under the UV lamp for 5 minutes. We cut the excess PNIPAM gel outside the shellac scaffold with a scalpel. Then we placed the samples in excess 0.5 M NaOH solutions and left overnight for selectively leaching the shellac scaffold. The gels are then rinsed with pure water several times to fully wash out the NaOH.

### 3.4. Unconstrained Swelling of Porous PNIPAM Hydrogel

To measure the swelling dynamic of the gel, we used similar technique as in Chapter 2. We shrunk the gels in hot water (~80 °C) and reswell in cold water (RT) while recoding images with the camera. We analyzed the images acquired with ImageJ software to obtain number of pixels corresponding to the area of the gel. Since we assumed fully isotropic volume change, we were able to calculate the corresponding thickness (x) data by taking the square root of the data corresponding to the area of the gel. From such data we were able to calculate the volume change with respect to time.

For this experiment, we optimized the design of the sample holder in order to acquire unconstrained swelling. In order to acquire unconstrained swelling, we 3D printed a sample holder (Fig. 3.5a). Then we glued the sample holder to the flat bottom of the glass crystallizing dish to prevent any movement during filling the dish with water. Afterwards, we stuck the cubic hydrogel sample (10x10x10 mm) to an acetate sheet which we also glued to the sample holder. Finally, we filled the crystallizing dish with hot/cold water and recorded the shrinking/re-swelling. This way the sample is only held in place from one surface allowing unconstrained shrinking/re-swelling (Fig. 3.5b, c).

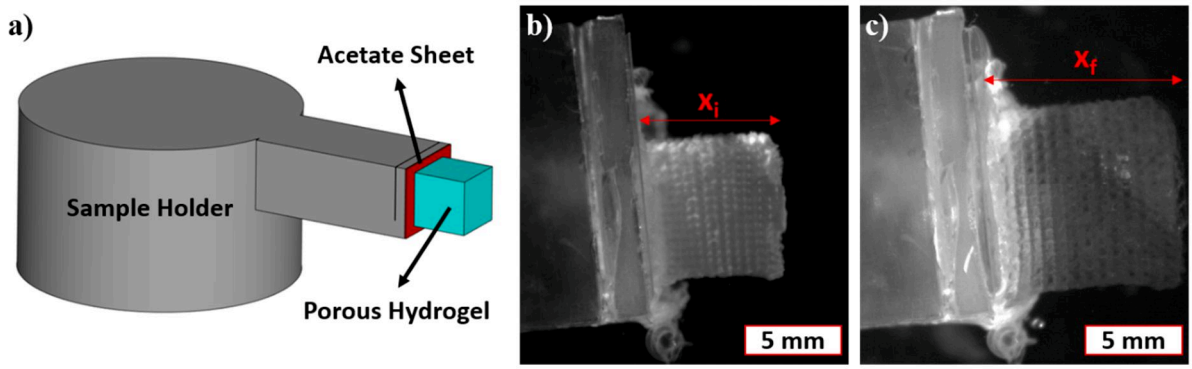



**Figure 3.5:** ) Schematic of the sample holder, images of the b) shrunk, c) swollen porous PNIPAM gel (50% v/v porous). $x_i$ represents the initial thickness of the gel while $x_f$ represents the final gel thickness.

### 3.5. Diffusion Coefficient of Water in the Porous Gel Matrix

We can compare the dynamics of swelling/shrinking of both HP-OR gel mentioned in the previous chapter and 3D printed porous gel. For this, we analyzed the swelling data obtained from both samples. Initially we plotted the change in thickness of the gel (Δx) against time (Fig. 3.6). We observed that the thickness of both of the gels change quite fast during swelling/shrinking owing to their microporous structure. On the other hand, the change was faster for HP-OR gel during both swelling and shrinking. As a result, HP-OR gel reached equilibrium much faster. This was due to higher level of porosity and more homogeneous pore structure of HP-OR gel. Moreover, 3D printed porous gel continued to increase in thickness when the thickness of HP-OR gel equilibrated. This was due to the slight difference in the total thickness of the samples in their natural state. The HP-OR gel had a thickness of 0.7 mm whereas 3D printed gel sample was 1.0 cm in thickness. Slightly higher thickness changes occurred during shrinking for both gels. This was because the initial volume of the gel was better captured in shrinking experiments. We first conducted the shrinking experiments. The gels shrunk down to the pseudo-equilibrium volumes. Then, we conducted the swelling experiments were the gel did not swell exactly to 100% of its initial volume but again the pseudo-equilibrium volumes. Thus, the change in thickness is slightly higher upon shrinking for both of the gels.

change in thickness accelerates quickly for both of the porous samples. The increase in thickness for the HP-OR gel plateaus faster than 3D printed porous gel. This is due to the higher level of porosity in HP-OR gel. On the other hand, increase in Δx continues further for the 3D printed porous gel because the tunnel shaped pores are bigger than the micro spherical pores in HP-OR. Thus, as the gel continues to swell, the bigger tunnel shaped pores continuous to expand and permit higher flux.

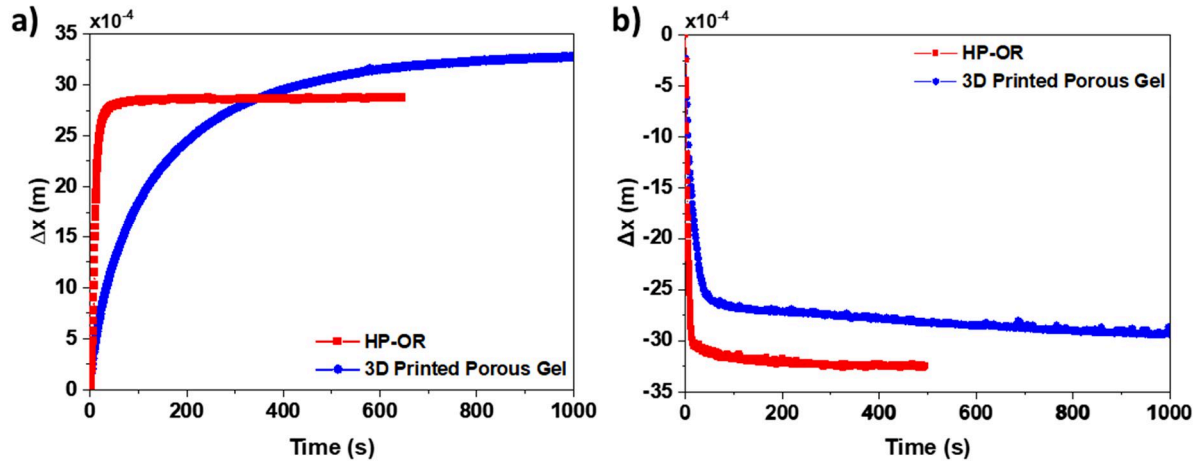



**Figure 3.6:** Graphs showing the change in gel thickness with time during a) swelling and b) shrinking of HP-OR (Red square) and 3D printed porous gel (blue circle).

To go further, we evaluated the water diffusion coefficient (D). We modeled the swelling dynamic of the gel based on the Biot's theory of poroelasticity as described in section 1.3.2. In such theory the gel is considered as homogeneous and in mechanical equilibrium. This means there is no stress applied on the gel in its initial state. The driving force for solvent diffusion inside the gel is the chemical potential difference between solvent inside and outside the gel. Moreover, the gel is taken to be in thermodynamic equilibrium which means that any change in free energy during swelling is due to the work done by stress and diffusion of solvent. Finally, assuming both the gel and solvent volumes are incompressible, we can say that the volume change is solely due to change in solvent concentration in the gel.

These assumptions, allow to obtain a direct relation between the applied stress, strain and difference in chemical potential of the solvents inside and outside the gel during swelling/shrinking. Moreover, the significant role of elastic modulus and the Poisson's ratio of the gel is shown in poroelastic behavior of gels during swelling/shrinking by Eq. 3.1,

$$\sigma_{ij} = 2G\left(\varepsilon_{ij} + \frac{\nu}{1-2\nu}\,\varepsilon_{kk}\delta_{ij}\right) - \frac{\mu-\mu_0}{\Omega}\delta_{ij} \qquad (3.1)$$

where σ represents the stress, ε strain, ν Poisson's ratio, Ω volume per solvent molecule, μ chemical potential of the solvent and G elastic modulus.

Using this relation, swelling of an unconstrained thin (100 μm) layer of PNIPAM gel was modeled in a study by Yoon et al. (2010). The gel was immersed in a solvent with certain chemical potential and it swelled freely in all three dimensions. Since there were no constraints on the gel volume, no stress occurred on the gel during swelling. At equilibrium, the chemical potential of the solvent inside the gel was equal to the chemical potential of the solvent outside. During the transient phase, the chemical potential of the solvent in the gel and both in plane/vertical strains where only time dependent variables. This means that the shape of the gel did not change during swelling since there was no constraints. With these parameters the free swelling of the gel could be explained by a partial differential equation but the instantaneous in plane deformation along with vertical strain (thickness change), made the numerical solution of such equation impossible. On the other hand, the numerical solution was achieved for constrained swelling and the experimental data on the unconstrained swelling revealed that the initial transient phase of swelling in both situations could be modeled by the relation;

$$\frac{\Delta(x)}{\Delta(\infty)} = \frac{2}{H}\sqrt{\frac{Dt}{\pi}} \tag{3.2}$$

where Δ(x) is the change in thickness of the gel, Δ(∞) is the maximum change in thickness at equilibrium, H is the initial gel thickness, t is the time and D is the diffusion constant of the solvent [2].

In our experiment, we freely swelled microporous gels without any external constraints. We assumed instantaneous temperature change upon immersion into hot/cold water. The chemical potential difference between solvents inside/outside was imposed by difference in temperatures. Gel shrink/swell due to the different hydrophilicity of PNIPAM molecules at temperatures above/below its LCST.

To obtain the diffusion coefficient using the relation in equation 3.2, we plotted Δ(x)/H as a function of √t/H (Fig. 3.7). We observed that the initial transient phase of swelling/shrinking was linear as predicted by the model. As shown in equation 3.2 the slope of these lines gave us the information on the diffusion coefficient of water through the microporous gel matrix during volume change.

From their respective slopes, diffusion coefficient of water through 60% porous gel was calculated to be $3.6x10^{-6}$ $m^2/s$ during both swelling and shrinking. This validates our results in the previous chapter. We were able to overcome the diffusion limited shrinking/swelling rate of the gel by introducing high porosity with PMMA scaffold.

On the other hand, 3D printed porous gel showed diffusion coefficient of $1.0x10^{-7}$ $m^2/s$ during swelling and $5.0x10^{-7}$ $m^2/s$ during shrinking. The diffusion coefficient was lower than the HP-OR gel. This was due to the lower porosity level of 3D printed porous gel. The difference between diffusion coefficients during shrinking and swelling was an indicator that there where non-porous volumes in 3D printed porous gel. The shrinking/swelling rate was still diffusion limited in these non-porous regions thus, swelling occurred slightly slower than shrinking.

According to the literature, diffusion coefficient of water through non-macroporous PNIPAM gel is in the range of $1\text{-}3x10^{-11}$ $m^2/s$ [2]. This means with PMMA scaffold induced macropores we obtained more than $10^5$x higher diffusion coefficients than bulk PNIPAM hydrogel thanks to macroporosity. Moreover, 50% porous gel produced with 3D printed shellac scaffold achieved more than ~$10^4$x higher diffusion coefficients than bulk PNIPAM hydrogel.

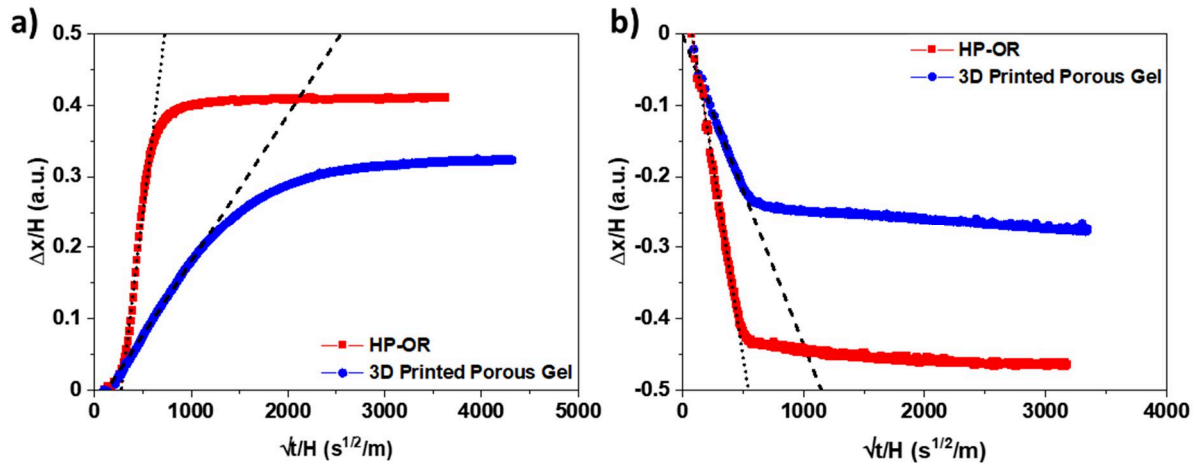



**Figure 3.7:** Swelling a) and shrinking b) curves of 60% porous HP-OR gel (red) and 50 vol% porous 3D printed gel (blue). The initial slope (transient region) gives information on the diffusion coefficient of water through the gel matrix during swelling. Black dotted and dashed lines represent linear fit to the transient stage of the curves of HP-OR and 3D printed porous gel, respectively.

## 3.6. Analysis of Poroelastic Gel Properties via Controlled Flow Experiment

### 3.6.1. Development of the Experimental Setup

We developed an experimental setup in which we could control the flow (inlet water pressure and temperature) of water exclusively through the macroporous gel matrix. Our aim was to obtain insight on the permeability of the hydrogel. Moreover, we also observed the direct effect of temperature on water diffusion through shrinking PNIPAM gel matrix.

We developed a gel container to be able to immobilize the gel during continuous flow of water. We 3D printed a two-part system which microfluidic connectors could directly fit (Fig. 3.8). The bottom part contained an inner groove for the gasket and the top part contained an additional second groove for a gasket between two halves of the container. This way, we prevented leakage either between the container and the gel and between two plastic parts. After placing the gel, two parts are put together by 8 screws.

Imposing a flow through the gel while letting the gel shrink/swell as freely as possible was challenging. To achieve this, we developed a special construction. We first polymerized PNIPAM in and around the cubic 3D printed shellac scaffold as explained (Section A.2.3). Then, we placed the scaffold/PNIPAM sample into a bigger cylindrical mold and polymerized a second layer of PNIPAM around. Since we needed to prevent any leakage during the experiment we had to press on the sample with gaskets. PNIPAM was too brittle and thus would break under such compression from gaskets. For this reason, we used a soft silicon (Ecoflex-0050 Smooth-On). We produced a doughnut shaped silicon sample holder and placed our scaffold/PNIPAM sample into the middle (Fig. 3.8a).

The main obstacle here was ensuring good adhesion between PNIPAM and silicone surfaces. The silicone elastomers do not favor bonding with acrylamides due to the oxygen inhibition effect. Thus, we used the method provided by Yuk et al. (2016), in which benzophenone is used to reactivate the silicone molecules for covalent crosslinking [3]. We rinsed the pre-polymerized silicone doughnuts with 10 wt.% benzophenone in ethanol solution and placed the disc shaped PNIPAM gels with shellac scaffold to the hole in the middle. Then, more NIPAM solution with UV initiator is poured and polymerized in between PNIPAM and silicone surfaces to act as glue. In the end, the disc shaped concentric PNIPAM/silicone gel is immersed into 0.5 M NaOH solution to leach the shellac out. After rinsing with excess pure water, the disc shaped gel is placed at the middle of the 3D printed container (Fig. 3.8b).

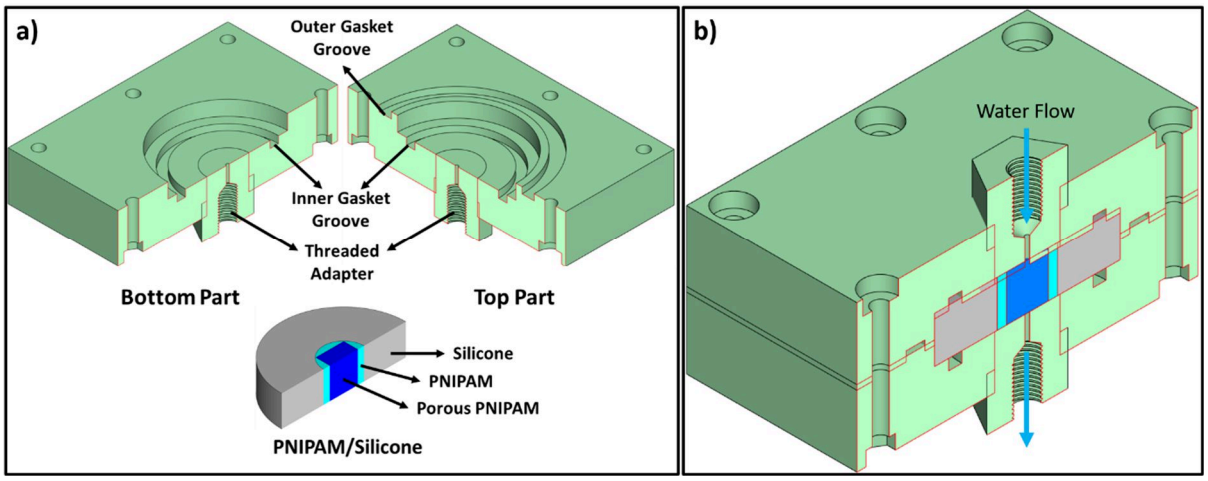



**Figure 3.8:** Schematic of the a) gel container and the disc shaped gel sample, b) cross-section of the assembled gel container system with sample inside.

In order to control the flow, we used a pressure controller (Fluigent) and connected the two pressure outlets to hot (80 °C) and cold (RT) water reservoirs. An electronically controlled valve is used to control the flow from two inlet water reservoirs to the system. In order to acquire the pressure gradient, a pressure sensor (Honeywell- 100MDSA3) is connected before and after the gel. Additionally, two thermocouples are placed before and after the gel container to observe the temperature of the passing water. Finally, a flow meter (Fluigent) is placed on the outlet of the gel container (Fig. 3.9).

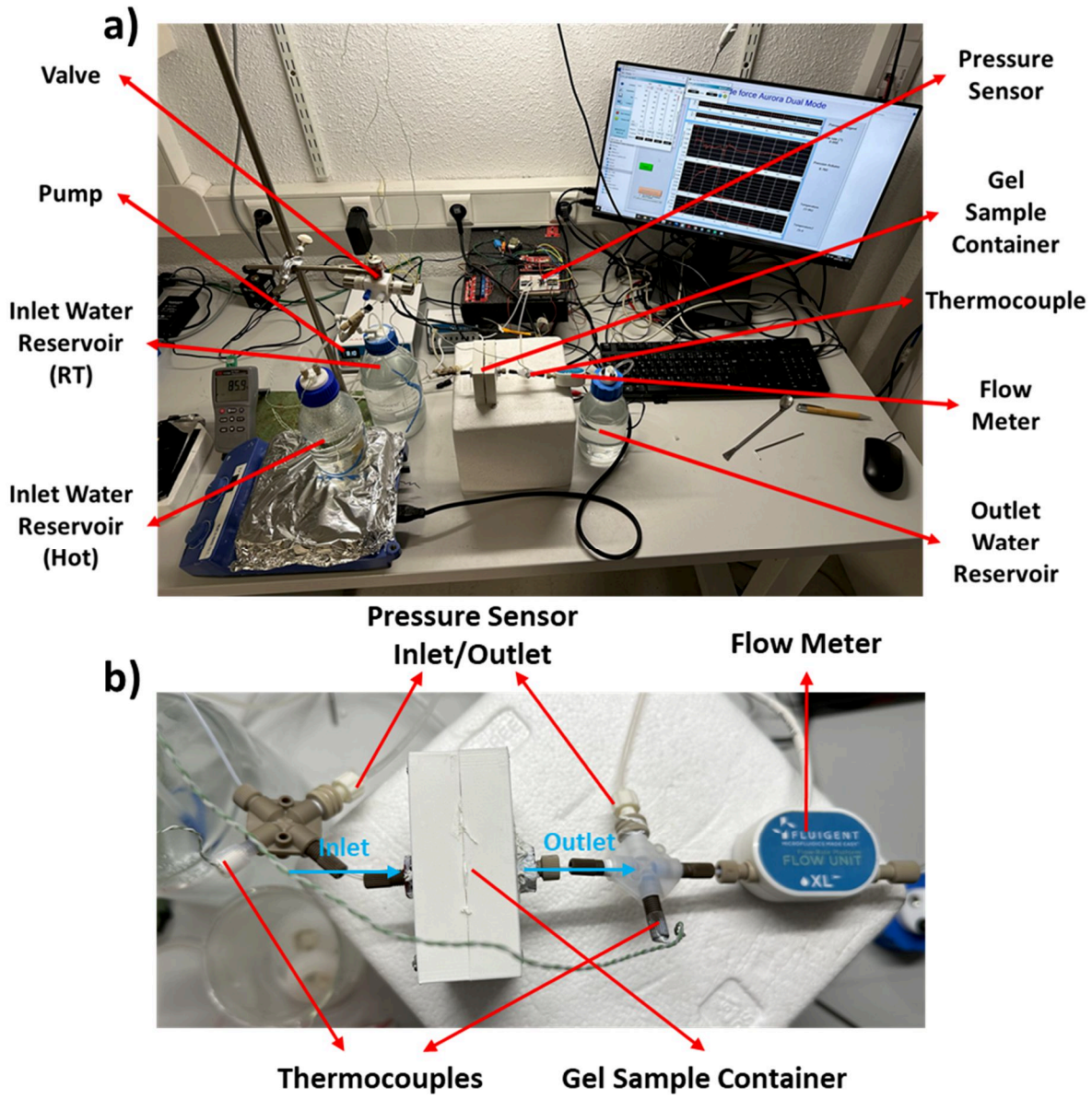



**Figure 3.9:** a) Experimental setup for controlled flow of water through porous gel sample. b) A zoom in top view of the gel sample container and sensors used.

### 3.6.2. Characterization of Hydrogel Permeability

Our first aim for constructing such controlled flow was to obtain the permeability data of the macroporous gel sample. We applied pressure sweep tests in which we started from high pressure and gradually decreased/increased the applied pressure to the inlet flow. After each step we waited about 1 minute for equilibration. We then increased/decreased the pressure.

From the evolution of flow rate with respect to pressure difference we observed two distinct behavior (Fig. 3.10). At low pressure differences, we observed that the flow rate evolves linearly with the pressure difference. For pressure differences above ~2500 Pa (25 mbar) the flow rate saturates at a maximum value.

The linear behavior at low pressure is in good agreement with the Darcy's law which states that the flow rate is directly related to the pressure gradient, viscosity of water and permeability of the gel matrix (defined as $k=\mu LQ/S\Delta P$ where $\mu$ is the water viscosity, L and S are the length and section of the gel sample, respectively) [2,4]. From the slope of the pressure difference across the porous gel and the flow rate (Fig. 3.10), we were able to calculate the permeability of our 50% porous gel as $2.7 \times 10^{-11}$ $m^2$.

We can compare this permeability value of 3D printed porous gel with 60% porous PAAc gel produced with the same PMMA scaffolding method in our team. According to the measurements previously done by our team, the swollen 60% macroporous PAAc gel showed a permeability value of $2 \times 10^{-12}$ $m^2$ at the swollen state [4]. Despite the lower porosity level (50%), we observe an order of magnitude higher permeability value in the current study. Such difference in permeability is attributed to the bigger, interconnected and tunnel shaped pores parallel to the flow direction. Such factors provide less resistance to flow enabling easier liquid transport.

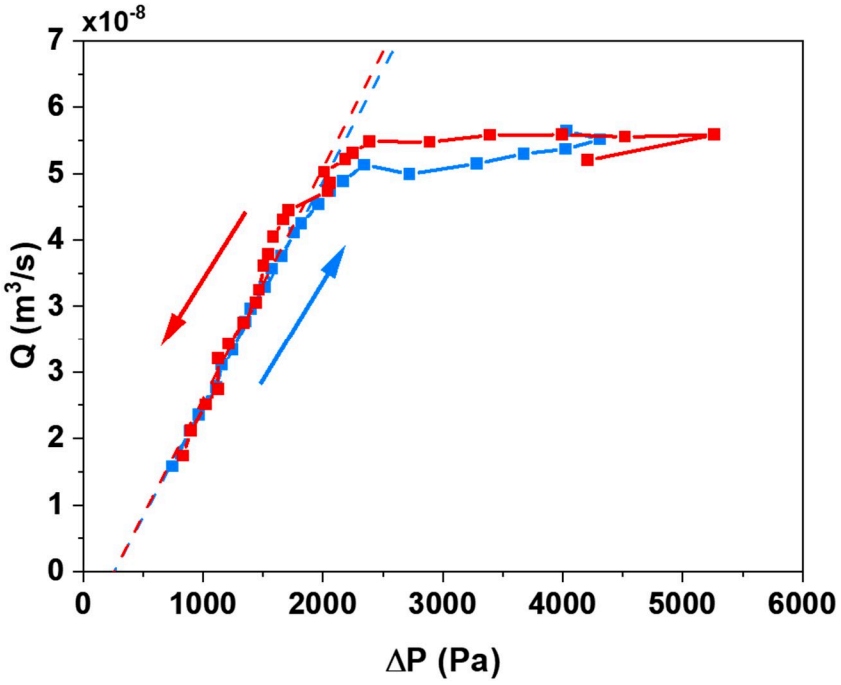



**Figure 3.10:** Graph depicting the change of flow rate of water (Q) with respect to the increasing (blue) and decreasing (red) pressure difference (ΔP) between inlet and outlet of the gel at RT. The dotted lines correspond to the linear fit applied at the data low pressure difference (<2500 Pa) region.

### 3.6.3. Poroelasticity of the Gel

The flow rate plateau observed at high pressure differences (Fig. 3.10) is because with the applied fluid pressure on the inlet ($P(0, t) = P_A$), the poroelastic gel matrix deforms in the direction of the flow. After certain pressure difference (>2500Pa) the outlet surface (x=H) of the gel starts to lean on the container surface. Thus, gel starts to experience compressive forces between the applied fluid pressure and the outlet gel container surface while flow is strictly restricted in the gel (Fig. 3.11). This is also in agreement with the lower permeability values upon lower slope at the plateau.

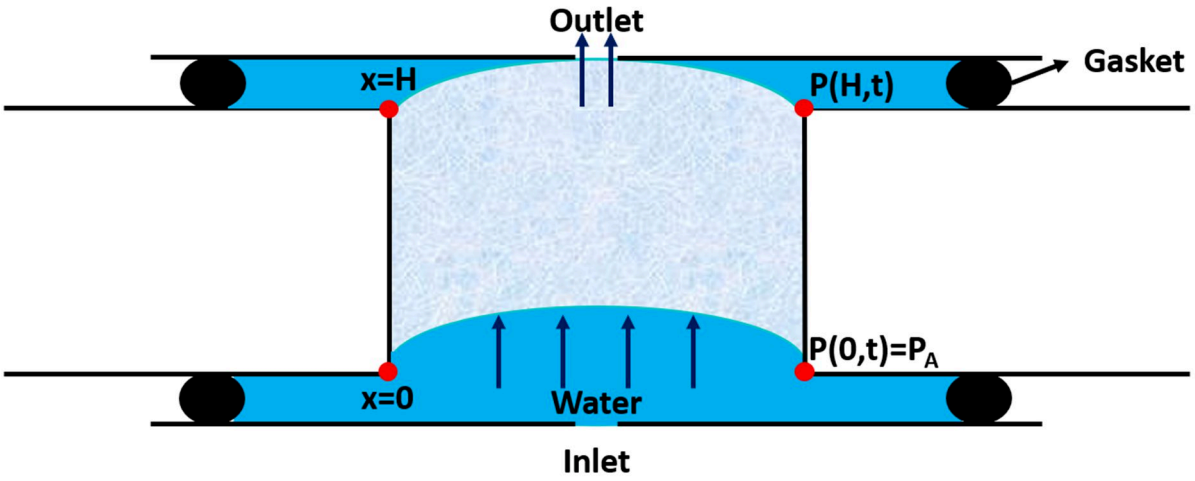



**Figure 3.11:** Schematic of the gel compression against the outlet gel container wall upon high applied pressure ($P_A$) on the inlet.

Such phenomena can be better explained by the linear poroelasticity theory [5]. In our case the fluid and solid displacements are unidirectional and permeation flow can be correlated to the pressure gradient across the gel by Darcy's law as;

$$W = -\frac{\kappa}{\mu}\frac{\delta P}{\delta x} \tag{3.3}$$

where W is the permeation flow, κ is the permeability of the porous gel, μ is the fluid viscosity, P(x, t) is the pressure field and x is the distance from inlet (x = 0) to outlet (x =H) surface of the gel. Given that the fluid/solid are incompressible and we have a continuous flow across the porous gel matrix, the mechanical equilibrium can be expressed as;

$$M\frac{\delta^2 U}{\delta x^2} = \frac{\delta P}{\delta x} = \frac{-\Delta P}{H} \tag{3.4}$$

Where M is the elastic modulus of the porous gel and U(x ,t) is the displacement field of the solid. Our gel had thickness (H) of $1x10^{-2}$ m. Integrating the equation over the gel volume by assuming constant gel applied pressure at the inlet ($P_A$) and no change is displacement field at the inlet ($\delta U/\delta x = 0$ when $x = 0$), we acquire the relation between displacement field and pressure field throughout the gel as in equation

$$\Delta U = \frac{\Delta P}{2MH}(H^2 - x^2) \tag{3.5}$$

When we plot this equation at the point where fluid flow starts to give a plateau upon increasing pressure difference (the point compression of the gel against container surface starts), we obtain the graph in Figure 3.12. The anisotropic displacement of the poroelastic gel upon compression can be better understood as the maximum solid deformation occurred at the inlet surface of the gel (x = 0) which corresponds to more than 30% of the total gel thickness.

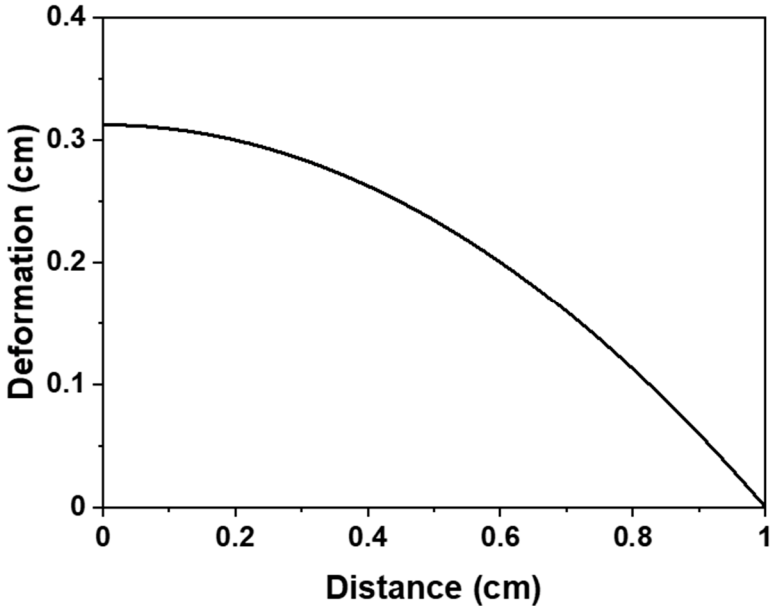



**Figure 3.12:** Graph showing the solid displacement along the gel when compression started to occur at 2500 Pa pressure difference.

### 3.6.4. Flow Dynamics Upon Temperature Change

After this, we conducted a temperature sweep test while keeping the inlet pressure constant to observe the change in fluid flow and pressure gradient. After reaching equilibrium at certain pressure we started flowing hot water (80 °C) at the same pressure. We then recorded the evolution of temperature at the inlet/outlet of the gel (Fig. 3.13a). We observed that the inlet temperature reached 34 °C after 6s we started pumping the hot water. Whereas the outlet water temperature only reached the same value after 40s. On the other hand, the increase in pressure difference and decrease in flow rate upon shrinking occurred simultaneously 20s after pumping hot water (Fig 3.13b, c). This is due to the shrinking of the PNIPAM gel resulting collapsing of the pores and limiting fluid flow. As a result, pressure difference between inlet and outlet of the gel increases.

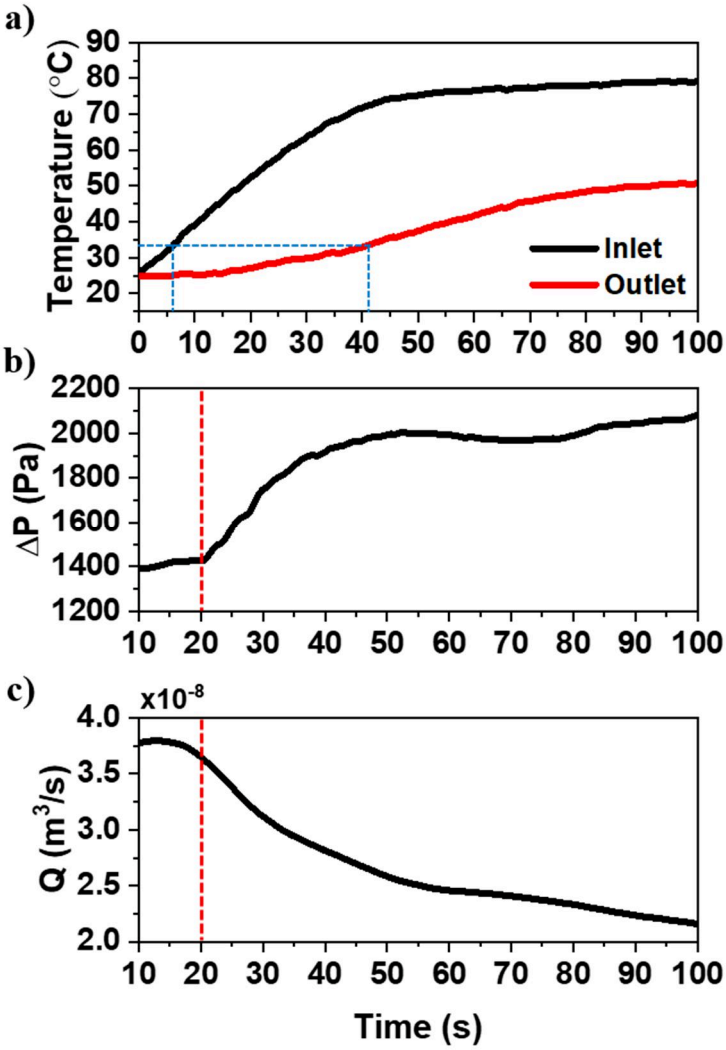



**Figure 3.13:** Graphs depicting evolution of a) inlet/outlet temperature, b) pressure difference and c) flow rate of water through the gel with time upon introducing hot water (80 °C) to the system. The blue dotted line represents the moment temperature reached 34 °C (LCST) whereas the red dotted line represents the instant effect of shrinking gel started to occur on pressure gradient and fluid flow rate through the gel.

### 3.7. Conclusion

In this chapter we aimed to reveal the effect of macroporosity on the poroelastic properties of PNIPAM hydrogels. No matter the type of trigger, hydrogel actuators ultimately rely on diffusion of water for volume changes. Moreover, introduction of macroporosity has proved itself to be a very efficient way to accelerate volume change rates upon faster water diffusion. Thus, it is important to identify the direct effect of porosity levels on poroelastic properties of hydrogels.

For this reason, we first developed a novel scaffolding method to better control the porosity levels in gels. By melt extrusion printing (3D) shellac, we were not only able to impose controlled porosity levels but also pore geometries. Moreover, since shellac can be dissolved at high pH aqueous solutions, the leaching process had no abrasive effect on the gel matrix.

Here we identified and compared the diffusion coefficient of water through 60% and 50% macroporous gels during free welling. We utilized the Biot's theory of linear poroelasticity to analyze the free swelling of macroporus PNIPAM. This way we were able to see not only the effect of porosity levels but the geometry of the pores on the unconstrained gel swelling kinetics. It is revealed that highly interconnected microspherical pores contributed to much faster (~$10^5$x) water diffusion compared to regular PNIPAM gel (mesoporous).

Moreover, we developed an experimental setup to analyze the flow of water through macroporous hydrogel under controlled conditions. Since the flow through porous gel is in agreement with Darcy's law, we were able to calculate the permeability of our porous gel. Here we observed that the permeability of fully swollen 50% porous PNIPAM gel was an order of magnitude higher than the 60% microspherical porous PAAc gel. This is attributed to the fact that the tunnel shaped pores parallel to the flow direction further lowered the resistance due to the gel matrix.

Upon realizing the plateau in flow rate over certain pressure difference and the resulting sudden decrease in permeability revealed that we exerted compressive forces over certain value. We observed that over 2.5 kPa pressure difference, the gel started to lean against the outlet surface and deform. With the linear theory of poroelasticity we determined that over 30% deformation occurred as soon as pressure difference exceeded 2.5 kPa.

Finally, by utilizing the same setup, we observed the change in flow kinetics through the gel upon increasing the fluid temperature over the LCST of PNIPAM. The gel eventually

shrunk and the flow rate decreased while pressure gradient along the gel increased upon shrinking. This was due to the collapsing pores increasing the resistance to fluid flow. We could not observe the permeability of the gel upon fully shrinking since cracks at the interface of PNIPAM and silicone occurred which allowed free flow.

This study enabled us to obtain insight on the flow kinetics through gel with different pore geometries and porosity levels which is crucial in development of hydrogel actuators with faster actuation ratios and higher actuation amplitudes. Additionally, with our novel scaffolding method, we opened a way to implement engineered pore geometries and porosity levels inside hydrogels enabling faster water diffusion.

### 3.8. References


[1] N. Thombare, S. Kumar, U. Kumari, P. Sakare, R.K. Yogi, N. Prasad, K.K. Sharma, Shellac as a multifunctional biopolymer: A review on properties, applications and future potential, Int. J. Biol. Macromol. 215 (2022) 203–223. https://doi.org/10.1016/j.ijbiomac.2022.06.090.

[2] J. Yoon, S. Cai, Z. Suo, R.C. Hayward, Poroelastic swelling kinetics of thin hydrogel layers: Comparison of theory and experiment, Soft Matter. 6 (2010) 6004–6012. https://doi.org/10.1039/c0sm00434k.

[3] H. Yuk, T. Zhang, G.A. Parada, X. Liu, X. Zhao, Skin-inspired hydrogel-elastomer hybrids with robust interfaces and functional microstructures, Nat. Commun. 7 (2016) 1–11. https://doi.org/10.1038/ncomms12028.

[4] V. Mansard, A macroporous smart gel based on a pH-sensitive polyacrylic polymer for the development of large size artificial muscles with linear contraction, Soft Matter. 17 (2021) 9644–9652. https://doi.org/10.1039/d1sm01078f.

[5] 2† Jean Cacheux,1,2 Jose Ordonez-Miranda,1,2 Aurélien Bancaud,1,2,3* Laurent Jalabert,1,2 Masahiro Nomura,1,2 Yukiko T. Matsunaga1, Asymmetry of tensile vs. compressive elasticity and permeability contributes to the regulation of exchanges in collagen gels, (n.d.) 1–19.

## 4. Development of an Electroactive PAAc/PEDOT:PSS Hydrogel Actuator

In this chapter, we demonstrate the studies conducted to develop a chemically active and electrically controllable hydrogel actuator. In order to achieve such purpose, there are several properties required from the hydrogel. These properties are chemical sensitivity, electronic conductivity and reversible actuation. Moreover, proper working conditions for the hydrogel should be investigated to achieve efficient and reversible actuation. PAAc is known to be chemically sensitive towards metallic ions such as $Cu^{2+}$ or $Ag^{+}$, The AAc molecules are known to form complexes with these metallic ions and shrink. Hence, we used PAAc as our chemically sensitive hydrogel throughout the study. Electronic conductivity was required from the hydrogel in order to be able to trigger actuation with electricity. Thus, our initial step towards developing such material was to introduce conductivity to the hydrogel matrix. We aimed to utilize an intrinsically conductive gel PEDOT:PSS and obtain a double network hydrogel system in which electricity could travel through the conductive secondary network. In the first section of this chapter we demonstrate three different strategies to acquire a double network hydrogel. These methods are polymerizing either EDOT/AAc monomers inside the chemically crosslinked counter gel and polymerizing AAc monomers inside physically crosslinked PEDOT:PSS gel matrix. After achieving electronic conductivity ($\geq 10^{-3}$ $S.cm^{-1}$) in the double network hydrogel, in the second part of this chapter we investigated its electrochemical properties such as capacitance to reveal the efficiency of ion transfer in/out upon electrical trigger. Finally, we investigated the complexation efficiency and reversibility upon introduction of $Cu^{2+}$ ions to PAAc hydrogel. The key aspect was to determine the amount of metallic ion required to acquire significant reversible actuation. Thus, we observed the shrinking/re-swelling dynamics of PAAc gel upon introduction of different ion concentrations and the changes in solution pH/conductivity after complexation. Nevertheless, for more elaborative results such as the critical ion concentration required for full shrinking of the PAAc gel we used complexometric spectrophotometry method.

## 4.1. Introduction

Physiological muscles in our bodies are chemically active and the contraction/extension mechanism is triggered by the electrical signals coming through neurons. Thus, here we aimed to mimic such system by utilizing a chemically active hydrogel and introduce electronic conductivity for precise triggering mechanism with electricity.

In order to obtain such artificial muscle material, we used PAAc as our chemically sensitive hydrogel material. The PAAc gel has been known to form complexes with metallic cations such as $Cu^{2+}$ and $Ag^{+}$ via electrostatic forces. As a result, at certain metallic ion concentrations, PAAc hydrogel undergoes volume phase transition due to inter chain links formed via complexations between carboxyl groups of the AAc molecules and metal ions [1]. Such property was previously utilized in studies for development of soft actuators [2–4].

Takada et al. (2005) is the only study which explore gel sensitivity to electrochemistry. In this study they produce a bimorph actuator from thin PAAc gel films [4]. Bimorph actuator is a cantilever constructed from two active layers. PAAc gel films were used as the active layers and a polyimide (PI) passive layer was used in between active ones. The cantilever was dipped into an electrolyte solution containing copper cations. Upon introduction of positive voltage to the PAAc layers, they undergone oxidation and complexed with copper ions. Such phenomena resulted in contraction of the PAAc films. The passive PI layer was intended to force the cantilever to bending motion upon contraction of the active layers. They realized that full contraction could be achieved when +0.5 V was applied and the straight form could be recovered when the copper ions were reduced back to its initial state upon introduction of -0.7 V. This proved the system was working as an electrochemical actuator.

Nevertheless, there were also several problems with the actuation system developed by Takada and his colleagues. First of all, they found that the diffusion coefficient of copper ions in the shrunk gel was 6000x lower than in the solution which results in lower actuation rates. Such slow diffusion in the gel is due to the electrostatic interaction of ions with the AAc molecules. This slow diffusion cannot be compensated by applying higher potentials to accelerate the ion diffusion.

Secondly, they realized that upon several oxidation/reduction cycles, the actuator displacement (stroke) significantly decreased. This was either due to the leakage of copper ions from the gel, inactivation of the ions on the gel or peeling of the gel from the electrode. Lastly,

it was observed that only 1/3 of the carboxy groups of PAAc molecules were complexed with copper ions in the shrunk state when the ion concentration was in excess. This was also thought to be due to the steric hindrance or competition between cations from copper and the electrolyte [4].

In order to overcome such disadvantages, our first strategy was to introduce electronic conductivity to the hydrogel. Electronic conductivity ($>10^{-2}$ $S.cm^{-1}$) would ensure more homogeneous and faster electron transfer throughout the gel matrix upon applied voltage. As a result, both the efficiency and the rate of copper reduction/oxidation could be enhanced.

Electronic conductivity can be implemented to a hydrogel in two main strategies. First one is incorporation of conductive nano/micro additives such as metallic particles, carbon black, carbon nanotubes etc. Since this method requires incorporation of solid particles, the elasticity and more importantly permeability of the gel matrix are reduced significantly. The solid additive particles act as barriers in front of the fluid flow. This in turn affects the actuation rate/ratio of the hydrogel negatively.

The second strategy is incorporation of a second polymer network which is intrinsically conductive in the system. This way, electrons can be conducted from the second network while acting as a toughening agent. More importantly, since both networks are elastic gels, the actuation rate and ratio are affected in a smaller scale. In our study, we utilized PEDOT:PSS as our conductive second polymer network.

### 4.2. Conductive Gel

PEDOT is a highly conductive conjugated polymer but it is generally used in the form of thin films. This is due to the high hydrophobicity of the PEDOT molecules. Hydrophilic dopant such as PSS is required to stabilize it in aqueous solutions. Even with doped PEDOT (PEDOT:PSS), stable aqueous suspensions with only very low solid content (~1 wt.%) can be obtained due to the low hydrophilicity. Such low mass percentage has not been a problem for production of highly conductive (~1000 S/cm) thin films (<100 μm thickness) via spin-coating or blade casting methods but it poses a serious problem in production of mm scale hydrogel matrices.

On the other side, producing large conducting samples based on conductive polymer is much more challenging. Recently in the literature, few studies have been published on production of electronically conductive gels. They are either based on polymerizing a second network of conductive polymer into an initial gel network [5] or producing a gel network into an already polymerized suspension conductive polymer [6]. In this work, we explore three strategies which are inspired from the literature. Our work emphasize the challenge for the production of electronically conductive gel.

**Strategy #1:** Initially, following the study by Naficy et al. (2012) we impregnated PAAc gels with EDOT/NaPSS solution and polymerized. The aim was to fully cover the PAAc matrix with PEDOT:PSS molecules and achieve conductive paths throughout the network. For this, we also investigated the effect of different EDOT, PSS and initiator concentrations on the final DN gel conductivity. We only observed ionic conductivity in these gels since conductive network was not dense enough to form permanent conduction paths.

**Strategy #2:** Our second strategy was to utilize the commercial PEDOT:PSS dispersion. We incorporated the suspension directly into the AAc monomer solution prior to polymerization. This method was very limiting in terms of final PEDOT:PSS amount in the DN gel structure because of the low concentration of the commercial dispersion (1.15 wt.%). Nevertheless, we were able to obtain final PEDOT:PSS concentrations of 0.1, 0.25 and 0.5 wt.%. Moreover, we also investigated the effect of physically crosslinked gel network by utilizing agarose as the first gel network. Unfortunately, we observed only ionic conductivity in these gels due to the similar reasons.

**Strategy #3:** Our last strategy for producing conductive DN gel was through gellification of PEDOT:PSS dispersion. We have searched the literature for better incorporation of PEDO:PSS molecules in the gel matrix to preserve the electronic conductivity in the double network structure. We first came across the study by Feig et al. (2018). In this study, PEDOT:PSS/PAAc double network gels were produced by first gellification of the commercial PEDOT:PSS dispersion. A highly ionic liquid 4-(3-butyl-1-imidazolio)-1-butanesulfonic acid triflate was added to the dispersion in order to de-dope the PSS reagents off and collapse conductive PEDOT molecules on each other. The entanglement of the highly hydrophobic PEDOT chains would increase and act as a physical crosslink. This way, conductivity values over $10^{-1}$ S/cm were achieved [6].

In the study by Yao et al. (2017), the same principal was used for inducing gelation on the PEDOT:PSS dispersion. This time sulfuric acid ($H_2SO_4$) was added (0.1 M) to the dispersion and heated up to 90°C for 3h to de-dope the PEDOT. In this study, no double network was developed. The PEDOT:PSS hydrogels were produced in the form of fibers and dried. As a result, highly conductive and porous material was developed. Conductivity of 8.8 S/cm was achieved [7].

We used sulphuric acid ($H_2SO_4$) as the de-doping agent at elevated temperatures (75 °C) to gellify PEDOT:PSS. Hence, we achieved a physically crosslinked PEDOT:PSS network which we later impregnated with AAc monomer solution and polymerized to acquire a DN hydrogel. These gels showed high electronic conductivity ($>>10^{-2}$ S.cm$^{-1}$) assuring presence of conductive paths inside the DN matrix.

## 4.3. Development of Conductive Double Network Gels

### 4.3.1. Strategy #1: Impregnation of EDOT Monomers into PAAc Gel

The strategy #1 replicate the work of Naficy et al (2012) [5]. It starts with samples of pre-polymerized PAAc which are dipped into EDOT monomer solutions to impregnate them. Afterwards, the initiator (APS) was introduced to the same pot to induce PEDOT:PSS polymerization and cover all PAAc surfaces. In the study, they report a single concentration of monomer and initiator which are used in excess to ensure full polymerization. In this work, we screened different concentrations and different polymerization processes.

Adding APS directly into the solution induces rapid polymerization of PEDOT. The gel turns black indicating formation of PEDOT:PSS. Nevertheless, polymerization also occurs around the gel since both monomer (EDOT) and initiator (APS) are both present in the surrounding solution. Therefore, at the end of the experiment, the gel sample is trapped in a black bulk of PEDOT:PSS matrix and needs to be separated. Due to the highly brittle nature of PEDOT:PSS, separating the sample without causing any cracks is problematic.

To overcome such problem, we considered another method for initiating polymerization. The gel sample is first impregnated with EDOT solution for 5 days. Then, we removed the gel sample from the EDOT solution and quickly dried with a tissue to get rid of the excess monomers around the gel. We then dipped the EDOT solution impregnated gel into an APS solution for 3 days. Polymerization was initiated by diffusion of APS through the gel matrix.

Moreover, we tried different EDOT and APS concentrations. The formulations of different samples are presented in Table 4.1. The resulting solutions, gel samples and their respective conductivities can be seen in Figure 4.2. The details of the method can be found in the appendix (A.4.1).

**Table 4.1:** Samples for EDOT:PSS polymerization inside pre-polymerized PAAc matrix.

| | EDOT/NaPSS Dispersion Concentration | APS Solution Concentration | APS Added Directly | Gels Immersed in Separate APS Solution |
|---|---|---|---|---|
| Sample 1 | Reference | Reference | ✓ | |
| Sample 2 | 5x Dilution | 5x Less | ✓ | |
| Sample 3 | Reference | Reference | | ✓ |
| Sample 4 | 5x Dilution | 5x Dilution | | ✓ |

We measured the conductivity of the gel by using a 4 point-probe method. Briefly, we placed the gel samples between two glass slides with 4 copper stripes acting as electrodes (Fig. 4.1). We then apply DC current sweeps up to 1mA (0.1 mA steps) between two outer electrodes and we measured the voltage between the two inner electrodes. We calculated the conductivity of the gels with the help of Ohm's law. The details of the method can be found in appendix (A.4.2).

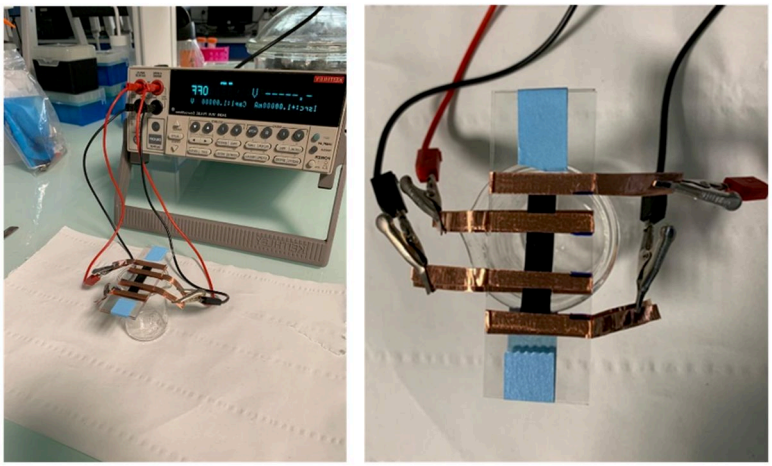


**Figure 4.1 :** Images of the 4-point probe setup. The gel is sandwiched between two glass slides with symmetrical copper tapes. The probes are attached to the sourcemeter with alligator clips.

Gel samples from direct addition of APS appear to have darker color than the samples produced by separate immersion onto APS solutions (Fig. 4.2a). This indicates that a much higher PEDOT:PSS concentrations in sample 1 and 2. Nevertheless, measurements show that all samples have a very low conductivity of about 1-5x$10^{-3}$ S/cm. Similar conductivity values have been measured by Naficy et al. Such conductivity value is only 10x higher than the one

measured for pure PAAc gel which only possess ionic conductivity and no electronic conductivity.

Several studies report that the conductivity range of $10^{-4}$-$10^{-2}$ S/cm is due to the ionic conduction [8,9]. We believe these values are due to the artifacts of the monomer solutions in the gels acting as ionically conducting electrolytes. To confirm this, we dried the gels and the measured conductivity decreased upon losing the solvent. This is due to the loss of ion mobility upon loss of liquid media. If conduction was by electron transfer from adjacent atoms in the polymer molecules, the conductivity would increase upon drying such as the conductive polymer concentration and the percolation.

Hereon, we will aim conductivity values higher than $10^{-2}$ S/cm. We will consider the conductivity below this value as only an artifact due to ionic conductivity. It indicates that the concentration of the conductive polymer is not sufficient for actuation.

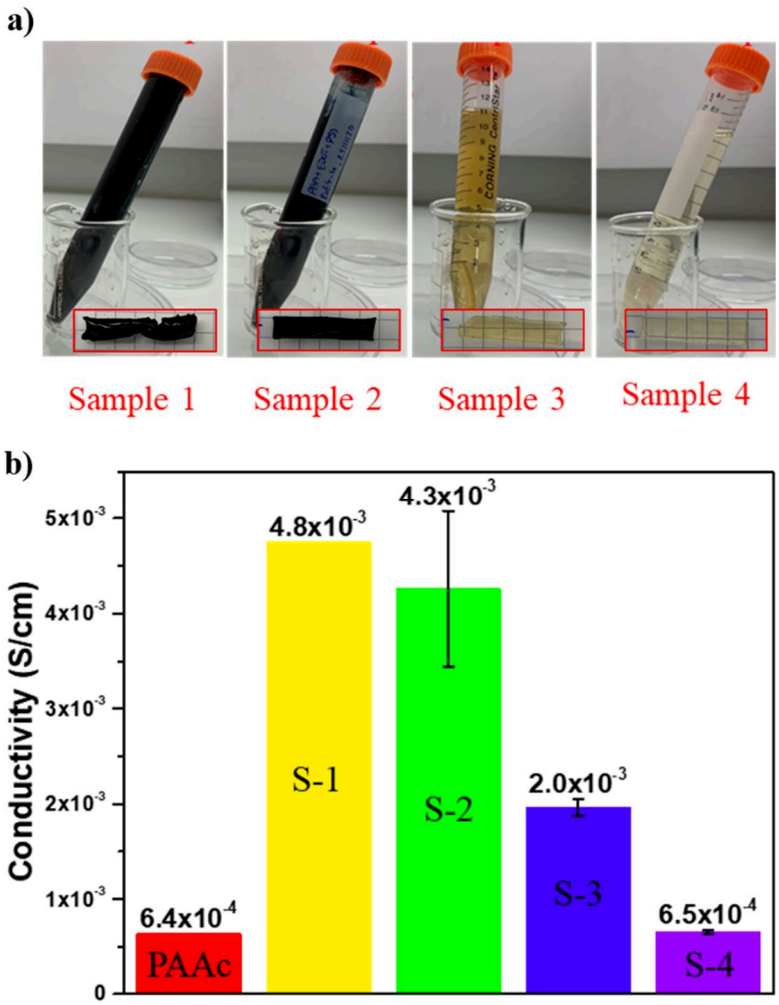



**Figure 4.2 :** a) Images of the EDOT/NaPSS dispersions with different concentrations and polymerization conditions. b) Conductivity values of neat PAAc gel (red) and PAAc/PEDOT:PSS gels with standard dispersion and direct APS addition (Sample 1, yellow), diluted dispersion and direct APS addition (Sample 2, green), standard dispersion and separate APS solution (Sample 3, blue), dilute dispersion and separate dilute APS solution (Sample 4, purple).

In order to better visualize the EDOT penetration through the PAAc matrix, we dried and froze the gels. After cutting, we conducted both SEM and energy-dispersive x-ray spectroscopy (EDX) analysis on the cross-sections of the samples. With EDX analysis we looked for the traces of sulfur atoms coming from the PSS since AAc molecules do not contain the same element. We took carbon, oxygen, potassium and sulphur atoms into account in conducting EDX analysis.

Since EDX analysis is done locally, it may not give qualitatively comparable results between different samples if no control sample is used for calibration. Nevertheless, corresponding sulfur atom concentrations were higher in dark colored samples and lower in light colored samples giving rough idea about the abundance of sulfur atoms in the gels.

From the EDX analysis results we could see that PEDOT:PSS was mainly polymerized on the surface of the sample 1 (Table 4.2). In rest of the samples, more homogeneous dispersion of PEDOT:PSS was observed. On the other hand, sample 2 showed the most homogeneous sulfur atom dispersion throughout the thickness of the gel while keeping higher relative abundance.

Despite the fact that black/brown color and sulfur atom traces were homogeneous in the cross-section of sample, we could not acquire any conductive path in the gel matrix. The reason for this was thought to be limitation of the molecular length and thus large scale interaction between PEDOT:PSS molecules by the PAAc matrix. Since the monomers were first impregnated in the nanopores of the PAAc matrix, the space limitation and the high hydrophobicity of the PEDOT:PSS resulted in small clusters of PEDOT:PSS molecules without proper expansion of the conductive paths.

**Table 4.2:** The sulphur atom traces obtained by EDX analysis on the cross-section of gel samples.

| S K | Atom wt. % | | | |
|---|---|---|---|---|
| **Location** | **Sample 1** | **Sample 2** | **Sample 3** | **Sample 4** |
| **Surface 1** | 11.3 | 24.6 | 6.2 | 2.5 |
| **Center** | 12.9 | 26.5 | 6.5 | 9.1 |
| **Surface 2** | 78.9 | 25.1 | 6.8 | 2.2 |

We tried to repeat the cycle impregnation and polymerization of EDOT twice in the same PAAc matrix. This way, we aimed to increase the PEDOT:PSS chain lengths and density to achieve conductive paths. For this we chose to use the 5x diluted EDOT/NaPSS solution. After initial polymerization with the addition of 5x less APS and 10x less APS into the EDOT/NaPSS solutions, the gels were put into a buffer solution (pH:6) to swell PAAc matrix. After swelling in the buffer solution for 24 h and rinsing with pure water for another 24 h, we subjected the gels to another cycle of EDOT impregnation and polymerization (Fig. 4.3b).

Using several cycle of polymerization increased the gel opacity indicating higher PEDOT:PSS concentration. This resulted in slightly higher conductivity values, Nevertheless, the obtained conductivity value was still too low to be considered as electronic conductivity. The decrease in conductivity upon drying of the gel confirmed our opinion as discussed before. Unlike reported before by Naficy et al., this strategy is not able to produce conductive gel. Even after several polymerization cycles, the PEDOT chain length or density remains too low to reach electrical percolation.

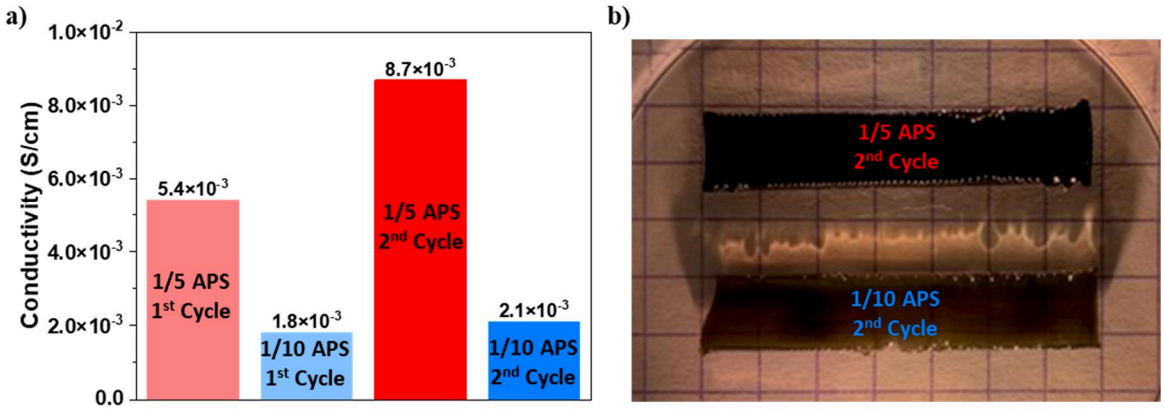



**Figure 4.3 :** a) Conductivity values of PAAc/PEDOT:PSS gels after initial and second cycle of EDOT impregnation/polymerization processes. b) Images of the resulting gel samples.

### 4.2.1. Strategy #2: Single Step Polymerization of AAc with PEDOT:PSS Dispersion

Here, we aimed to overcome the previous limitation. We crosslinked the PAAc gel network around an already polymerized PEDOT:PSS dispersion. This strategy would enable to obtain longer PEDOT:PSS chains more adapted for electrical percolation.

For this method, we used commercial PEDOT:PSS dispersion. Commercial dispersions are easy to use and can ensure high molecular weights. Since PEDOT:PSS is not very hydrophilic, the concentration of the dispersion only 1-1.3 wt.%. It is a dispersion but not a solution after all. PEDOT:PSS can only be conserved in the form of stable colloids thanks to the dopant PSS. Thus, it is generally used for producing conductive films via spin-coating or blade casting methods.

The PEDOT:PSS dispersion is mixed into AAc monomer solution. Then, we polymerized the AAc monomer solution containing PEDOT:PSS dispersion using UV

initiation. We aimed higher interaction between conductive chains since PEDOT:PSS network was not formed under space limitation of another gel matrix.

We used a commercial dispersion (Ossila-PH1000) with ~1.15 wt. % PEDOT:PSS content. By adding different amounts of dispersion, we controlled the PEDOT:PSS content in the solution. We produced mixtures with 0.1, 0.25 and 0.5 wt.% PEDOT:PSS concentrations (Fig. 4.4a). The limiting factor on the final PEDOT:PSS concentration was the low polymer content of the commercial dispersion. We could not achieve higher concentrations by mixing the dispersion with AAc monomer solution.

Upon measuring the conductivity values, we observed that we could not achieve electronic conductivity (4.5-8.5x$10^{-3}$ S/cm). The decreasing conductivity values with increasing PEDOT:PSS content is an indicator for the conductivity is only due to the ions present in the aqueous content of the gel (Fig. 4.4c). Moreover, we dried the gels in order to induce electronic conductivity by potentially decreasing the inter molecular distance in the gel matrix. Unfortunately, the conductivity values decreased further (~$10^{-6}$ S/cm) for all PEDOT:PSS concentrations proving the ion mobility to be crucial for electron transfer inside the gel matrix.

Since we still could not achieve electronic conductivity values (≥ $10^{-2}$ S/cm) with UV polymerized, PEDOT:PSS dispersion containing gel, we aimed to investigate the effect of physical crosslinking of the gel matrix on the PEDOT:PSS chain interactions and at the same time the effect of drying. In theory, physical crosslinks would eliminate any limitation caused by the intermolecular covalent bonds in between AAc reagents. For such reasons, we added commercial PEDOT:PSS dispersion to agarose and physically crosslinked PEDOT:PSS/Agarose gels (Fig. 4.4b).

As can be seen in Figure 4.4c, both neat and 0.5 wt. % PEDOT:PSS containing agarose gels possessed very low conductivity values. We concluded that chemical/physical crosslinking of the gel matrix had no significant effect on the PEDOT:PSS chain interactions to provide electronic conductivity.

The main problem was the disconnection between PEDOT:PSS clusters inside much bigger PAAc gel matrix. Thus, it was required to first construct a percolating PEDOT:PSS matrix ensuring tight packing and interconnection of conductive network before including the second network.

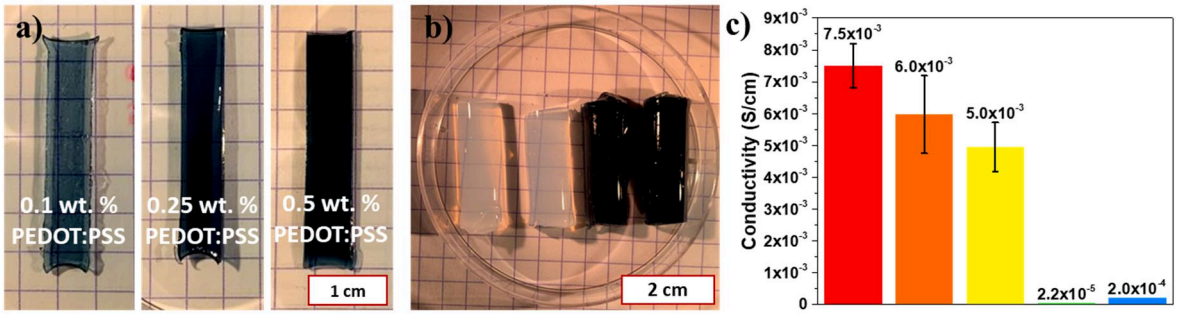



**Figure 4.4:** Images of the a) UV polymerized PEDOT:PSS/PAAc gels b) neat agarose, 0.5wt. % PEDOT:PSS/Agarose gels c) conductivity values of the 0.1 wt. % (red), 0.25 wt. % (orange), 0.5 wt. % (yellow) PEDOT:PSS containing UV polymerized PAAc gels and neat (green), 0.5 wt. % PEDOT:PSS containing (blue) agarose gels.

### 4.2.2. Strategy #3: Impregnation of Gellified PEDOT:PSS with AAc Monomer

In order to ensure high interaction between PEDOT:PSS molecules, we aimed to first construct a percolating conductive matrix of PEDOT in the mm scale. Our aim was to ensure the presence of a conductive path inside the DN gel. Thus, we first gellified the PEDOT:PSS dispersion by de-doping it with strong acid ($H_2SO_4$). Briefly, we subjected the commercial dispersions with 0.1 M sulfuric acid to heat treatment at 75 °C inside sealed plastic tubes to ensure controlled gellfication of PEDOT. The details of the procedure can be found in the appendix (A.4.5). We obtained gellified PEDOT:PSS fibers with 1.6 mm and 3.5 mm diameter thicknesses.

During the heat treatment step, we observed phase separation between the dark, solid phase rich in PEDOT and transparent liquid phase. The phase separation broke the gel fiber into segments of irregular length (Fig. 4.5c). This phenomenon is particularly important when larger fiber diameter (3.5 mm) is targeted or when the system is cast into another geometry such as a thin layer. Therefore, the geometries acquired by gellification of PEDOT:PSS is highly restricted.

To limit such phase separation, we investigated the effect of both acid concentration and the gellification temperature. We investigated the gellification dynamic by using rheology. The experimental method and the results can be found in appendix (A.4.6). Unfortunately, we were not able to obtain significant improvement.

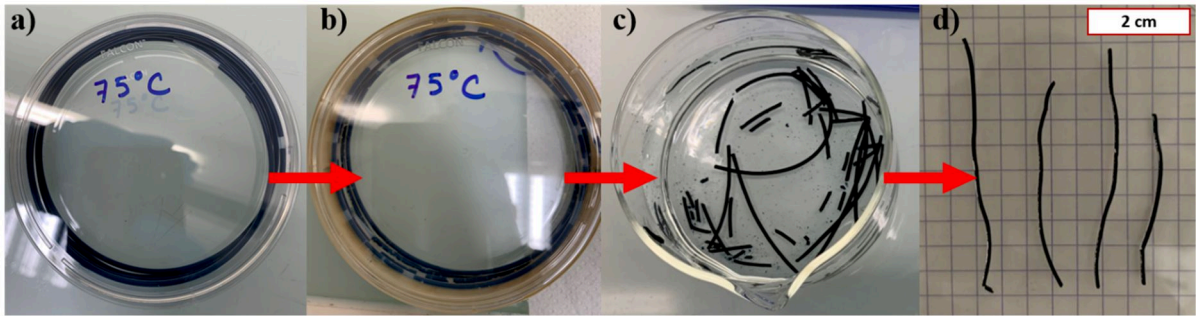



**Figure 4.5:** Preparation steps of the PEDOT:PSS/PAAc double network gel. Images of a) the gellified PEDOT:PSS dispersion injected in the PP tubing, b) PEDOT:PSS gel after heating at 75°C for 1 h, c) PEDOT:PSS gels soaked in the AAc monomer solution and d) PEDOT:PSS/PAAc DN gels with average swollen diameter of 1.6 mm after polymerization of the AAc monomers.

We measured the conductivity of the DN fibrous gels with the four-point probe method. According to the results, electronic conductivity levels were reached for all samples. As can be seen in the Figure 4.6, 1.1 and 0.8 S/cm of conductivity values were calculated for thin and thick PEDOT:PSS/PAAc gels. For the PAAm containing gels, electronic conductivity of ~0.3 S/cm was measured. We also observed that drying increased the conductivity values of the DN gels which is another indicator of electronic conductivity through PEDOT:PSS chains is present in the gel matrix.

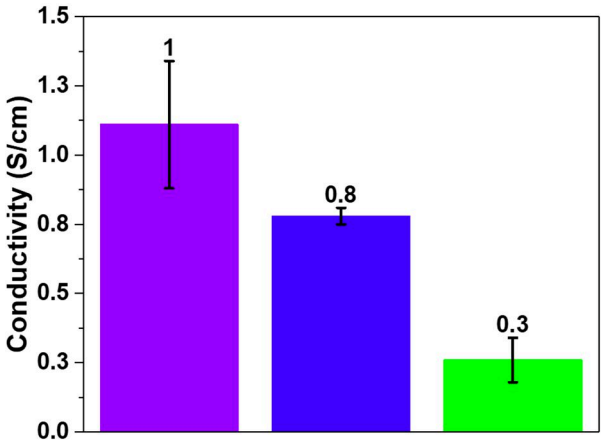



**Figure 4.6 :** Electronic conductivity values of thin (1.6 mm in diameter) PEDOT:PSS/PAAc DN gel (purple), thick (3.5 mm in diameter) PEDOT:PSS/PAAc DN gel (blue) and PEDOT:PSS/PAAm DN gel (green).

### 4.3. Electrochemical Characterization of Double Network Gels

We succeeded to achieve mm scale conductive fibers with strategy #3. We now test the electrochemical properties of the resulting DN gels. According to the literature, hydrogels consisting of conductive polymers such as PEDOT:PSS or PPy possessed super capacitive properties thanks to the electronic/ionic conductivity and high surface area (porous structure) [10–16]. An electrochemical capacitance (pseudocapacitance) is achieved by charge transfer via reversible redox reactions occurring at the surface of the highly ionic polymeric molecules. Since hydrogels are highly porous, the double-layer effect amplifies the capacitance of the system.

In order to observe the performance of the gels, we exposed the samples to 20 consecutive oxidation/reduction cycles in the voltage window ±0.7 V. Moreover, in order to be able to compare the capacitive performance of the DN gel samples, we prepared PEDOT:PSS coated PVDF membranes according to the study by, Temmer et al. (2013) [17]. We first used 0.01M KCl solution as the electrolyte to observe the electrochemical performance of both DN gels and PVDF membrane in the presence of highly mobile, small and relatively inert (against PAAc molecules) ions. The area inside the CV voltammogram gives information on the capacitance of the material.

The PVDF membrane was used as a control sample which is highly porous and conductive thanks to the PEDOT coating. The membrane had a thickness of 0.1 μm and a porosity of 71% (v/v) [17]. This means it had a very high surface to volume ratio. PEDOT coated PVDF membrane showed good capacitive performance because higher surface area increases the charge storage capacity of the material.

The results show that the CV cycles were symmetrical for all gel samples. This indicates that reversible oxidation/reduction reactions occurred on the gel under applied +/- voltages. The voltage scan rate of 100 mV/s was also tested to see the effect of ion mobility inside the gel on the capacitive performance. The decreased number of ions travelling in/out during oxidation/reduction reactions can be seen from the difference in the shapes of the CV voltammograms when 10 mV/s and 100 mV/s scan rates were imposed. Upon faster voltage scans, ions did not have enough time to travel in/out of the gel, as a result flatter voltammograms are acquired. Also, the results show that the gels were highly durable after 20 cycles (Fig. 4.7) at both voltage scan rates.

The capacitive performance (capacitance and symmetry) of the DN gels were similar to PEDOT coated PVDF membrane. The specific capacitance values are calculated by normalizing the capacitance values obtained from CV tests by the amount of active material (PEDOT:PSS or PEDOT mass) in the samples. According to the results, the PEDOT:PSS/PAAc and /PAAm DN gels showed similar performance. 18 and 11 F/g specific capacitances were obtained from PAAc and PAAm containing DN gels, respectively when 10 mV/s was used as the scan rate. On the other hand, PEDOT/PVDF membrane showed a specific capacitance value which is an order of magnitude higher than the DN gels (Fig. 4.7c). If we accept highly porous and conductive PEDOT coated PVDF membrane as a super capacitive material, DN gels with mm scale dimensions showed reasonable capacitive performance (Fig. 4.13c).

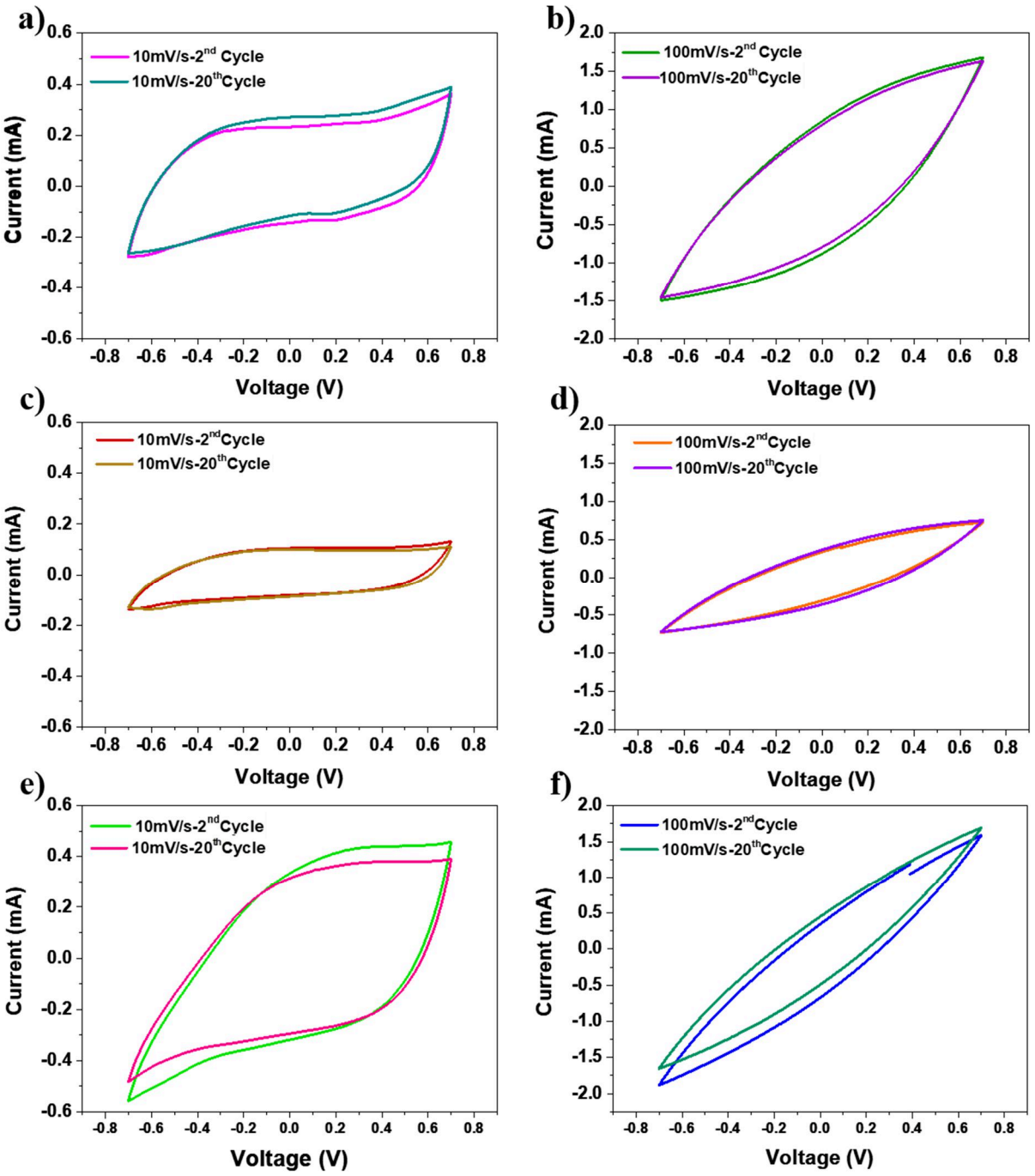



**Figure 4.7:** Cyclic voltammetry graphs in which 0.01 M KCl solution is utilized as the electrolyte, potential window of ±0.7 V applied on a), b) PEDOT:PSS/PAAc gel, c), d) PEDOT:PSS/PAAm gel, e), f) PEDOT/PVDF membrane with 10, 100 mV/s rates, respectively.

### 4.3.1. Electrochemical Performance of DN Gels in the Presence of Copper Ions

Our main aim was to be able to reversibly transfer metallic ions ($Cu^{2+}$, $Ag^{+}$) on the PAAc surface by complexation reactions. Since we introduced conductivity to the gel matrix, the DN gel should possess both super capacitive properties while physically actuating upon reversible redox reactions. To test this, we conducted the same CV tests with the same parameters by using 0.01 M $CuCl_2$ solution as the electrolyte. The details of the method can be found in the appendix (A.4.7).

The CV graphs revealed that less symmetric CV cycles were obtained. This means the number of ions incorporating in oxidation and reduction were not the same. This is due to the complexation of $Cu^{2+}$ ions on the PAAc molecules upon oxidation. Additionally, $Cu^{2+}$ ions are bigger than the $K^{+}$ ions which explains the bigger difference between their respective CV voltammograms at 10 mV/s and 100 mV/s scan rates (Fig. 4.8).

PAAc containing DN gel showed higher specific capacitance with respect to its PAAm containing equivalent. The PVDF membrane on the other hand again had an order of magnitude higher specific capacitance value. This is due to the high porosity (70%) and very high surface to volume ratio resulting in amplified double-layer effect. As can be seen in Figure 4.8e, d, there is less difference in shape between the low and high scan rate CV voltammograms due to the aforementioned shape effects which enables similar ions transport kinetics even at higher scan rates. This was not the same for our mm scale DN gel structure with lower porosity.

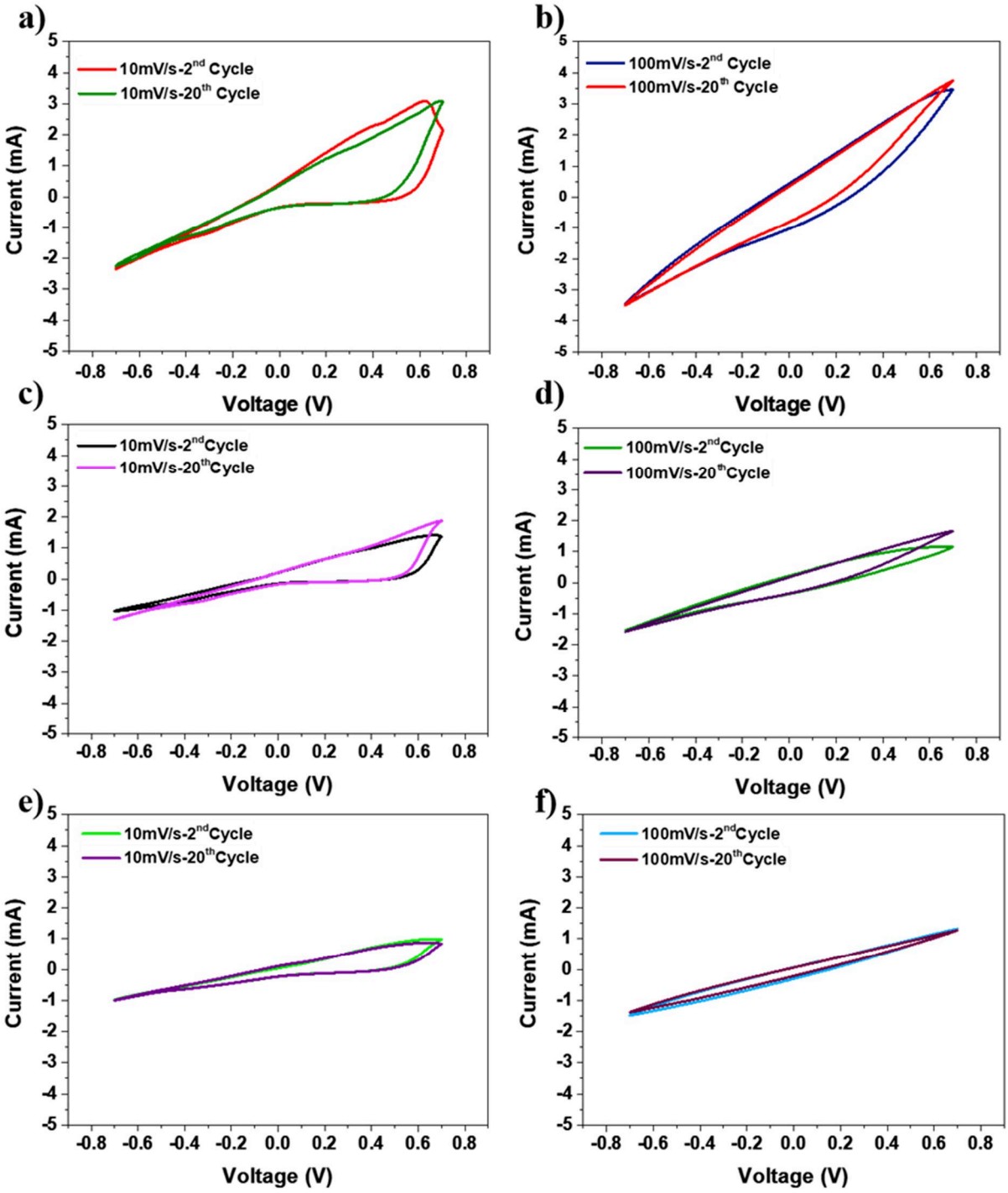



**Figure 4.8:** Cyclic voltammetry graphs in which 0.01 M $CuCl_2$ solution is utilized as the electrolyte, potential window of ±0.7 V applied on a), b) PEDOT:PSS/PAAc gel, c), d) PEDOT:PSS/PAAm gel, e), f) PEDOT/PVDF membrane with 10, 100 mV/s rates, respectively.

When we conducted CV tests on the PEDOT:PSS/PAAc gel, we observed that the color of the gel started to turn brown. Thus, we conducted several CV tests with different voltage windows (±0.2 and ±0.7 V) and different voltage scan rates (10 and 100 mV/s) on the same

sample. As can be seen in Figure 4.9, we did not observe any color change when we applied ±0.2 V either at 10 or 100 mV/s scan rates. Moreover, no color change occurred on the gel when ±0.7Vwas applied to the gel until we decreased the voltage scan rate to 10 mV/s. This means the copper ions accumulated only when higher voltages are applied to the gel for a longer amount of time.

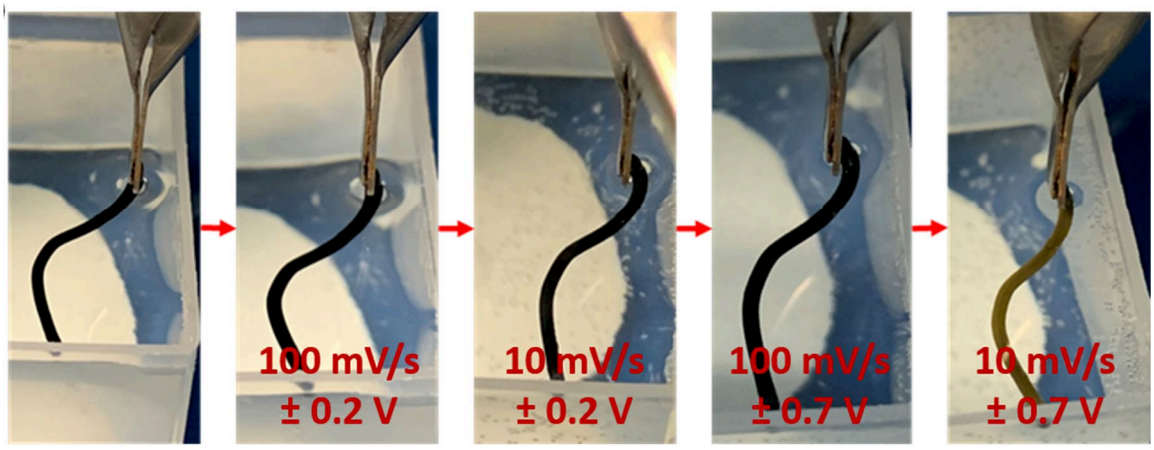



**Figure 4.9:** a) Images of the PEDOT:PSS/PAAc gel before/after subjected to CV tests with different voltage rates and potential windows.

In order to better analyze such phenomena, we conducted chronoamperometry test in which the DN gels were subjected to constant potential (-0.2 V or -1.0 V) for 15 minutes to reduce copper ions and observe where the copper get fixed. After the chronoamperometry, all the samples were rinsed with excess pure water afterwards to remove any unreacted copper ions. We also dipped a gel sample in the copper solution without applying any voltage and rinsed it to use observe the copper attachment on the gel without applied potential. Then, we conducted EDX analysis on the cross-section of the DN gels. We dried, froze and cut the samples before subjecting them to SEM imaging and EDX analysis. We took carbon, oxygen, sulphur and copper atoms into account during EDX analysis. We compared the impact on DN gels.

When no voltage was applied, homogeneous copper accumulation occurred in PAAc matrix. This was due to the sensitivity of AAc molecules to metallic ions. In comparison, we observed less homogeneous copper accumulation in PAAm sample with a high concentration on the surface and lower in the center. The copper accumulation in PAAc was due to complex formation while in PAAm it was only due to surface adsorption.

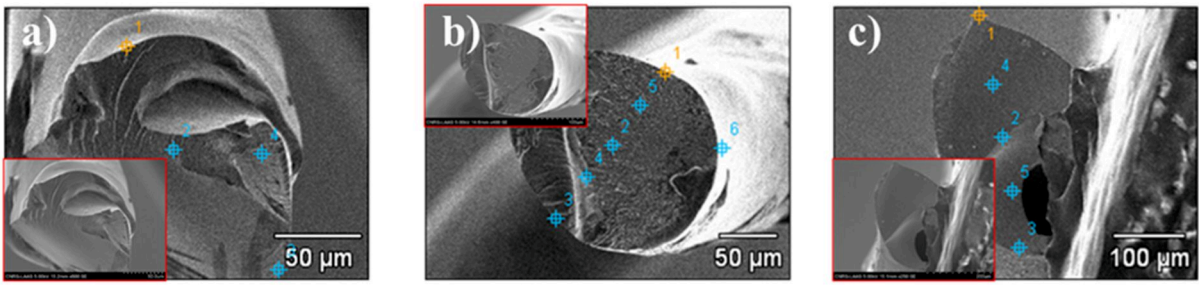
Upon application of voltage, the effect of metal complexation was observed. With -0.2 V applied, the relative abundance of copper atoms increased in both PAAc and PAAm containing DN gels. With -1.0 V applied, the difference between PAAc and PAAm become more apparent but accumulation occurred more homogeneously on the PAAc samples. Whereas copper accumulated mostly on the surface of the PAAm gel. This was due to the affinity of PAAc molecules towards copper ions. Again, we cannot make any exact quantitative analysis without a control sample for calibration but the distribution of copper atoms and differences in relative abundance between samples were clearly observed from the results.

Since PAAc formed complexes with copper, -0.2 V applied potential was only able to force reduction of copper on the PEDOT:PSS molecules throughout the gel matrix (Fig. 4.10b). PAAm gel also showed homogeneous copper distribution throughout its cross-section. This is because the sole driving force for copper accumulation on the sample was the applied potential which is the same throughout the electronically conductive gel matrix (Fig. 4.10e).

According to our understanding, with -1.0 V of applied potential difference, ion transfer into the PEDOT:PSS/PAAc gel was fast and strong enough to homogeneously reach throughout the gel matrix. As a result, complexation occurred homogeneously (Fig. 4.10c). On the other hand, since copper cannot complex with AAm molecules, the sole driving force for ion transfer was the applied potential which drove ions to the gel surface much faster than the inner matrix. We presume that, a more conductive and dense semipermeable layer formed on the surface of the PAAm gel trapping other ions either by electrostatic force or by mechanical entrapment. This resulted in such inhomogeneous accumulation of copper on the gel surface (Fig. 4.10f).

This experiment showed that chemically sensitive PAAc gel could efficiently react with metal ions. On the other hand, the fact that we still observe copper accumulation in cyclic voltammetry at higher voltage windows (-0.7 V) and low scan rate (10 mV/s) means that the copper accumulation cannot be reversed with application of positive voltage (0.7 V).

The reactivity of PAAc gel with copper ions cannot be fully utilized either due to low applied potentials or high scanning rates. At high negative applied potentials the excess accumulation (reduction of ionic copper on conductive network) inhibits the chemical sensitivity of the gel. Thus, higher scanning rates are required which does not let enough ions to be able to diffuse in/out as seen from all the CV test results. In all cases, ions cannot reach the whole gel matrix to induce enough actuation to the gel.




PEDOT:PSS/PAAc in $CuCl_2$

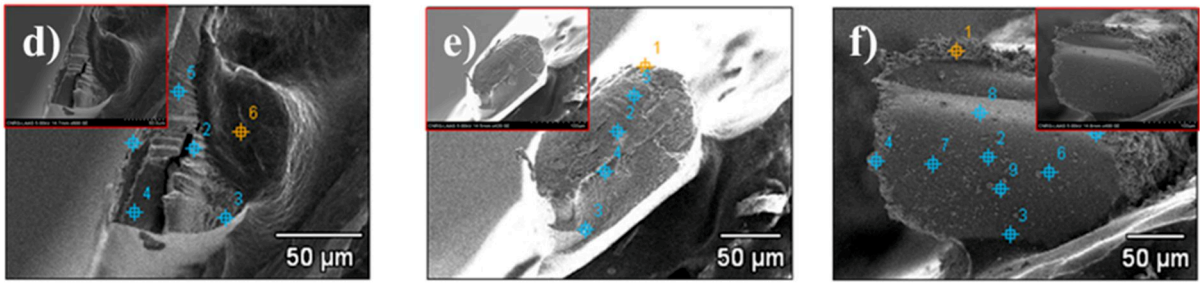
| Cu L | Wt. % |
|---|---|
| Point | Atom |
| 1 | 7.6 |
| 2 | 6.7 |
| 3 | 7.6 |

PEDOT:PSS/PAAc in $CuCl_2$ (-0.2 V)

| Cu L | Wt. % |
|---|---|
| Point | Atom |
| 1 | 14.4 |
| 2 | 19.9 |
| 3 | 20.7 |

PEDOT:PSS/PAAc in $CuCl_2$ (-1.0 V)

| Cu L | Wt. % |
|---|---|
| Point | Atom |
| 1 | 26.5 |
| 2 | 27.1 |
| 3 | 27.9 |




PEDOT:PSS/PAAm in $CuCl_2$

| Cu L | Wt. % |
|---|---|
| Point | Atom |
| 1 | 5.8 |
| 2 | 3.7 |
| 3 | 7.5 |

PEDOT:PSS/PAAm in $CuCl_2$ (-0.2 V)

| Cu L | Wt. % |
|---|---|
| Point | Atom |
| 1 | 12.7 |
| 2 | 10.7 |
| 3 | 13.5 |

PEDOT:PSS/PAAm in $CuCl_2$ (-1.0 V)

| Cu L | Wt. % |
|---|---|
| Point | Atom |
| 1 | 58.2 |
| 2 | 7.8 |
| 4 | 67.5 |

**Figure 4.10:** Cross-sectional SEM images and elemental EDX analysis results after soaking a) PAAc and b) PAAm DN gel into $CuCl_2$ solution. After conducting chronoamperometry with applied potential of -0.2V and -1.0V to the b,c) PEDOT:PSS/PAAc , e,f) PEDOT:PSS/PAAm gels. All gels are washed and dried before analysis.

### 4.4. Macroporous Conductive Double Network Gels

In order to increase the ion transfer rate during oxidation/reduction, we introduced macroporosity to the DN gels. As a result, we aimed to increase the specific capacitance of the gel samples. We utilized the PMMA scaffolding method for which PMMA microspheres (diameter 75 ± 30 µm) were sintered as explained in Chapter 2. We dipped the PMMA scaffolds into PEDOT:PSS dispersion. Then, we dipped them into 0.1 M sulfuric acid solution and used heat treatment to gellify PEDOT:PSS. Afterwards, we immersed the scaffolds with gellified PEDOT in AAc monomer solution to form the second polymer network. Finally, we leached out the PMMA using ethyl acetate treatment. The details of the method are in appendix (A.4.9).

Three type of microporous gel was produced; pure PEDOT:PSS, double network PEDOT:PSS/PAAc and PEDOT:PSS/PAAm. We observed the highly porous gel matrix by conducting SEM analysis on the surface and the cross-sections of the dried samples (Fig.4.11). We observed a very porous structure made of interconnected cells with a diameter of 75 µm to 150 µm. These pores were due to the sacrificial PMMA particles. We also observe much larger pores which are due to the phase separation occurring during gellification of PEDOT:PSS.

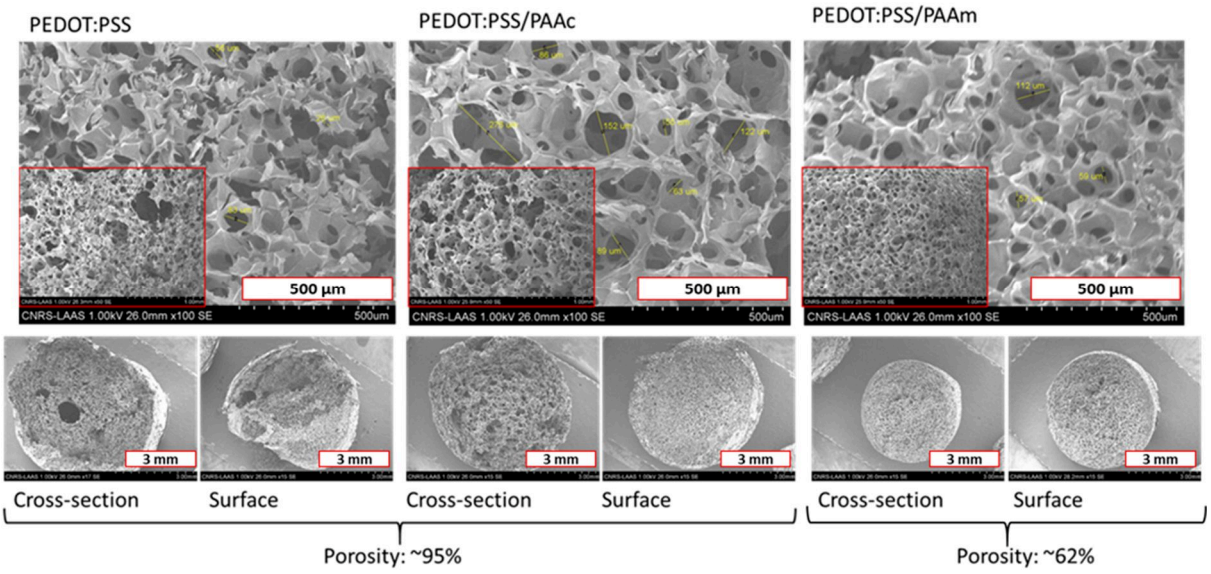



**Figure 4.11:** SEM images of the DN microporous gels.

We compared the conductivity of the macroporous samples and the bulk DN fiber gels with the same composition. In order to see the effect of degree of PEDOT:PSS gellification on the conductive properties, we also gellified PEDOT:PSS with concentrated (18 M ) sulfuric acid. As a result, we obtained the highest conductivity values (11 S/cm), among our samples.

The conductivity of the macroporous gels was smaller than the conductivity of the equivalent bulk gel by 1 to 2 order of magnitude (Fig. 4.12). This difference was mainly due the porous structure which imply that there is less conductive material and thus less conductive path inside the matrix.

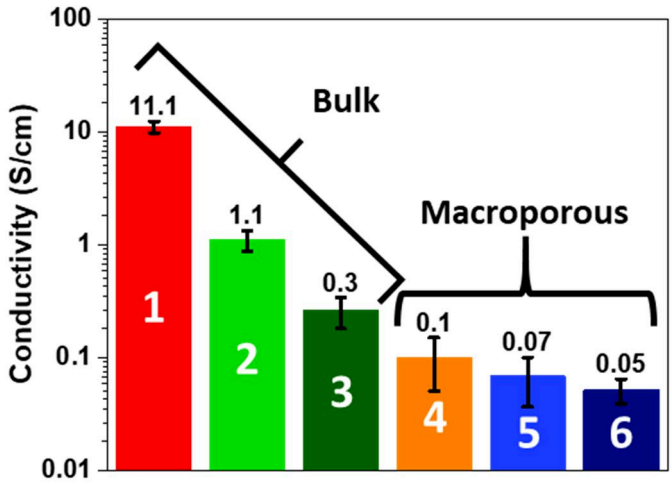



**Figure 4.12:** Bar graph with a log scale depicting the conductivity values of the acid treated PEDOT:PSS gel (18 M sulfuric acid treated) (red, sample 1), PEDOT:PSS/PAAc DN gel (light green, sample 2), PEDOT:PSS/PAAm DN gel (dark green, sample 3), macroporous PEDOT:PSS gel (orange, sample 4), macroporous PEDOT:PSS/PAAc DN gel (light blue, sample 5) and macroporous PEDOT:PSS/PAAm DN gel (dark blue, sample 6).

We also conducted CV tests on the macroporous DN gels with the same parameters. The specific capacitance value are calculated by normalizing the capacitance values obtained from CV tests by the amount of active material (PEDOT:PSS or PEDOT mass) in the samples. Results revealed the significant difference between the PEDOT coated PVDF membrane samples and the rest of the DN gel samples in terms of capacitive performance (Fig. 4.13c, d). The reason for such difference was the high surface to volume ratio of highly porous and thin PEDOT coated PVDF membranes resulting in much higher charge storage capacity. Moreover, both bulk and macroporous DN gel samples showed similar specific capacitance values when KCl was used as the electrolyte. The macroporous samples showed lower specific capacitance values either in the presence of KCL or $CuCl_2$ as the electrolyte. The reason for this is the lower conductivity of the macroporous samples due to the phase separation during PEDOT:PSS gellification. The uncontrolled porosity upon sacrificial scaffolding in gellified PEDOT:PSS reduced the electronic conductivity as mentioned before. Due to the copper ions, bulk DN gels and membrane samples showed higher specific capacitance values in $CuCl_2$ solution due to the

higher ionic charge of copper ions. Finally, PAAc containing samples showed significantly higher specific capacitance values with respect to other gel samples in $CuCl_2$ electrolyte. This is the effect of sensitivity of PAAc molecules towards copper ions resulting in higher ion transfer upon oxidation of metallic copper.

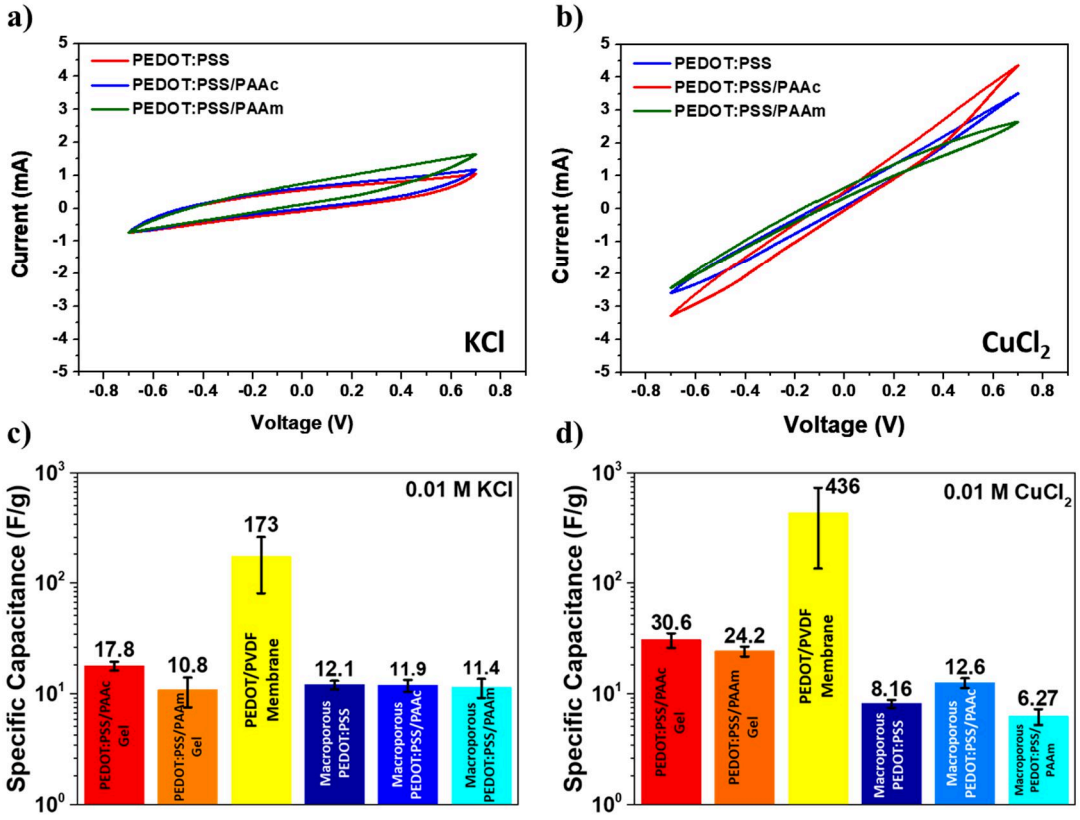



**Figure 4.13:** CV voltammograms of macroporous gel samples in a) 0.01 M KCl and b) 0.01 M $CuCl_2$ electrolytes with 10 mV/s scan rate. Bar graphs (log scale) depicting from left to right, the specific capacitance values of DN PEDOT:PSS/PAAc (red), PEDOT:PSS/PAAm gel (orange), PEDOT coated PVDF membrane (yellow), macroporous PEDOT:PSS (dark blue) and PEDOT:PSS/PAAc (blue), PEDOT:PSS/PAAm (turquoise) DN gel samples measured from CV test results conducted in 0.01 M c) KCl and d)) $CuCl_2$ solutions with 10 mV/s scan rate.

## 4.5. Investigation of Swelling/Shrinking Behavior of PAA Gels in the Presence of $Cu^{+2}$ Ions

One of the key goals of this study was to develop a gel producing actuation. Thus, we determined the level of sensitivity of PAAc to metallic ions. We prepared neat PAAc gel samples as mentioned before but with 3.0 M and 0.7 M AAc concentrations. We soaked the gels in 0.5 M potassium phosphate buffers at pH 3.0 or 6.0 As PAAc has a pKa at 4.5 (pH), gels prepared and swollen in pH 6.0 had larger initial volume than the gels swollen in pH 3 buffer solution.

After soaking the gels in buffers for 24h, we dipped them into $CuCl_2$ solutions with concentrations varying between $10^{-6}$-$10^{-1}$ M. We left the gels in the solutions for 24h. Then we took the gel samples out to gently dry and weight. The gels were also weight before introducing to copper solutions to be able observe the volume change. Finally, the gels were rinsed with excess pure water and left to re-swell for 4 days. The gels were eventually weight again to determine if any re-swelling occurred.

Simultaneously, we measured the changes in copper concentrations in the solutions. Measuring and calculating the difference between the initial/final copper concentrations in the solutions, we aimed to determine the amount of complexed copper in the PAAc gel. We used spectrophotometry since copper was known to absorb light at 780 nm wavelength.

Unfortunately, light absorptivity of copper was too high (>1.0) at concentration values higher than $10^{-2}$ M and too low (<0.01) below to obtain proper calibration curves. Thus, we used complexometric methods. At the concentration range of 3.25-7.75x$10^{-3}$ M we used ethylenediaminetetraacetic acid (EDTA) to from complex with copper ions and amplify the absorptivity. For lower copper concentrations, we used Diethyldithiocarbamate (DDTC) with dodecyl sulfate (SDS) as surfactant. The resulting calibration curves and the details on the spectrophotometric methods can be found in appendix (A.4.11).

According to the weighing results, all gels shrunk to 10% of their initial volume except 3M gel initially at pH 3 (Fig. 4.14). The reason for poor shrinking of this gel was its already shrunk state at the beginning of the experiment (Fig. 4.14a). The pKa of PAAc is at pH 4.5 and the gel is in shrinking tendency below this pH value. This was not a problem for the 0.7 M PAAc gel since lower monomer concentration induced higher water absorption capacity giving higher swollen volume to the gel even at acidic pH values (Fig. 4.14c).

We observed significant volume change in 3 M samples at $10^{-3}$-$10^{-4}$ M copper concentrations. Whereas full shrinking occurred at ~$10^{-2}$ M copper concentrations for the 0.7 M gels. Bigger initial volume of the 0.7 M PAAc gels required more cooper ions to complex with to fully shrink. We were able to determine that ~10% of the AAc monomers in the gels were able to form complexes at such concentrations.

Lastly, we observed that the volume change upon complexation was not reversible for 3 M PAAc gels. The copper complexes did not detach from the AAc monomers even after rinsing with excess pure water for 4 days. On the other hand, 0.7 M PAAc gels were able to re-swell to their initial volumes or even surpass initial volumes upon rinsing. This was thought to be due to the hindrance of the complexed ions in shrunk PAAc matrix at high monomer concentrations. The shrunk 3 M PAAc gel matrix had a caging effect on the copper ions by excess AAc reagents competing for complexation.

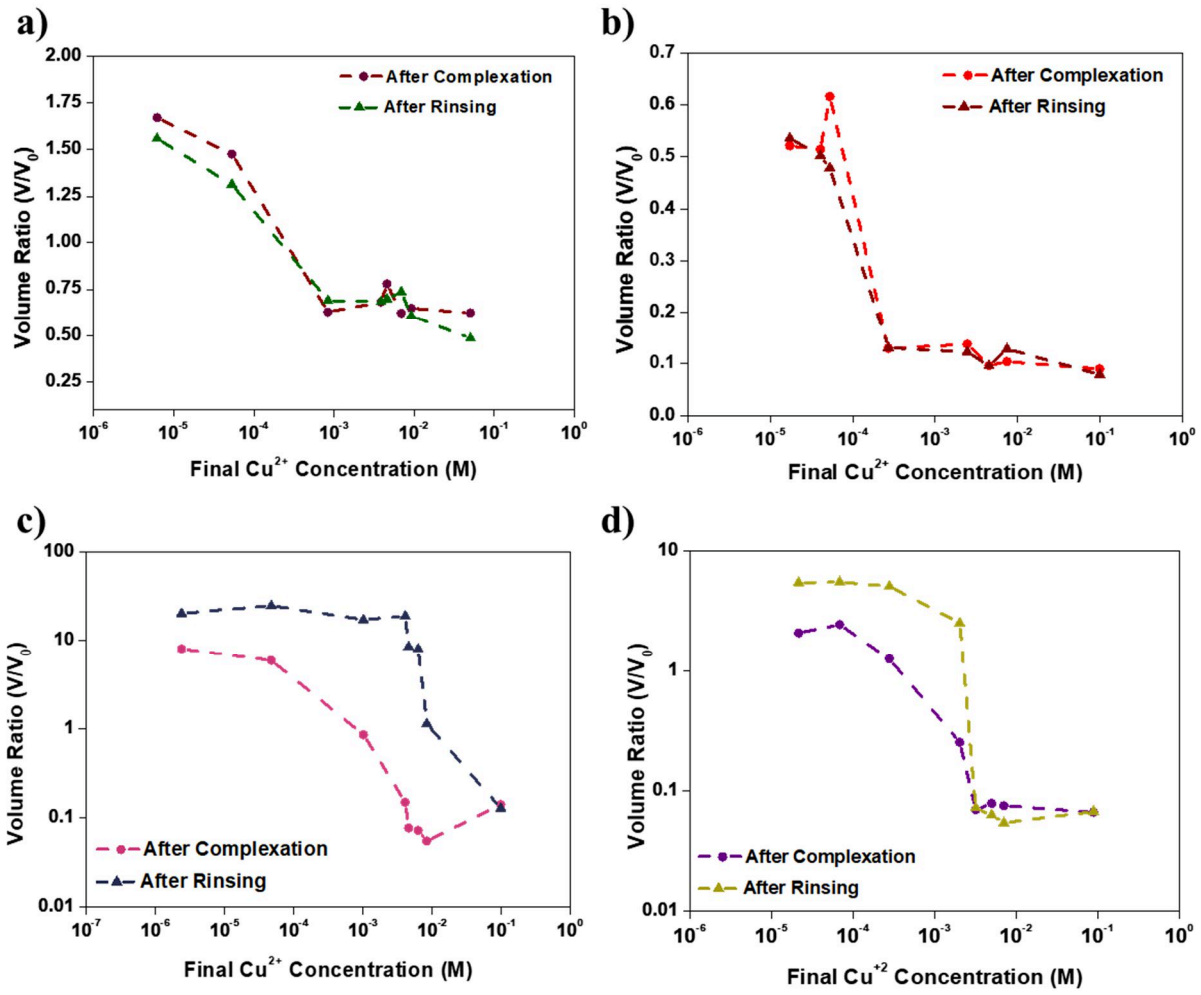



**Figure 4.14:** Graphs showing the volume change of the 3 M PAAc gel initially at a) pH 3, b) pH 6 and 0.7M gels initially at c) pH 3 and d) pH 6.

### 4.6. Can we couple electrochemistry and actuation?

Here we aimed to mimic muscle systems by developing an electroactive, chemically sensitive gel. By introducing electronic conductivity, we aimed to obtain an electrical trigger mechanism on the swelling/shrinking of the chemically sensitive PAAc gel. In this section, we would like to analyze the further steps to be taken to achieve this goal.

We produced conductive DN gel and we have demonstrated the capacity to trap copper ion by copper reduction. Nevertheless, the gellification process of PEDOT:PSS was very prone to instabilities such as phase separations leading to poor control on the resulting morphology. This in turn, limited our control on the conductive DN gel geometries.

Moreover, our experiments revealed that efficient complexation reactions on the AAc molecules could be obtained upon electrical stimulation but this did not lead to significant volume changes. According to our initial expectations, applied electric potential on the conductive PEDOT:PSS network would reversibly trigger the complexation reactions on the AAc reagent of the gel matrix. We believe majority of the copper ions did not reduce by complexing with PAAc molecules but rather reduced on the conductive PEDOT:PSS molecules. In order to better observe the actuation acquired by this method, a bilayer actuator system could be produced. DN gel can be used as the active layer and PAAm gel as the inert second layer can be used. By immersing this system in copper solution and introducing voltage to the conductive DN layer, the small volume change could be amplified in the form of bending motion. When we tried to produce such system, the unreliable gellification process of PEDOT:PSS dispersion prevented acquiring homogeneous, thin (~1.0 mm thickness) layers. The phase separation during heat treatment disrupted the molding process resulting in cracks and inhomogeneous thicknesses.

When we further investigated the shrinking/re-swelling mechanism of neat PAAc gel, we observed that complexed copper ions were not able to detach from the AAc molecules when high (3 M) AAc concentrations were used. We believe this was due to the electrostatic caging effect by the excess AAc molecules around he complexed copper ions. Even though a copper ion could detach from one active reagent upon rinsing, it would be captured and complexed by a neighboring AAc reagent. At lower monomer concentrations (0.7 M), reversible complexation and thus reversible shrinking/re-swelling was achieved. Nevertheless, the 0.7 M gel are very soft and not suitable for conductive DN gel production process. We believe this problem can be addressed by using both chemically sensitive AAc and inert AAm monomers

for producing a gel with similar mechanical properties while ensuring reversible shrinking/swelling upon metal complexation.

As a result, it can be said that production of a stable and efficient electroactive, chemically sensitive artificial muscle material from PAAc gel contain inconveniences at this state.

### 4.7. Conclusion

In this study, our aim was to develop a chemically sensitive electroactive gel for artificial muscle applications. We aimed to utilize complexation capability of AAc molecules with copper ions. Thus, the initial step we took was to introduce electronic conductivity to the gel. This way we could electrically trigger metal complexation and thus, actuation of the gel.

For introducing electronic conductivity, we incorporated PEDOT:PSS as a second network and develop a double network gel hydrogel system. For this, we first investigated several ways to incorporate electronically conductive PEDOT:PSS molecules in PAAc matrix. Methods based on post-polymerization of EDOT:PSS monomers after impregnation into PAAc gel resulted only in ionically conductive materials. This was due to the limiting effect of PAAc network on the relatively hydrophobic and thus denser PEDOT:PSS molecules. We were able to solve such problem by trying the exact opposite. Gellification of PEDOT:PSS network and impregnating with AAc monomers ensured interaction between conductive molecules. This way, we obtained electronically conductive double network gels.

We also investigated the rheological properties of the gellified PEDOT:PSS to improve the efficiency of the physical crosslinking process. Results of the rheological tests revealed that rate of gellification of PEDOT:PSS dispersion was directly related to the applied temperature. Moreover, gellification occurred only over certain temperatures. Unfortunately, we could not solve the phase separation problem even by adjusting the gellification temperature accordingly.

We conducted CV tests on the conductive PEDOT:PSS/PAAc and PAAm gel to determine the capacitive performances. PAAc and PAAm containing double network conductive gels demonstrated specific capacitance values of 18 and 11 F/g, respectively. On the other hand, we could not observe any significant actuation upon electrically triggered metal complexation of PAAc DN gels. Upon cyclic voltammetry and chronoamperometry tests, we observed that efficient copper complexation was not possible either due to accumulation of ions on the gel surface which limits further ion transfer into the gel or high scanning rates resulting in limited ion transfer.

Finally, the copper complexation of the PAAc gels were investigated by exposing the gel samples to different ion concentrations. By investigating the changes in ionic solution after immersion of the gel, we determined the complexation efficiency of the AAc monomers. Moreover, by utilizing complexometric techniques we were able to determine the amount of

copper ion required for significant shrinking values. It was observed that decreasing the AAc monomer concentration in the gels from 3 M to 0.7 M, reversible shrinking/re-swelling could be achieved. Unfortunately, the low mechanical properties of the 0.7 M PAAc gel prevented its utilization in our process.

### 4.8. References


[1] J. Rička, T. Tanaka, Phase Transition in Ionic Gels Induced by Copper Complexation, Macromolecules. 18 (1985) 83–85. https://doi.org/10.1021/ma00143a013.

[2] G. Li, Z. Deng, M. Cai, K. Huang, M. Guo, P. Zhang, X. Hou, Y. Zhang, Y. Wang, Y. Wang, X. Wu, C.F. Guo, A stretchable and adhesive ionic conductor based on polyacrylic acid and deep eutectic solvents, Npj Flex. Electron. 5 (2021) 1–8. https://doi.org/10.1038/s41528-021-00118-8.

[3] T. Tatsuma, K. Takada, T. Miyazaki, UV-light-induced swelling and visible-light-induced shrinking of a TiO 2-containing redox gel, Adv. Mater. 19 (2007) 1249–1251. https://doi.org/10.1002/adma.200602386.

[4] K. Takada, N. Tanaka, T. Tatsuma, A redox actuator based on reversible formation of bond between poly(acrylic acid) gel and Cu2+ ion, J. Electroanal. Chem. 585 (2005) 120–127. https://doi.org/10.1016/j.jelechem.2005.07.024.

[5] S. Naficy, J.M. Razal, G.M. Spinks, G.G. Wallace, P.G. Whitten, Electrically conductive, tough hydrogels with pH sensitivity, Chem. Mater. 24 (2012) 3425–3433. https://doi.org/10.1021/cm301666w.

[6] V.R. Feig, H. Tran, M. Lee, Z. Bao, Mechanically tunable conductive interpenetrating network hydrogels that mimic the elastic moduli of biological tissue, Nat. Commun. 9 (2018) 1–9. https://doi.org/10.1038/s41467-018-05222-4.

[7] B. Yao, H. Wang, Q. Zhou, M. Wu, M. Zhang, C. Li, G. Shi, Ultrahigh-Conductivity Polymer Hydrogels with Arbitrary Structures, Adv. Mater. 29 (2017). https://doi.org/10.1002/adma.201700974.

[8] X. Ma, W. Cai, S. Zhang, J. Guo, X. Peng, Z. Qiu, J. Ying, J. Wang, Highly stretchable polymer conductors based on as-prepared PEDOT:PSA/n-PAA hydrogels, New J. Chem. 42 (2018) 692–698. https://doi.org/10.1039/c7nj03103c.

[9] W. Kong, C. Wang, C. Jia, Y. Kuang, G. Pastel, C. Chen, G. Chen, S. He, H. Huang, J. Zhang, S. Wang, L. Hu, Muscle-Inspired Highly Anisotropic, Strong, Ion-Conductive Hydrogels, Adv. Mater. 30 (2018) 1–7. https://doi.org/10.1002/adma.201801934.

[10] B. Yao, H. Wang, Q. Zhou, M. Wu, M. Zhang, C. Li, G. Shi, Ultrahigh-Conductivity Polymer Hydrogels with Arbitrary Structures, Adv. Mater. 29 (2017). https://doi.org/10.1002/adma.201700974.

[11] M. Hu, J. Wang, J. Liu, J. Zhang, X. Ma, Y. Huang, An intrinsically compressible and stretchable all-in-one configured supercapacitor, Chem. Commun. 54 (2018) 6200–6203. https://doi.org/10.1039/c8cc03375g.

[12] Y. Zhao, S. Chen, J. Hu, J. Yu, G. Feng, B. Yang, C. Li, N. Zhao, C. Zhu, J. Xu, Microgel-Enhanced Double Network Hydrogel Electrode with High Conductivity and Stability for Intrinsically Stretchable and Flexible All-Gel-State Supercapacitor, ACS Appl. Mater. Interfaces. 10 (2018) 19323–19330. https://doi.org/10.1021/acsami.8b05224.

[13] Q. Chen, H. Lu, F. Chen, L. Chen, N. Zhang, M. Ma, Supramolecular Hydrogels for High-Voltage and Neutral-pH Flexible Supercapacitors, ACS Appl. Energy Mater. 1 (2018) 4261–4268. https://doi.org/10.1021/acsaem.8b00891.

[14] Z. Yang, J. Ma, B. Bai, A. Qiu, D. Losic, D. Shi, M. Chen, Free-standing PEDOT/polyaniline conductive polymer hydrogel for flexible solid-state supercapacitors, Electrochim. Acta. 322 (2019) 134769. https://doi.org/10.1016/j.electacta.2019.134769.

[15] W. Teng, Q. Zhou, X. Wang, H. Che, P. Hu, H. Li, J. Wang, Hierarchically interconnected conducting polymer hybrid fiber with high specific capacitance for flexible fiber-shaped supercapacitor, Chem. Eng. J. 390 (2020) 124569. https://doi.org/10.1016/j.cej.2020.124569.

[16] K. Rohtlaid, G.T.M. Nguyen, S. Ebrahimi-Takalloo, T.N. Nguyen, J.D.W. Madden, F. Vidal, C. Plesse, Asymmetric PEDOT:PSS Trilayers as Actuating and Sensing Linear Artificial Muscles, Adv. Mater. Technol. 6 (2021) 1–13. https://doi.org/10.1002/admt.202001063.

[17] R. Temmer, A. Maziz, C. Plesse, A. Aabloo, F. Vidal, T. Tamm, In search of better electroactive polymer actuator materials: PPy versus PEDOT versus PEDOT-PPy composites, Smart Mater. Struct. 22 (2013). https://doi.org/10.1088/0964-1726/22/10/104006.

## General Conclusions

In this thesis, we presented our work on development of hydrogel based fast actuators. Hydrogels have high potential for efficient and compact actuators they can produce high actuation amplitudes even at low initial volumes. On the other hand, there are still some factors limiting their potentials. We present that the slow actuation rates, low volume ratio and precise control of the actuation dynamics were the main limitations before revealing the true potential of smart gel based actuators.

The reason for slow actuation was the limited diffusion rate of solvent inside the gel matrix. Since hydrogels require to expel or absorb water in order to shrink/swell, respectively, diffusion rate of water plays a critical role in actuation rates. We introduced macroporosity to the gels to decrease the average diffusion path length of solvent in the gel. This way, fluid could freely flow in the interconnected pores accelerating fluid transport during shrinking/swelling.

Inducing macroporosity to hydrogels has always been a challenge. There have been several ways to introduce macroporosity to the gels all based on templates. These templates could be foams, emulsions, ice (freezing-thawing) or solid particles (PMMA) but none of these methods provide good control on the level of porosity or pore geometries. Having control on the hydrogel macroporosity is very important since it directly affects the actuation rates and mechanical properties of the gel.

We developed a novel sacrificial scaffolding method in which we could shape and control the porosity level. We used shellac as the sacrificial template. Shellac is a hydrophobic material which can easily melt and shaped at low temperatures. While its hydrophobic structure ensures precise templating in aqueous environments (during polymerization of aqueous monomer solutions), shellac can be selectively dissolved at high pH aqueous solutions. Moreover, we developed a melt extrusion 3D printing method for shellac and obtained precise template structures. This way we acquired precise template architectures providing good control on both the pore geometries and porosity levels of the gel.

Moreover, we aimed to overcome the complexity of controlling hydrogel actuators by using temperature as the trigger. For this we used PNIPAM as the thermally sensitive material. Temperature remains as one of the simplest stimulus to control actuation as it does not require direct contact with the material and can be adjusted by many ways (conduction, convection or radiation). Upon our experiments we realized that heat dissipation posed as the main obstacle

before precise control over temperature. We could not ensure homogeneous heat dissipation over the whole gel volume due to this problem. Moreover, low efficiency of heat sinks resulted in accumulation of heat in the system decreasing the cyclic efficiency of the actuator.

Nevertheless, we were able to both highly accelerate and provide symmetrical shrinking/swelling of PNIPAM gel with macroporous matrix. We developed a simple, compact and energy efficient actuator system alternative to commercial technologies (piezo-electric). We also provided comprehensive analysis of the developed system providing its mechanical, cyclic and thermal performance.

We then developed a hydrogel actuator based on an electrochemical control mechanism. A certain level of electronic conductivity in the gel is required in order to use electrochemical stimuli to control actuation. For this, we used a conductive gel PEDOT:PSS. We produced a double network PEDOT:PSS/PAAc gel with high electronic conductivity. We aimed to control the chemical sensitivity of PAAc gel against metallic ions and trigger its volume change (shrinking/re-swelling) by applying electrical potential. Our experiments revealed that gellification of PEDOT:PSS dispersion resulted in conductive gel network but the process was prone to phase separation. This prevented any control on the resulting gel geometry. As a result, we were not able to apply this method accordingly to obtain desired actuator shapes (thin layer). We were also able to determine the reversibility of the volume change of PAAc gel upon metallic complexation. We revealed that certain copper concentrations in solution and monomer concentrations in the gel are need to be ensured to obtain reversible shrinking/re-swelling of PAAc actuators.

To summarize, we developed fast actuating hydrogel actuators and investigated the applicability of such material in Braille device and artificial muscle applications. We revealed that there are several limitations on the controlling and production methods of such materials. Nevertheless, smart hydrogels pose great potential for future actuator technologies with its high actuation stroke to volume, elasticity and processability properties. Because actuation technology always pursues, smaller, more efficient and adaptive systems to develop a better world.

# Appendix: Materials and Methods

## A.2-Chapter 2: Development of a Braille Device Utilizing Thermo-Sensitive Macroporous PNIPAM Hydrogel as the Fast Actuator

### A.2.1 Preparation of NC Gel

The preparation of bulk nanocomposite gel (NC) was as follows. NIPAM monomer (2.26 g, 1.3 M) was dissolved in 15 mL of pure water. After fully dissolving the monomer, Laponite-RDS (1.52 g, 7.7 wt. %) was slowly added to the solution under high-speed stirring to prevent coagulation during mixing. The solution took a homogeneous semitransparent cloudy appearance upon Laponite addition. After addition of the initiator APS, the solution was put into an ice bath and purged with nitrogen for 15 min. Finally, the solution was poured into cylindrical 2 × 4 mm and 4 × 4 mm (DIxH) molds after addition of 16 μL of TEMED. Polymerization took place at room temperature for 20 h.

### A.2.2 Preparation of OR Gel

The preparation of organic reticulated gel (OR) was as follows. NIPAM monomer (2.26g−1.2 M) was dissolved in 17.1 mL of pure water. Then, 1.9 mL of a solution of MBIS in water (3 wt %) and 100 μL of a solution of Irgacure 651 in ethanol (10 wt %) were added. The solution was poured into a mold and placed under an UV lamp inside an ice bath for 5 min.

### A.2.3 Preparation of High Porosity (HP) Gels

HP gels are obtained when PMMA micro spherical particles were used as the scaffold building block. For this, PMMA microspheres with average diameter of 75 ± 30 μm are poured into a glass cylindrical mold (dxh 7x10 mm for compression, shrinking/re-swelling tests and 4 x 4 mm for single pin braille setup) and heated to 185 °C for 8 hours to sinter them onto each other. This way, highly interconnected and densely packed matrix is obtained. The obtained PMMA cylinders were soaked into NIPAM solution under vacuum for 4h and left overnight in the solution to allow full coverage of the micro spherical surfaces. Then, the scaffolds were taken out of the solution and placed under the UV lamp for 20 min each side on an ice bath. The polymerized samples were rinsed with ethyl acetate for 4 days by refreshing the solution every 24h to selectively dissolve PMMA scaffold. This method was not suitable for the NC

gels since physically crosslinked polymer matrix could not endure ethyl acetate treatment. Obtained HP-OR gels were then rinsed with ethanol and swollen in pure water before further utilization (Fig. A.1). Due to the packing density of the PMMA microspheres, the pore density obtained was 60%. The pore density of the hydrogel was indirectly measured from the density of the scaffold. Thus, samples produced by this method are referred as HP gels for the rest of this thesis.

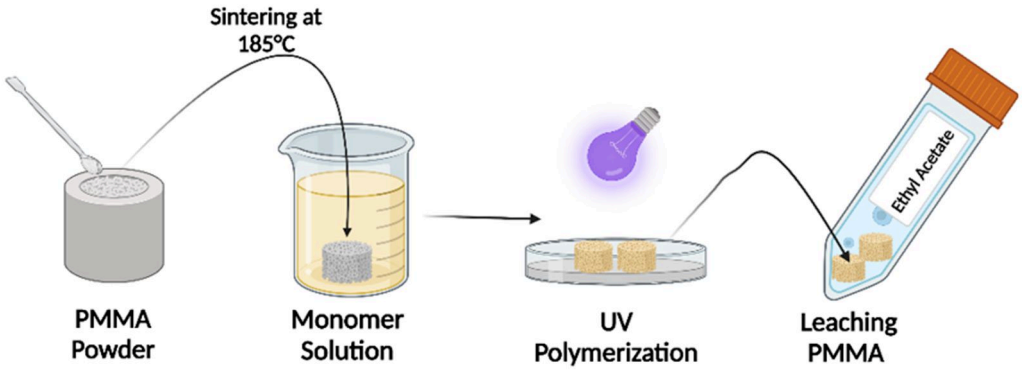



**Figure A.1:** Schematic representation of macroporous HP-OR gel preparation based on PMMA spherical micro particles.

## A.2.4 Preparation of Low Porosity (LP) Gels

Low porosity (LP) gels on the other hand were obtained by using shellac fibers as sacrificial scaffold. Shellac is a natural material produced by a bug (Kerria lacca) which is a native to Asia. We have produced microfibers with average diameter of 12 ± 5 μm using melt-spinning method. The shellac microfibers were produced by using a cotton candy machine (VEVOR-FR). The shellac flakes were melted at 170 °C (125 V) and collected by an aluminum rod coated with a paper towel. In order to remove any hydrophobic contaminants, the fibers were rinsed with excess ultrapure water and dried at room temperature for 3 days. The shellac floss that was tightly packed during drying was placed in a Petri dish. For the LP-NC gel, the monomer solution was injected between the floss and left to polymerize at room temperature for 20 h. For the LP-OR gel, the Petri dish was placed under a UV lamp and inside an ice bath for 20 min. Cylindrical samples with 2 and 4 mm diameters were cut out from the polymerized OR and NC gel by using a hole-punch and placed in a 0.5 M NaOH solution to leach the shellac fibers out of the gel matrix. The gels were left in NaOH solution under constant agitation by changing the solution every 24 h until shellac fibers were visibly removed. Then, the gels were washed in a water bath (Fig A.2).

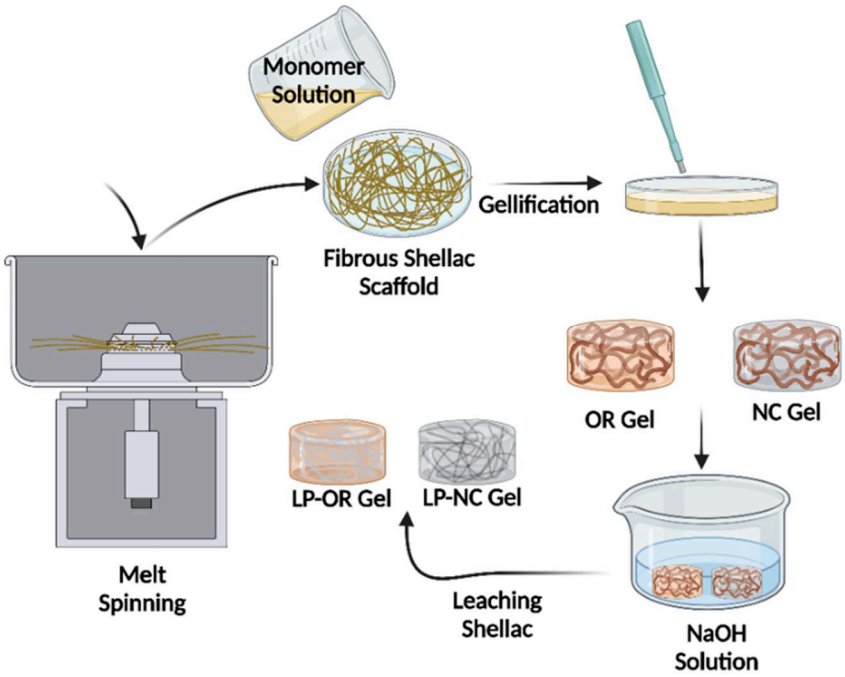



**Figure A.2:** Schematic representation of macroporous HP-OR gel preparation based on PMMA spherical micro particles.

## A.2.5 Mechanical Testing

In order to characterize the swollen gels mechanically, compression tests were performed. A mechanical testing machine (Mark-10 ESM301) was used (Fig. A.3). Both the Young's modulus and compression strength at certain strain values were determined for all samples. To determine the true stress and the Young's modulus values, we assumed a Poisson ratio of 0.5 (incompressible material). The Young's modulus values were determined in the range of 10− 20% deformation for all samples.

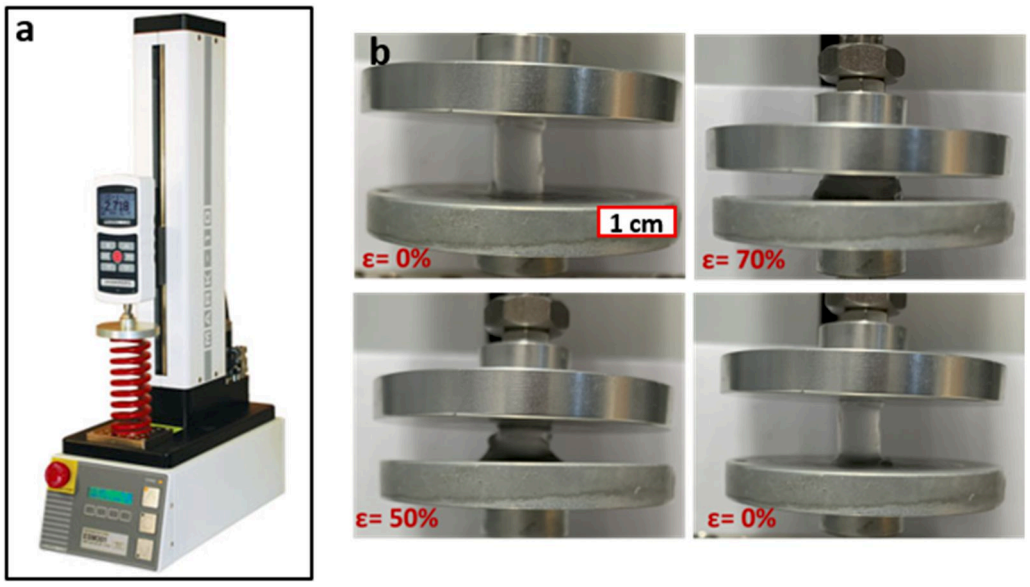



**Figure A.3:** a) Mark-10 ESM301 mechanical testing machine. b) Compression stages of HP-OR gel.

## A.4 Chapter 4: Development of an Electroactive PAAc/PEDOT:PSS Hydrogel Actuator

### A.4.1 Impregnation of PAAc Gel with EDOT Monomers

As the method for producing DN conductive gel, we dipped pre-polymerized PAAc gels into EDOT monomer solution. The AAc monomer solution is prepared as follows. To acquire 2.907 M AAc concentration, 3.9 ml of pure AAc is mixed with 7 ml of pure water. Then, 9 ml of bis-acrylamide solution (3 wt. % MBAA in water) is added. The solution was degassed for 15 min with nitrogen purge. Finally, 0.1 ml of UV-initiator (Irgacure 651) solution (10 wt.% in AA) of is added. The AAc gels are polymerized with under UV lamp for 5 minutes. The acquired PAAc gels are then dipped into EDOT:PSS dispersion.

2 g of NaPSS was dissolved in 20 ml of water (0.8 M). Then 1.3 g of EDOT was added. The mixture was sonicated in a sonic bath for 30 minutes. At this stage, the PAAc gels were immersed into the dispersions and left at RT for 5 days with mild stirring on the rotator. We introduced 2.6 g APS in two different ways. For some samples, we added APS directly into the dispersion after stirring the EDOT/NaPSS dispersion with PAAc in it for 5 days and let the polymerization go on for 3 days. For the other samples, we took out the immersed PAAc gels from EDOT/NaPSS dispersion after 5 days of spinning and then put the gels into APS solutions

for initiation of the polymerization. The gels are kept 3 days in APS solutions. Additionally, 5 times dilution of the EDOT/NaPSS dispersions and APS solutions are also experimented. The produced gels were rinsed with excess water to get rid of any unreacted ingredients and fully swollen before testing.

## A.4.2. Four Point Probe Conductivity Measurement

The conductivity of the gel samples is measured via four-point probe method. We produced a setup by sticking copper tapes on glass slides. 4 stripes of copper tapes are stuck on one side of the glass slide. Two points were selected on the outer part and two other points on the inner with predetermined distance between the inner points. The tapes on one side (left or right) of the glass slide is connected to the negative and the other side to the positive potential via alligator clips. A symmetrical glass slide is also prepared to sandwich the gel samples in between. This way, we ensured four points contact on both sides of the gel sample to provide current flow through the gel matrix. The probes were connected to a sourcemeter (Keithley 2400) and up to 1 mA of current is applied, current sweeping with 0.1 mA of steps us used. Resulting voltage data is acquired according to the Ohm`s Law. The conductivity is measured using the equation;

$$\rho = R\frac{A}{l} \qquad (A.1)$$

where ρ (Ω.m) is the electrical resistivity, R (Ω) is the resistance of the material, A ($m^2$) is the cross-sectional area perpendicular to the direction of current flow and l is the length of the specimen or in our case the distance between the nearest probes (5 mm). The conductivity (σ, Ω/m) is calculated by the relation ρ=1/σ. All the gel samples were tested at fully swollen state.

## A.4.3 Single Step Polymerization of AAc with PEDOT:PSS Dispersion

As the PEDOT:PSS dispersion we used Ossila-PH1000 with 1.15 wt. % solid content. The AAc monomer solution was prepared as in A.4.1. The amount of water in the solution was adjusted according to the amount of commercial dispersion added to acquire PEDOT:PSS concentrations of 0.1, 0.25 and 0.5 wt.% in the gel. All the solutions were crosslinked for 5 minutes under UV lamp. The produced gels were rinsed with excess water to get rid of any unreacted ingredients and fully swollen before testing.

## A4.4 Production of Agarose/PEDOT:PSS Gels

We prepared neat agarose gels by dissolving 4wt. % Agarose Type-B in water. Then it was heated over 36°C and cooled to physically crosslink the gel matrix. For the PEDOT:PSS/Agarose gels, the predetermined amount of PEDOT:PSS dispersion was added to the agarose solution and stirred thoroughly before heating/cooling. The produced gels were rinsed with excess water to get rid of any unreacted ingredients and fully swollen before testing.

## A.4.5 Impregnation of Gellified PEDOT:PSS with AAc Monomer

In gellification of the commercial dispersion, we utilized the sulfuric acid treatment. We produced 0.1 M sulfuric acid containing dispersions. Following the method in the study by Yao et al. (2017), we quickly (before gellification started) drew the dispersion into a syringe and injected it into polypropylene microfluidic tubes with internal diameter of 1.32 mm. After placing the tubes into a petri dish, we sealed it with an autoclave tape. The petri dish was heated at 75°C for 3h. Afterwards, we pumped out the gellified PEDOT:PSS from the tubes by using an empty syringe directly into an AAc monomer solution. The gellified PEDOT:PSS was kept under dynamic vacuum for 1,h after soaking in the AAc monomer solution to get rid of any bubble left inside. Finally, the soaked gels were taken out and AAc monomers inside the physically crosslinked PEDOT:PSS matrix were polymerized at 80°C for 1 h in separate eppendorfs to prevent drying. In the AAc monomer solution, we used 2.907 M AAc monomer, 0.0875 M MBAA (n,n'-methylenebisacrylamide) and $1.33x10^{-3}$ M 4,4'-Azobis(4-cyanopentanoic acid) thermal initiator. The DN gels were rinsed with excess pure water to remove remaining nongellified PEDOT:PSS and unreacted AAc monomer solution remnants

## A.4.6 Rheological Characterization on the Gellification Process of PEDOT:PSS Dispersion

In order to determine the optimum heating and acid concentration parameters for a more stable gellification process, we conducted rheology tests on the acid treated PEDOT:PSS dispersion. An AR-2000x rheometry (TA Instruments) is used. A steel cone with 20 mm of diameter was used for the head. 40 µl of acid treated PEDOT:PSS dispersion was put between the cone and the surface (Fig. A.4).

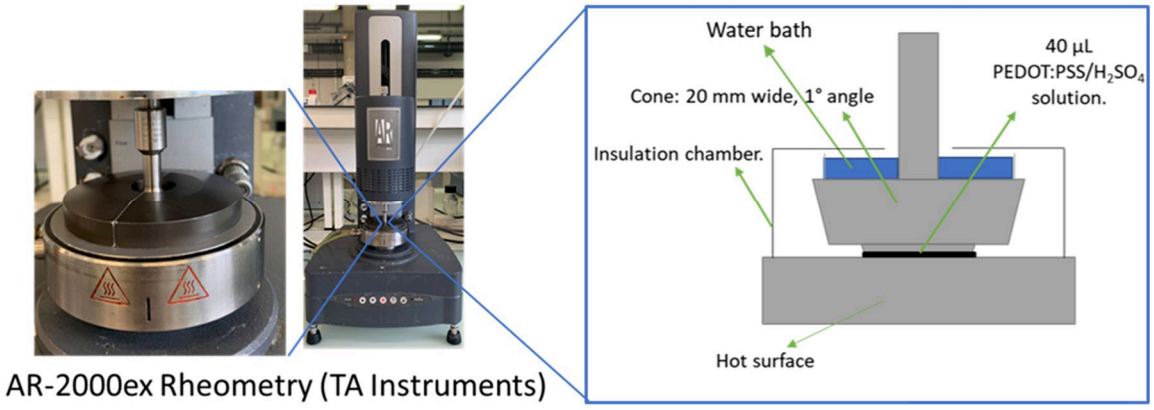



**Figure A.4:** Images of the AR-2000X rheometer and the schematic of the cone head used on the PEDOT:PSS dispersion.

Strain sweep was done at room temperature up to 5% strain at 1, 10 and 100 Hz frequency to find the appropriate experimental parameters. Eventually, for each experiment oscillation frequency of 1 Hz and 0.2 % strain was selected for the rest of the experiments. The tests were done in continuous oscillation mode.

After determining the right strain and frequency parameters, we applied different temperatures to the 0.1 M sulfuric acid containing dispersions. According to the results, we did not observe any significant gellification at room temperature since there was no increase in storage modulus value (Fig. A.5d). Gellification started to be apparent after applying 55°C for 5 minutes. On the other hand, we also did not observe a significant increase in storage modulus value after 5 minutes until the applied temperature was increased up to 70°C (Fig. A.5d). We conducted the experiments up to 85°C of applied temperature and observed that gellification is too fast to let us manipulate the dispersion before full gellification at such elevated temperature. Moreover, to prevent phase separation due to fast gellification, we tried heating the dispersion first to 55°C and after 20 minutes we increased the temperature up to 75°C. We selected the

55°C as the initial applied temperature because the storage modulus increase to very close values as in the 70°C case but slower. It can be seen from the graph (Fig. A.5d) that two lines (55°C and 70°C) coincide after 20 minutes. This way we aimed to slow the initial gellification process to prevent phase separation due to the sharp change in viscous properties. As can be seen in the graph (Fig. A.5e), the resulting gels had similar properties after 50 min but the step heating slowed the the overall process.

Finally, we tested the effect of different sulfuric acid concentrations on the gellification kinetics. We used 10 and 100 times diluted dispersions and tested them with heating at 75°C for an hour. We observed that, upon 10 and 100 times dilution, the dispersion reached lower storage modulus values as expected. The effect of concentration is observed to be very significant on the final mechanical properties of the gel. This result also agreed with the literature [6,10]. Thus, we continued to use 0.1 M as the acid concentration in producing physically crosslinked PEDOT:PSS gels.

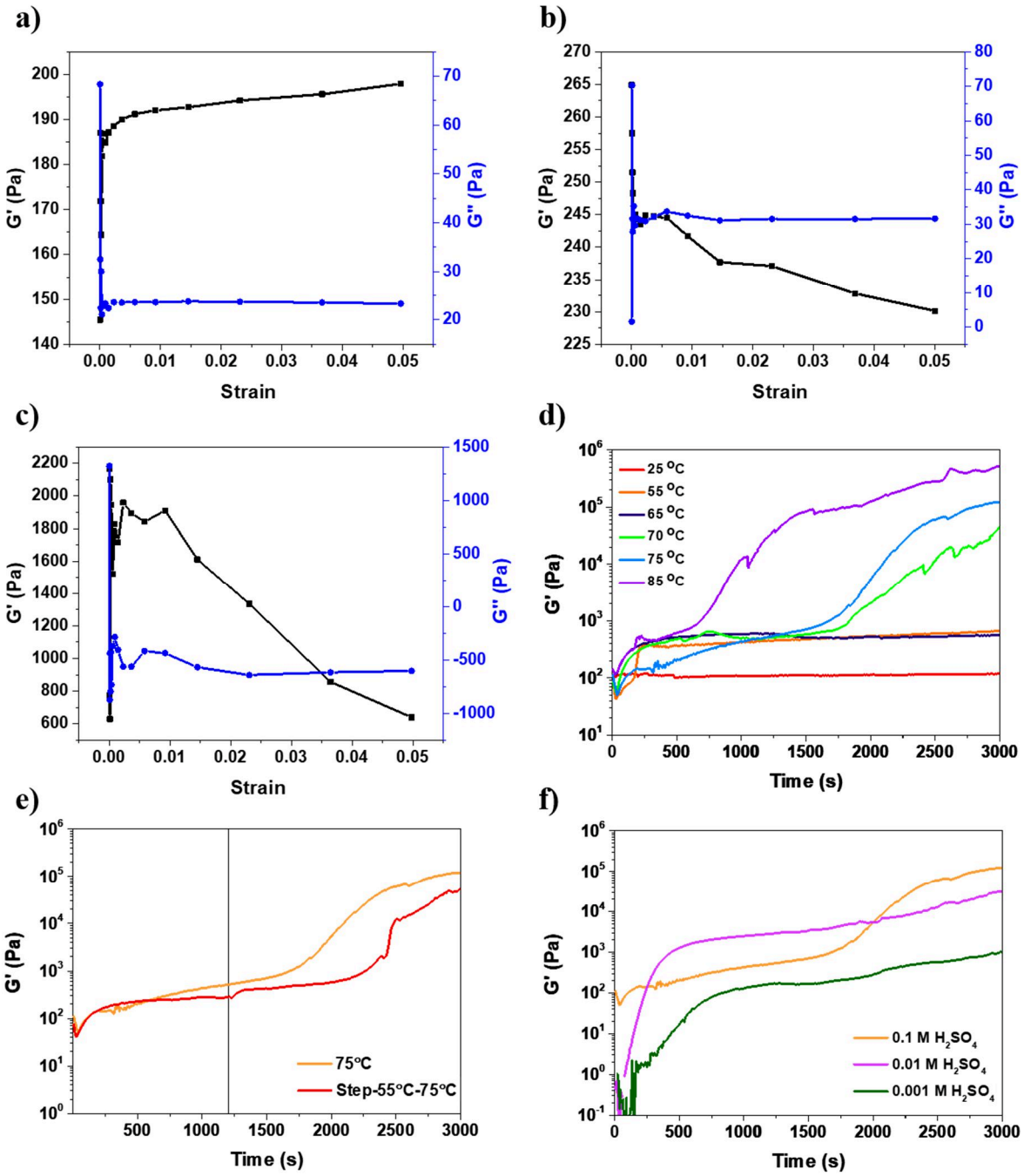



**Figure A.5:** Strain sweeping test results in the range 0-5 % strain at a) 1Hz, b) 10 Hz and c) 100 Hz oscillation frequency. Graphs depicting change of storage modulus (G') with respect to time with different applied d) temperatures, e) two-step heating from 55 to 75°C program sulfuric and f) acid concentrations.

## A.4.7. Electrochemical Characterization of DN Hydrogels

In CV test, we used three electrode system in our electrochemical cell. Conductive DN gel was the working electrode whereas platinum wire and Ag/AgCl were used as the counter, reference electrodes, respectively. 1 M KCL and 0.01 M $CuCl_2$ solutions were used as the electrolytes. In CV test, the gel was cyclically charged between +0.7 and -0.7 V using a potentiostat (VMP3) to induce oxidation/reduction on the ions. From this test, we were able to identify potentials required for the oxidation/reduction reaction occurring on the gel surface. Additionally, the area of the cycle and the rate of the test reveals the specific capacitance value of the samples with the relation,

$$C = \frac{\int IdV}{\nu \times m \times \Delta V} \qquad (A.2)$$

where the integral corresponds to the area under the curve (A.V) after a cycle, ν is the scan rate (V/s), m is the mass of the capacitive content in the sample (characteristic mass) (g) and ΔV (V) is the potential window of the test. Moreover, also the total surface area of the sample can also be used instead of the mass (F/g) for specific capacitance ($F/cm^2$) calculations. In our study we used 10 and 100 mV/s as the scan rates.

In determining the specific capacitance values, data from the 10 mV/s scan rate CV test results are used. The capacitance values are normalized by the amount of active material in the samples which are PEDOT or PEDOT:PSS. For bulk samples, we determined the mass of PEDOT:PSS per volume of the DN sample. Using such correlation, we were able to determine the PEDOT:PSS amount in each sample. For the macroporous DN gel samples, since we produced them in separate eppendorfs in a batch process, we had the data of PEDOT:PSS mass per sample. Lastly for the PEDOT coated membrane samples, we determined the PEDOT mass by subtracting the mass of the membrane from the coated sample.

## A.4.8 Preparation of PEDOT:PSS Coated PVDF Membrane

The commercial PVDF 110 μm thick membrane with 70% porosity and 0.1 μm sized pores was soaked into EDOT/PSS solution to impregnate with enough monomers. Then, the membrane surface was wiped dry with a filter paper and dipped into $FeCl_3$ solution (1.5 M) at 60°C to initiate oxidative polymerization of PEDOT:PSS. After the membrane turned dark, it was washed with excess methanol to terminate the polymerization and remove unreacted

monomers. Finally, the membrane was rinsed with methanol and water before drying at 40°C for 1h under vacuum.

### A.4.9 Preparation of Macroporous Conductive Double Network Gel

We dipped the PMMA scaffolds into PEDOT:PSS dispersion for 7h under vacuum and then left overnight. Then, we took soaked the samples into 0.1 M sulfuric acid solution for 1h under vacuum. Afterwards, we took put took the samples out and heated in oven 70°C for 3h to physically crosslink the PEDOT:PSS. Then, we soak the samples into AAc monomer solution for 3h under vacuum. After taking out of the vacuum we left the samples in the monomer solutions overnight in the fridge. Finally, we polymerized the AAc at 80°C for 1h and leached the PMMA scaffold with ethyl acetate treatment as in Chapter 2. We rinsed all the sampled with excess pure water at the end to remove non-gellified PEDOT:PSS molecules, AAc monomers and fully swell the DN gel.

### A.4.10 Preparation of Buffer Solutions

For the pH 3 buffer, we prepared 0.5 M potassium phosphate solution and added phosphoric acid until pH 3 was obtained. Then the solution volume was increased with enough water. For the pH 6 buffer, we prepared solution with 0.3 M dipotassium phosphate and 0.2 M potassium phosphate.

### A.4.11 Determination of Copper Concentrations via Complexometric Spectrophotometry Method

Our initial plan was to determine the copper concentration in the solutions before and after introducing PAAc by using UV-Vis Spectrophotometry (Nanodrop 2000c). We aimed to utilize the fact that copper solutions have an absorption peak around 780 nm at high concentrations. Upon testing, we realized that the absorbance values of copper were too high (>1.0) at concentration values over $10^{-2}$ M and too low (<0.01) below that concentration to obtain a proper calibration curve (Fig A.6a). For easier spectrophotometric determination of copper concentrations, we utilized the base principle of complexometric titration. We introduced chemical reagents to form complexes with copper ions and amplify the light absorbance at certain wavelengths. Firstly, according to the study by Barrera et al. (1985), we introduced $10^{-2}$ M of ethylenediaminetetraacetic acid (EDTA) into the copper solutions. EDTA undergoes complexation with copper ions and as a result shows high light absorbance values

in the range of 600-800 nm [16]. We used EDTA for the copper concentration range $7.75x10^{-3}$-$3.25X10^{-3}$ M in which a reasonable absorbance value is obtained for a calibration curve (Fig. A.6b). Above and below this concentration range the resulting absorbance values were either over 1.0 or too low to observe reasonable changes. For lower copper concentrations ($10^{-3}$-$10^{-5}$ M) we used the method obtained from the study by Andres et al. (1995), in which a salt Diethyldithiocarbamate (DDTC) is used in the presence of the surfactant sodium dodecylsulfate (SDS). While DDTS forms complexes with copper ions, SDS ensures solubility of the resulting complex in aqueous media. By using $10^{-1}$ M and $2x10^{-2}$ M DDTC/SDS, we obtained a light absorption peak at 446 nm indicating copper presence (Fig. A.6c).

Using the aforementioned methods, calibration curves were obtained for different copper ion concentration. The concentration values and the resulting curves are shown in Fig. A.6d-f for pristine, EDTA and DDTC/SDS containing copper solutions. It is important to mention that at $10^{-2}$ M copper concentration; the pristine solution could be used without any need for complexes leaving the $10^{-1}$-$10^{-2}$ M range indeterminable.

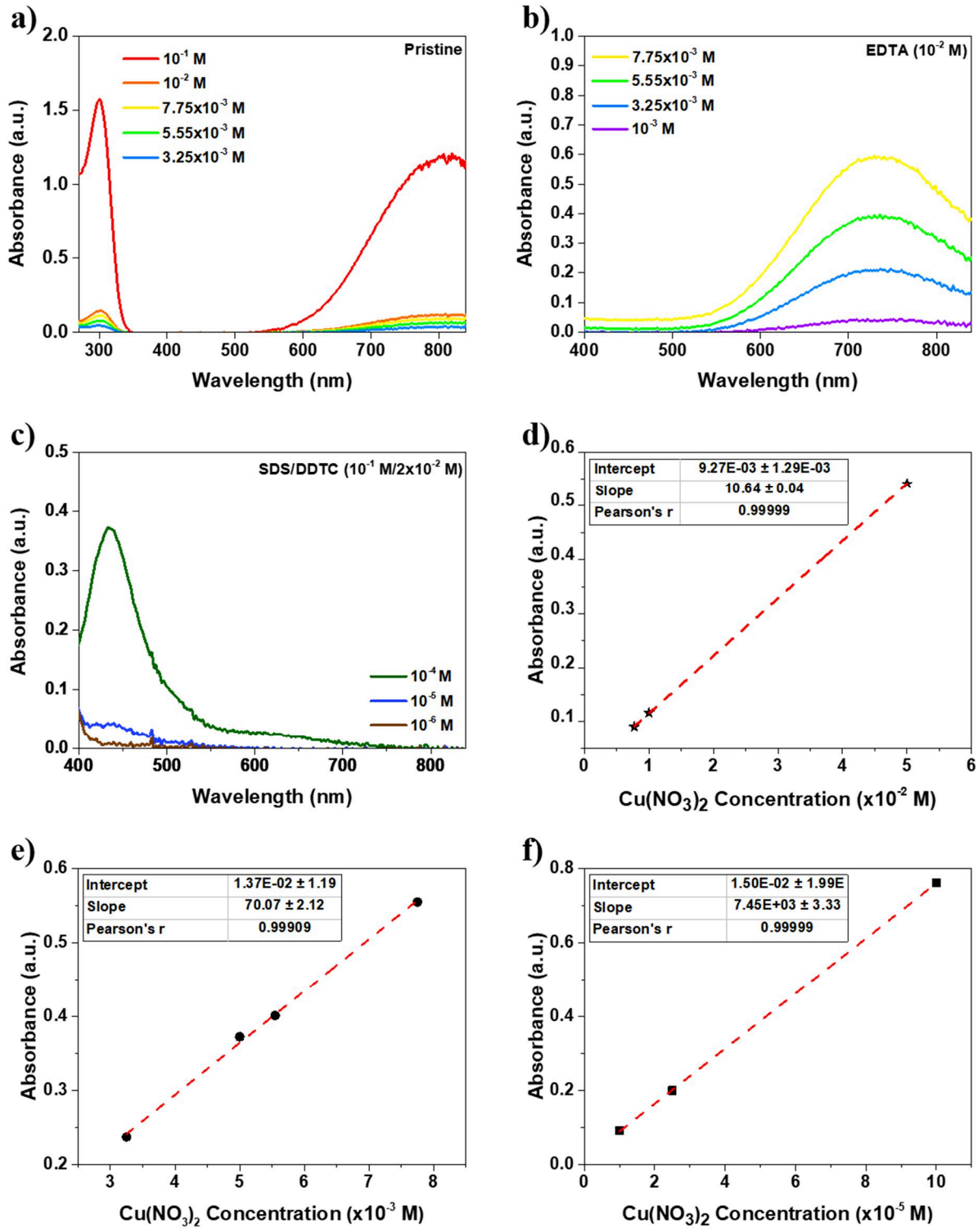



**Figure A.6:** a-c) UV-Vis spectra of pristine, EDTA and DDTC/SDS containing copper solutions. d-f) Calibration curves obtained for different copper ion concentration regions with different chemical complexes